CHALMERS
UNIVERSITY OF TECHNOLOGY

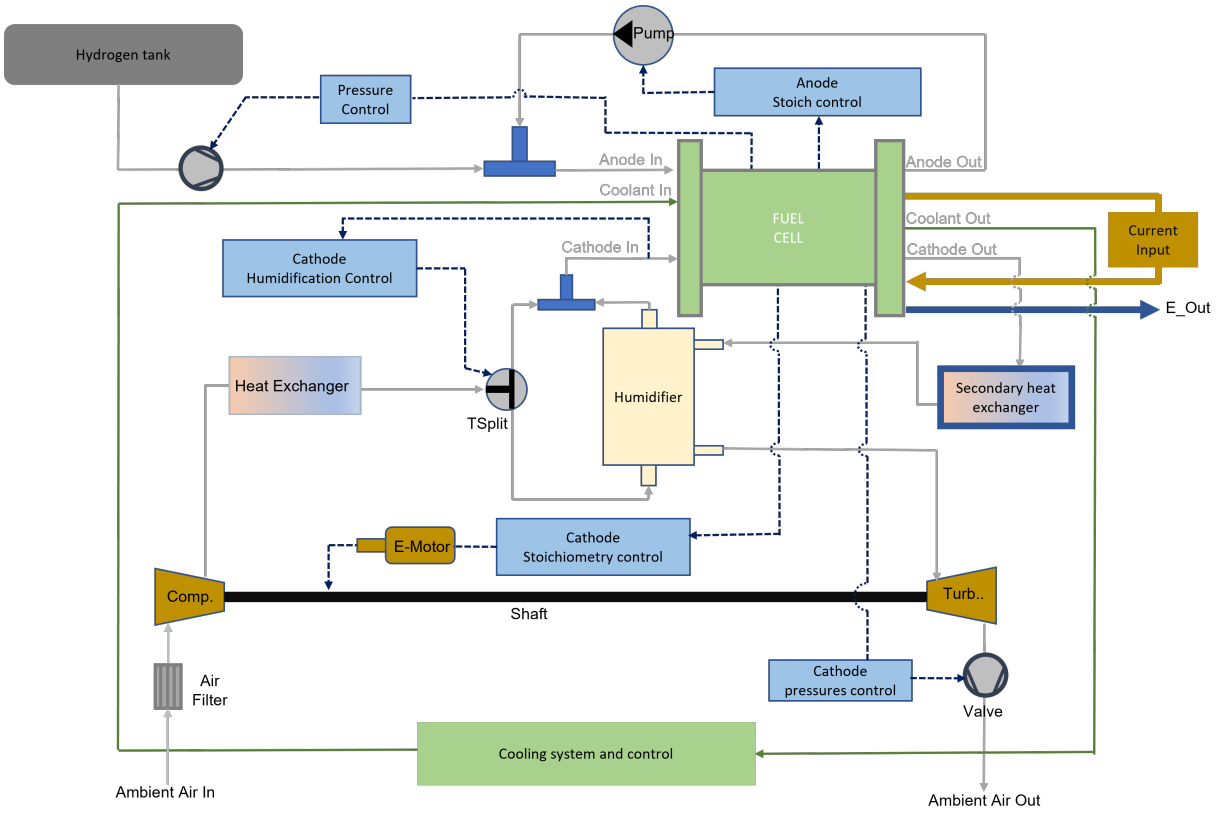


# Intermediate Temperature Fuel Cell Electric Vehicles: Simulation Study

Master's thesis in Mobility Engineering


Ashwin Bhagwat
Rahul Kumar Tiwari

DEPARTMENT OF PHYSICS
CHALMERS UNIVERSITY OF TECHNOLOGY
Gothenburg, Sweden 2023
www.chalmers.se

Master's thesis 2023

# Intermediate Temperature Fuel Cell Electric Vehicles: Simulation Study

ASHWIN BHAGWAT
RAHUL KUMAR TIWARI


CHALMERS
UNIVERSITY OF TECHNOLOGY

Department of Physics
Chalmers University of Technology
Gothenburg, Sweden 2023

Intermediate Temperature Fuel Cell Electric Vehicles: Simulation Study
ASHWIN BHAGWAT
RAHUL KUMAR TIWARI



Industrial supervisor: Staffan Luong, Volvo GTT, PSD Software solutions
Examiner: Björn Wickman, Department of Physics

Master's Thesis 2023
Department of Physics
Chalmers University of Technology
SE-412 96 Gothenburg
Telephone +46 31 772 1000

Intermediate Temperature Fuel Cell Electric Vehicles: Simulation Study

Gothenburg, Sweden 2023

Intermediate Temperature Fuel Cell Electric Vehicles: Simulation Study
ASHWIN BHAGWAT
RAHUL KUMAR TIWARI
Department of Physics
Chalmers University of Technology

# Abstract

Low-temperature proton exchange membrane fuel cells (LT-PEMFC) operating at 60 – 80 ℃ have shown higher efficiency, and better integration with vehicle applications but face issues such as slow reaction rate, water flooding, and low thermal gradient with respect to surrounding. On the other hand, high-temperature (HT) PEMFC operating at 150 – 200 ℃ enhances overall performance due to higher gas diffusivity, membrane conductivity, and waste heat treatment system. But due to high operational temperature, the water content of the HT-PEMFC decreases, leading to higher internal resistance, resulting in reduced performance of the fuel cell.
Therefore, this study focuses on building a detailed PEMFC model which can be operated at 80 ℃, as well as at 100, and 120 ℃ intermediate temperature (IT), and comparing the performance, power distribution, and efficiency at LT, and IT operation. A maximum power of 152 kW, 151 kW, and 130 kW is achieved while operating the same FC system at 80, 100, and 120 ℃ respectively. The efficiency results show that the FC operating at 80 ℃ has an efficiency range of 51% – 41%, whereas, at 100, and 120 ℃, the efficiency drops to 51% – 41%, and 34% – 33%, respectively. A single integrated system is built separately, which operates at 80 ℃ when the power demand is between 0 – 85%, and at 100 ℃ when the power demand is higher (85 – 100%). This system design allows for a 55% reduction in radiator size, and a 25% reduction in compressor map while maintaining system efficiency between 40 – 51%.
The degradation effect of the FC stack when operating at 80, 100, and 120 ℃ is also modeled. The results show that operating the fuel cell at 120 ℃ leads to accelerated degradation, and lower efficiency when compared to operating it at 80, and 100 ℃. Therefore, the FC system, which operates at a maximum of up to 100 ℃, is integrated with the vehicle model to analyze its effect at the vehicle level. The results show that hydrogen consumption (kg/100km) is approximately the same when operating at 80 ℃, and integrated system (running at 80 – 100 ℃). However, while operating the system only at 100 ℃, consumes 25% more hydrogen for the same driving cycle. Therefore, running the FC with an integrated system operational at 80, and 100 ℃ shows promising results.

Keywords: IT-PEMFC, cell calibration, BoP modeling, degradation modeling, system performance .

# Acknowledgements

We would like to express our sincere gratitude to our supervisor, and examiner, Prof. Björn Wickman, from Chalmers University of Technology. Your unwavering support, and invaluable guidance throughout our thesis journey have been truly exceptional. We would also like to extend a warm thank you to Volvo Group Trucks Technology(GTT) for providing us with the opportunity to write this thesis. It has been a very interesting, and rewarding experience. Thank you to all our colleagues at Volvo GTT for making us feel welcomed, and for all the time, and help you have given us. We would like to give a special thanks to our supervisor at Volvo GTT, Staffan Luong, for your continuous support, and valuable feedback throughout this project. We extend our heartfelt appreciation to Björn Ericson, and his team at KTH University for their invaluable contribution in providing us with the significant data required to construct, and validate our model. Their collaboration have been instrumental in the success of our Thesis. Furthermore, we would like to extend our sincere gratitude to our colleagues from the GTT-Powertrain Strategic Development (PSD) group, for their unwavering support, and invaluable guidance. Their expertise, and assistance have been pivotal in our journey,, and we are truly grateful for their contributions. Lastly, we would like to thank our families, and friends for supporting us throughout these years at Chalmers University.

Rahul Kumar Tiwari, and Ashwin Bhagwat, May 2023

# List of Acronyms

Below is the list of acronyms that have been used throughout this thesis listed in alphabetical order:

| | |
|---|---|
| FC | Fuel Cell |
| PEM | Proton exchange membrane |
| LT | Low temperature |
| IT | Intermediate temperature |
| HT | High temperature |
| BoP | Balance of plant |
| BEV | Battery electric vehicle |
| FCEV | Fuel cell electric vehicle |
| RH | Relative humidity |
| MEA | Membrane electrode assembly |
| ORR | Oxygen reduction reaction |
| PFSA | Perfluorosulfonic acids |
| OCV | Open circuit voltage |
| GDL | Gas diffusion layer |
| BPP | Bi-polar plates |
| EOD | Electro-osmotic drag |
| BD | Back diffusion |
| ICE | Internal combustion engine |
| PI | Proportional integral |

# Nomenclature

Below is the nomenclature of indices, sets, parameters, and variables that have been used throughout this thesis.

## Overall

| Symbol | Description | Unit |
|---|---|---|
| $i$, $I$ | Current | A |
| $A$ | Area | $cm^2$ |
| $V$ | Voltage | V |
| $i_o$ | Exchange current density | $A/cm^2$ |
| $\alpha$ | Transfer coefficient | - |
| $F$ | Farady's constant | C/mol |
| $T$ | Temperature | ℃ |
| $E_o$ | Reversible or equilibrium potential | V |
| $R$ | Gas constant | J/molK |
| $P$ | Pressure | bar |
| $\gamma$ | Heat capacity ratio | - |
| $a_c$ | Catalyst specific area | $cm^2/mg$ |
| $L_c$ | Catalyst loading | $mgPt/cm^2$ |
| $t_m$ | Membrane thickness | µm |
| $\lambda_m$ | Water content | - |
| $\lambda$ | Stoichiometry | - |
| $i_L$ | Limiting current | A |
| $PR$ | Pressure ratio | - |
| $RPM$ | Rotation per minute | rad/s |
| $\dot{m}$ | Mass flow rate | g/s |

| | | |
|---|---|---|
| $x_{\lambda}$ | State function for $\lambda$ control | - |
| $e_{\lambda}$ | Error function for $\lambda$ control | - |
| $K_{P\lambda-C}$ | Proportional constant for $\lambda$ control | - |
| $K_{I\lambda-C}$ | Integral constant for $\lambda$ control | - |
| $x_{Pc}$ | State function for cathode pressure control | - |
| $e_{Pc}$ | Error function for cathode pressure control | - |
| $K_{Ppress.}$ | Proportional constant for cathode pressure control | - |
| $K_{Ipress.}$ | Integral constant for cathode pressure control | - |
| $x_{Posbp}$ | State function for humidification control | - |
| $e_{Posbp}$ | Error function for humidification control | - |
| $K_{PPRH}$ | Proportional constant for humidification control | - |
| $K_{IPRH}$ | Integral constant for humidification control | - |
| $x_{pos2bp}$ | State function for IT humidification control | - |
| $e_{pos2bp}$ | Error function for IT humidification control | - |
| $K_{P2RH}$ | Proportional constant for IT humidification control | - |
| $K_{I2RH}$ | Integral constant for IT humidification control | - |
| $x_{AP}$ | State function for anode pressure control | - |
| $e_{AP}$ | Error function for anode pressure control | - |
| $K_{P-HP}$ | Proportional constant for anode pressure control | - |
| $K_{I-HP}$ | Integral constant for anode pressure control | - |
| $x_{\lambda-A}$ | State function for $\lambda - anode$ control | - |
| $e_{\lambda-A}$ | Error function for $\lambda - anode$ control | - |
| $K_{Pvflow}$ | Proportional constant for $\lambda - anode$ control | - |
| $K_{Ivflow}$ | Integral constant for $\lambda - anode$ control | - |
| $x_{TFC}$ | State function for coolant pump control | - |
| $e_{TFC}$ | Error function for coolant pump control | - |
| $K_{PTFC}$ | Proportional constant for coolant pump control | - |
| $K_{ITFC}$ | Integral constant for coolant pump control | - |
| $x_{Trad}$ | State function for radiator bypass control | - |
| $e_{Trad}$ | Error function for radiator bypass control | - |
| $K_{Ppbv}$ | Proportional constant for radiator bypass control | - |
| $K_{Ipbv}$ | Integral constant for radiator bypass control | - |

# Contents

# List of Figures

# List of Tables

# 1
# Introduction

Transport solutions are a vital part of modern life, and the past decade has seen a major shift in vehicle propulsion systems from fossil-powered vehicles to environmentally friendly, emission-free transportation. Increased legislative, and ecological demands to move towards carbon neutrality by 2050 have pushed the automotive industry towards electrified vehicles. The development of battery, and fuel cell (FC) technology is encouraging, and has become a research hotspot. While both produce zero tailpipe emissions, battery electric vehicles (BEV) are limited by their driving range, and long charging time. In contrast, fuel cell electric vehicles (FCEV) offer a shorter refueling time, lighter system, and longer range when compared to BEVs. The operating temperature window 100 – 120 ℃ of intermediate temperature proton exchange membrane fuel cell (IT-PEMFC) is less researched/experimented upon, and is the primary focus of this thesis. Such a system could overcome issues like water flooding, slow reaction, and internal resistance. IT-PEMFC could also provide a sufficient temperature gradient for an effective thermal heat recovery system for the balance of plant (BoP), and vehicle.

## 1.1 Objective

The objective of this thesis is to model, investigate the performance of an IT-PEMFC system, and analyze the effects of IT on the system's overall efficiency, heat management, and water management. The study will focus on optimizing the BoP components, such as the compressor, turbine, and fan, to achieve an ideal efficiency for the overall IT-PEMFC system, taking into consideration the impact of operating temperature on these components.

## 1.2 Delimeters

The experimental results obtained for this thesis focus on three specific temperature ranges: 80, 100, and 120 ℃. Consequently, the scope of the study is limited to analyzing, and comparing the performance of the IT-PEMFC system at these particular temperatures. In this thesis, a FC model from GT-Suite is utilized to analyze the performance of the IT-PEMFC system. However, it is acknowledged that to achieve a more dynamic representation, the controllers need to be enhanced to better control the system. The pre-existing model is specifically designed to accurately represent an operating temperature range of 60 – 80 ℃. The model's applicability to extended temperatures up to 120 ℃ is based on theoretical considerations. However, at higher

temperatures, such as 100, and 120 ℃, certain chemical reactions or activities may occur that are not explicitly accounted for in the model. As a result, the model's predictions or simulations in those temperature ranges might not fully capture the experimental observations or real-world behavior.
The primary objective of this study is to evaluate the performance of the IT-PEMFC system, and compare it with low temperature PEMFC (LT-PEMFC). It does not encompass proposing specific strategies or recommendations for improving the overall system efficiency or performance. Furthermore, a comparative analysis with high temperature PEMFC (HT-PEMFC) systems is also beyond the scope of this study.

## 1.3 Background

PEMFCs operating within the IT range have shown the potential to enhance performance in terms of reaction kinetics, catalyst tolerance, heat rejection, and water management. However, there is limited research conducted on IT-PEMFCs focusing on these aspects. Some studies have investigated the influence of relative humidity (RH), and partial pressures on IT-PEMFC performance. For instance, Ying Song et al.[1] evaluated cell performance under three different operating conditions (cell temperature ℃/ anode %RH/ cathode %RH): 80/100/75, 100/70/70, and 120/35/35. They observed voltage results of 0.72, 0.69, and 0.58 V, respectively, at ambient pressure, and 400 $mA/cm^2$. These findings highlight the need to optimize high-temperature membranes with improved conductivity to achieve effective performance at low RH. On the other hand, J. Zhang et al.[2] demonstrated that effective distribution, and higher RH (100%) enhance performance in terms of mass transfer, and membrane conductivity at elevated temperatures of 100 – 120 ℃. Their study was conducted on a 4.4 $cm^2$ in-house assembled membrane electrode assembly (MEA). Additionally, Xu et al.[3] investigated the impact of elevated temperature, and RH on the oxygen reduction reaction (ORR) kinetics in PEMFCs. They found that RH significantly affects catalytic activity within the range of 0 – 60% RH, but the effect becomes unclear at higher RH conditions $>$ 60%, and elevated temperatures. However, they also observed an increase in performance with increasing partial pressure from 0.1 atm to 1.0 atm. Overall, these findings emphasize the importance of understanding the system-level behavior of PEMFCs utilizing perfluorosulfonic acid (PFSA) membranes, such as Nafion, as electrolytes at temperatures exceeding 90 ℃. This necessitates further research to investigate different RH levels of incoming gases, and varied partial pressures within the anode/membrane/cathode system. Consequently, there is a motivation to delve deeper into modeling the IT-PEMFC system, and explore its effectiveness under diverse operating conditions.

## 1.4 Outline

After the report preface, chapter 2 will provide an introduction to FCs, and their BoP components. Chapter 3 will delve into the methodology, explaining how the study was systematically conducted. In chapter 4, the main results will be presented, while any additional results will be included in the appendix. This chapter will also include the discussion points, and reflections on the obtained results. Finally, the report will conclude with chapter 5, and 6, which will summarize the study's findings, and conclusions. Additionally, chapter 6 will discuss future work, and potential areas for further research.

# 2

# Fuel cell system theory

A FC is a device that generates electricity through an electrochemical process using hydrogen ($H_2$), and oxygen ($O_2$) as fuel. It's an electrochemical cell that converts the chemical energy of a fuel directly into electrical energy without the need for combustion, making it a clean, and efficient source of power. The basic components of an FC include an electrolyte, an anode (negative electrode), and a cathode (positive electrode). The electrolyte is typically a special porous material that allows ions to pass through while blocking the flow of electrons, creating an electric potential across the cell. At the cathode, the protons, electrons, and $O_2$ (or oxidant) combine to form water ($H_2O$), and release heat, making FCs environmentally friendly. To understand the generation of electric current from the reaction between $H_2$, and $O_2$, it is essential to analyze the individual reactions occurring at each electrode.
FCs are versatile, and can be used in a wide range of applications, including stationary power generation for buildings, transportation, portable electronics, and even in space applications. They are known for their high energy efficiency, low emissions, and quiet operation. Table 2.1 presents different types of FCs exist based on different type electrolyte, and their application, including PEMFC, solid oxide FC (SOFC), alkaline FC (AFC), phosphoric acid FC (PAFC), anion exchange membrane FC (AEMFC), and more, each with its own characteristics, and applications.

**Table 2.1:** Different types of FC technology [4, 5, 6, 7]

| Characteristic | **PEMFC** | **AFC** | **PAFC** | **AEMFC** | **SOFC** |
|---|---|---|---|---|---|
| Electrolyte | Polymer membrane | Potassium hydroxide | Phosphoric acid | Anion membrane | Ceramic |
| Operating temperature | 60 – 80 ℃ | 50 – 220 ℃ | 150 – 220 ℃ | 60 – 80 ℃ | 650 – 1000 ℃ |
| Catalyst | Platinum | Platinum | Platinum | Platinum | Nickel |
| Power range | 1 W – 100 kW | 1 kW – 10 kW | 10 kW – 1 MW | 100 kW – 10 MW | 10 kW – 10 MW |
| Typical application | Vehicle powertrain, small-scale power generation | Vehicle powertrain, small-scale power | Stationary power/heat generation | Portable power/small-scale power generation | Stationary power/heat generation |

The present thesis focuses on PEMFC, as they are widely used for automotive applications due to their high-power density, quick start-up time, and low operating temperatures. PEMFCs operate at temperatures below 80 ℃, which allows for a quick start-up time, and rapid response to changes in power demand, making them suitable for use in vehicle application that require quick acceleration, and deceleration. PEMFCs also have a high-power density, meaning they can generate a large amount of power in a relatively small, and lightweight package, which is important for automotive applications where space, and weight are critical factors. In addition, PEMFCs can use $H_2$ as a fuel source, which is a clean, and abundant source of energy that produces only water vapor, and heat as byproducts, making it an environmentally friendly option for automotive applications.

## 2.1 Fuel cell electrochemisty

A FC functions as an electrochemical energy converter, relying on simultaneous electrochemical reactions occurring at both the anode, and cathode. Figure 2.1 shows the schematic representation of a single cell. Reactions 2.1, and 2.2 take place at the interface between the ionically conductive electrolyte, and the electrically conductive electrode. Due to the involvement of gases in these electrochemical reactions, the electrodes of a FC must possess porosity to enable the entry of gases, and allow the exit of water (a byproduct) from the reaction sites [4].

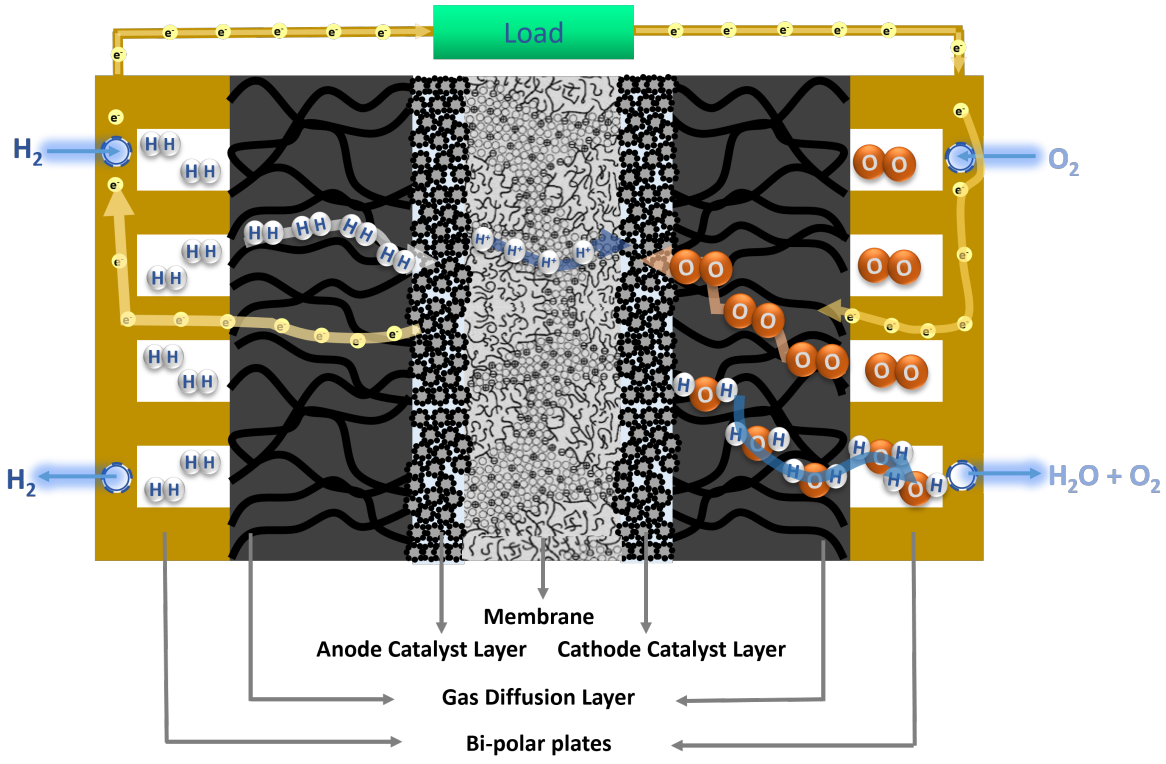


**Figure 2.1:** Schematic of single cell FC

### 2.1.1 Cell reaction

Electrochemical reactions encompass the transfer of electrical charge, and a variation in Gibbs energy [8]. The rate at which these reactions occur relies on the presence of an activation energy barrier that the charge must surmount when transitioning between the electrolyte, and a solid electrode, or vice versa. The velocity at which an electrochemical reaction takes place on the surface of the electrode is determined by the rate at which electrons are released or utilized, which corresponds to the electrical current.

At anode :

$$H_2 \rightarrow 2H^+ + 2e^- \tag{2.1}$$

At cathode :

$$\frac{1}{2}O_2 + 2H^+ + 2e^- \rightarrow H_2O \tag{2.2}$$

Overall :

$$H_2 + \frac{1}{2}O_2 \rightarrow H_2O \tag{2.3}$$

According to Faraday's law, the current density is directly proportional to both the quantity of charge transferred, and the consumption of reactant per unit area.

$$i = nFj \tag{2.4}$$

where:

| | |
|---|---|
| $nF$ | is charge transferred, C/mol, |
| $j$ | is flux of reactant per unit area mol/cm$^2$s. |

This net current is the difference between the forward, and reverse currents occurring on the electrode.

$$Red = Ox + ne^- \tag{2.5}$$

$$Ox + ne^- = Red \tag{2.6}$$

where:

| | |
|---|---|
| $Red$ | is reduction, |
| $Ox$ | is oxidation. |

In the FC, oxidation takes place at the anode, as per reaction 2.1, while reduction happens at the cathode, as per reaction 2.2. These oxidation, and reduction reactions are the fundamental reaction happening within the FC.

### 2.1.2 Voltage losses, and polarization

When the FC is not connected to any external load, it undergoes internal losses that lead to a reduction in cell potential, known as open circuit voltage (OCV). Nonetheless, once the FC is connected to an external load (for e.g. a resistor), it produces current, causing the cell's potential to drop. This decrease in potential is associated with distinct losses that occur at different levels of potential, and the same is presented in figure 2.2.

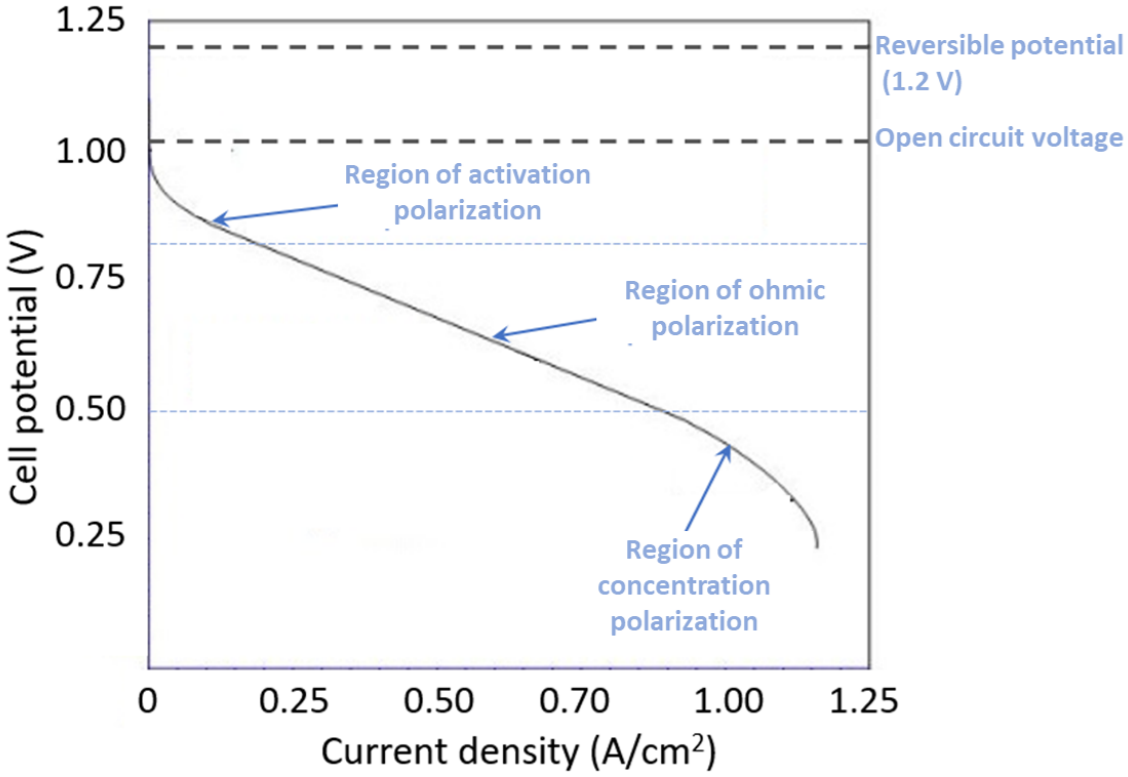


**Figure 2.2:** Polarization curve of single FC

#### 2.1.2.1 Activation polarization

In FC electrochemistry, initiating an electrochemical reaction requires an initial energy difference from equilibrium. This energy loss, translated into voltage, is referred to as activation polarization. Activation polarization is associated with the slower kinetics of the electrode reactions. These losses occur at both the anode, and cathode of the FC. However, in the case of $O_2$ reduction, higher overpotentials are required. This implies that the $O_2$ reduction reaction is considerably slower compared to the $H_2$ oxidation reaction. Therefore, the activation polarization losses are influenced by the reaction kinetics at the electrodes. A simple way to show the activation losses is through Tafel equation 2.7:

$$\Delta V_{act} = a + b \cdot log(i) \tag{2.7}$$

where:
$a$ is Tafel coefficient,
$b$ is Tafel slope.

$$a = -2.3\frac{RT}{\alpha F}log(i_o) \tag{2.8}$$

$$b = -2.3\frac{RT}{\alpha F} \tag{2.9}$$

From the above, it is noted that the Tafel equation is solely dependent on the transfer coefficient $\alpha$.

#### 2.1.2.2 Crossover losses

Although both $H_2$ crossover, and internal currents have conceptual similarities, they exhibit different effects in the FC. The loss of electrons occurs after the electrochemical reaction, resulting in the expected impact on the activation polarization of both the anode, and cathode. However, the consequences of $H_2$ permeation differ between the anode, and cathode. $H_2$ that permeates the membrane, and reaches the anode does not participate in the electrochemical reaction. Consequently, the total current resulting from the electrochemical reaction remains unaffected compared to the external current. On the other hand, when $H_2$ permeates to the cathode side, it reacts with $O_2$ on the catalyst surface, leading to the formation of $H_2O$. This reaction depolarizes the cathode, thereby reducing the potential of the cathode, and the overall cell. Furthermore, although $O_2$ permeation through the membrane is possible, its rate is significantly lower than that of $H_2$. The impact on FC performance resembles that of $H_2$ crossover losses; however, in this case, the anode also experiences depolarization. The extent of $H_2$ crossover is influenced by factors such as membrane permeability, membrane thickness, and the concentration difference of $H_2$ across the membrane. An open circuit potential below 0.9 V may indicate a potential $H_2$ leak or electrical short in the FC system. However, as the FC starts generating current, the concentration of $H_2$ in the catalyst layer (CL) decreases, diminishing the driving force for $H_2$ permeation through the membrane. Consequently, these losses become negligible during normal operating currents.

#### 2.1.2.3 Ohmic losses

Ohmic losses, as the name implies, arise from the hindrance encountered by ions in the electrolyte, and electrons in the electrically conductive (gas diffusion layer (GDL), bi-polar plates (BPPs), and electrical connection) components of the FC, leading to resistance. These resistive effects contribute to the overall decrease in cell performance.

#### 2.1.2.4 Concentration polarization

Concentration polarization occurs when the electrochemical reaction rapidly consumes a reactant at the electrode, resulting in the establishment of concentration gradients. The concentration of the reactant at the catalyst surface is influenced

by the current density, whereby higher current densities correspond to lower surface concentrations. At a certain point, the rate of consumption matches the diffusion rate, causing the reactant concentration at the catalyst surface to reach zero. This is known as the limiting current density, as the FC cannot produce a higher current beyond this point due to the absence of reactants at the catalyst surface.
In practical FCs, experiencing the exact limiting current density is rare due to non-uniform conditions across the porous electrode area. For a sharp drop in cell potential when reaching the limiting current density, the current density would need to be uniform across the entire electrode surface, which is seldom the case due to the presence of discrete particles comprising the electrode surface. While some particles may reach the limiting current density, others may continue to operate normally. Thus, the limiting current density may be encountered at either the cathode or anode, depending on the specific conditions of the FC.

### 2.1.3 Sensitivity parameters

The performance of a FC is affected by several factors, making it sensitive to external, and operating conditions. These conditions include temperature, RH, reactant gas pressure, and the partial pressure of oxygen $O_2$. Through precise control, and optimization of these parameters, it becomes feasible to improve the FC's performance, and achieve optimal operation of the system.

#### 2.1.3.1 Effect of RH

The impact of humidity on FC performance can be understood by its effect on membrane conductivity, and water transport within the cell. Water transport within the FC membrane involves several mechanisms, including electro-osmotic drag (EOD), back diffusion (BD), and convection (as shown in figure 2.3). EOD occurs when water molecules move alongside protons from the anode to the cathode. BD refers to the transfer of water into the membrane driven by a concentration gradient from the cathode to the anode. Convection, results from pressure differences between the cathode, and anode, causes water movement. However, the influence of convection is generally minor compared to the dominant effects of EOD, and BD, primarily due to the membrane's extremely low hydraulic permeability.
Maintaining an appropriate level of humidity is essential for efficient operation. When the humidity is too low, the membrane can become dehydrated, resulting in reduced proton conductivity. This leads to higher internal resistance, increased ohmic losses, and decreased cell performance. Insufficient humidity can also cause the membrane to dry out, leading to membrane degradation, and reduced durability. On the other hand, excessive humidity can lead to flooding, where excessive water accumulates in the electrode pores, and blocks the reactant gas diffusion paths. This restricts the supply of reactant gases to the catalyst sites, hindering the electrochemical reactions, and decreasing FC performance. Flooding can also cause increased mass transfer, and concentration polarization, further impacting the overall efficiency [10].

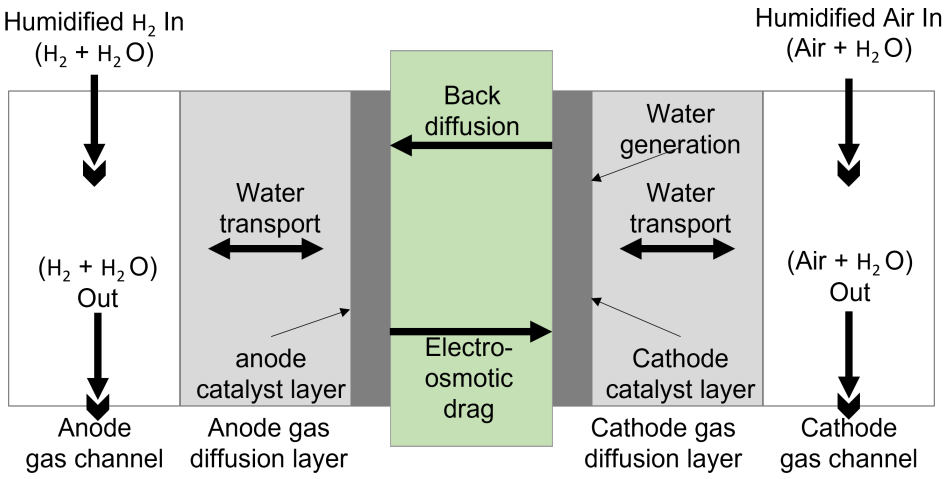


**Figure 2.3:** Water transport mechanism in FC [9]

#### 2.1.3.2 Effect of operating temperature

The impact of operating temperature on FC performance is not straightforward to predict based solely on the equations that describe the polarization curve. Temperature plays a significant role in every aspect of the FC performance, both explicitly, and implicitly. However, the effect of increased temperature on voltage can vary. PEMFC operating at 60 – 80 ℃ have demonstrated higher efficiency, and great integration with vehicle applications. However, numerous distinctive factors such as water flooding, and low thermal gradient (to extract waste heat) have hindered their progress [11]. On the other hand, HT-PEMFC operating at 150 – 200 ℃ enhances overall performance due to higher gas diffusivity, membrane conductivity, and waste heat treatment system [12]. But due to high operational temperature, the water content of the HT-PEMFC decreases, leading to higher internal resistance, resulting in reduced performance of the FC. The relationship between operating temperature, and FC performance is complex, and requires careful analysis to understand its specific influence on voltage output. Hence, with this study we are trying to understand the effect of operating the FC in the intermediate region, which means 80 – 120 ℃ on the stack, system, and vehicle level.

#### 2.1.3.3 Effect of oxygen partial pressure

The partial pressure of $O_2$ has an essential effect on FC performance. Adequate $O_2$ availability is essential for the electrochemical reactions at the cathode end. When the partial pressure of $O_2$ increases, it leads to a higher concentration of $O_2$ at the cathode, thereby enhancing the kinetics of the $O_2$ reduction reaction. Therefore, it improves cell performance, increases current density, and enhances efficiency. Insufficient $O_2$ partial pressure, on the other hand, can limit the availability of $O_2$ at the cathode, resulting in lower $O_2$ concentration at the electrode surface. This reduces the rate of the $O_2$ reduction reaction, and adversely affects cell performance. Insufficient $O_2$ supply can cause voltage losses, leading to decreased efficiency.
To optimize FC performance, it is necessary to regulate optimal $O_2$ partial pressure.

This can be achieved by ensuring efficient gas diffusion through the electrode structure. Proper $O_2$ supply is required to avoid performance limitations, and maximize the power output of the FC system. However, meeting the high $O_2$ partial pressure requirement can be more challenging in automotive applications where the air is the oxidant. The compression of air is limited, which poses difficulties in achieving the desired $O_2$ partial pressure for optimal FC performance. This limitation needs to be addressed in for automotive FC system.

### 2.1.4 Cell efficiency

The FC efficiency $\eta$ is the ratio between the electrical work produced $W_{el}$, and $Q$, which is energy in the consumed hydrogen.

$$\eta = \frac{W_{el}}{Q} \tag{2.10}$$

Electrical work is simply put as:

$$W_{el} = V \times I \tag{2.11}$$

and energy in consumed hydrogen as:

$$Q = \Delta HV \frac{I}{nF} \tag{2.12}$$

consumed $H_2$ can be translated to current according to Faraday's $1^{st}$ law:

$$N_{H_2} = \frac{I}{nF} \tag{2.13}$$

where:
$N_{H_2}$ is in mol/s,
$\Delta HV$ is hydrogen's heating value, 286 kJ/mol.

## 2.2 Single cell component

A single FC typically generates a relatively low voltage, usually less than 1 V. To achieve a higher voltage output, multiple cells are connected in series to form a stack. An example of a 3-cell stack is illustrated in figure 2.4. As mentioned earlier, each cell consists of an anode, a cathode, and an electrolyte layer. The anode, and cathode are commonly constructed using carbon paper or cloth, which are coated with catalysts to facilitate the electrochemical reactions. The electrolyte allows the transport of ions between the anode, and cathode. The individual cells are interconnected in series using bipolar plates (BPP), which serve as mechanical support for the stack, and create a conductive path for electron transfer between adjacent cells. The BPP also incorporate channels or pathways that efficiently distribute the reactants (fuel, and oxidant) to each cell, and collect the water produced during the electrochemical reaction. The following sections provide a detailed description of each component.

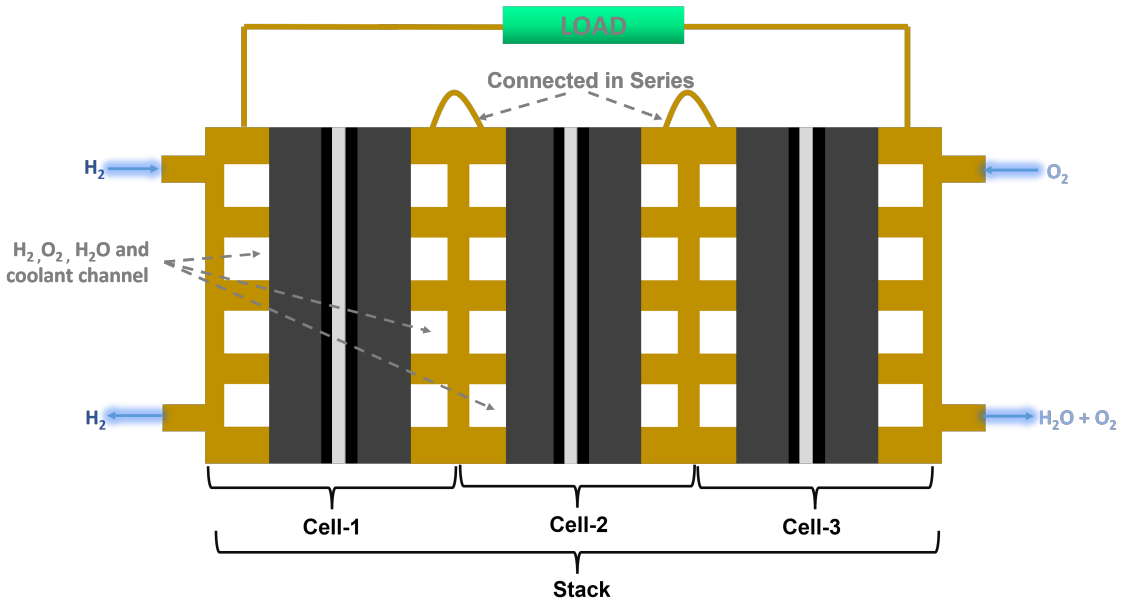


**Figure 2.4:** FC stack composed of 3 cells in series

### 2.2.1 Membrane

Nafion is a random copolymer consisting of perfluoroether side chains terminated with sulfonic acid groups randomly distributed along the semicrystalline polymer backbone [13]. This polymer is extensively used in various applications such as chlor-alkali electrolysis, water electrolysis, and polymer electrolyte FCs [14, 15]. The ionic conductivity of nafion is attributed to the highly hydrophilic sulfonic acid groups that can attract water, and form ionic clusters for proton transport. The conductivity, and permeability of nafion are mainly determined by the water content within the membrane. The presence of water facilitates a phase segregated structure in which the hydrophobic, and hydrophilic phases separate from each other.

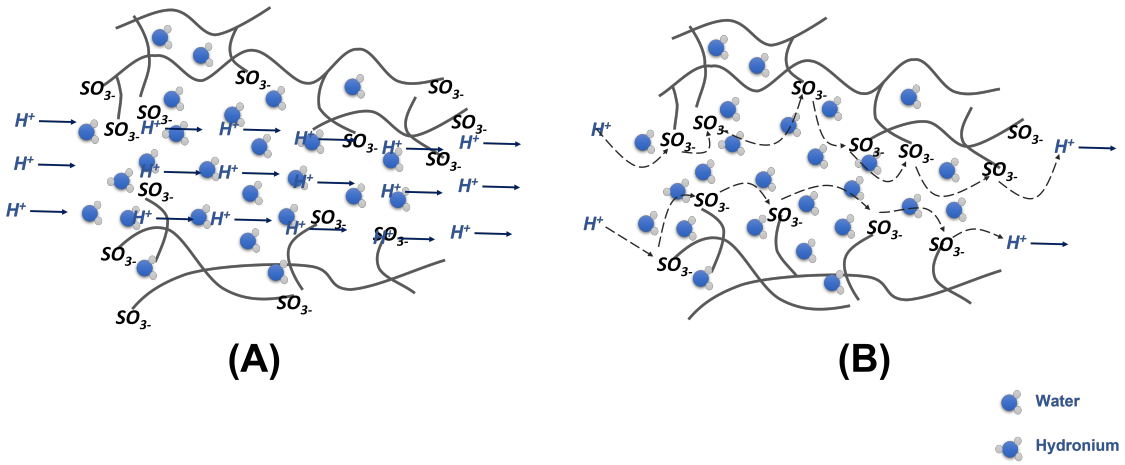


**Figure 2.5:** Schematic of (A) vehicular mechanism, and (B) hopping mechanism

The morphology of the nafion membrane has considerable impacts on its properties, with the cluster channel or cluster network structure being the first approach for its structure [16]. In the hydrated state, proton transport occurs through interconnected water channels by proton hopping, as represented in figure 2.5.B. The Grotthuss mechanism characterizes charge transfer with hydronium ions, being formed by a hydrated sulfonic acid group, and charge transfer to the next available sulfonic acid group. On the other hand, the vehicular mechanism describes the transport of hydronium ions through diffusion caused by EOD with the formation of other ions, which is shown in figure 2.5.A.
Despite the widespread use of Nafion in FC applications, there are notable limitations such as high fabrication costs, low ion conductivity at low humidity, and high temperatures, and low tolerance for fuel impurities. These limitations have led to extensive research efforts focused on increasing the ion conductivity of PEM materials at higher temperatures [17, 18]. The objective of such research is to overcome the aforementioned drawbacks of Nafion, and enhance its performance for FC applications. However, it is important to note that the scope of our thesis does not involve discussing these ongoing research efforts. Instead, our thesis aims to model the parameters of the current industrialized Nafion membrane. The objective is to gain insights that can be utilized to improve its performance, and provide valuable information for the development of novel PEM materials with enhanced properties.

### 2.2.2 Catalyst layer

The CL with the GDL has a thickness of approximately 10 µm, and comprises small particles of platinum metal on the surface of finely divided carbon of somewhat larger particle size. However, the requirements for the fuel side, and air side of the PEMFC are very different due to the slow rate of the ORR compared to the $H_2$ oxidation reaction. At a representative operating current density of 400 $mA/cm^2$, the voltage loss at the anode is about 10 mV, while that at the cathode is over 400 mV [19]. Therefore, the platinum loading in the CL on the cathode side is usually much higher than that in the layer on the anode side. The carbon in the CLs is typically produced by the pyrolysis of hydrocarbons to yield a highly porous, nanostructured powder with a high surface area (800 – 2000 $m^2/g$), such an example is the commercially available Vulcan XC72®. The carbon serves not only to disperse the active metal but also to provide good electronic conductivity to enable a high current to be drawn. The resulting loading of carbon with platinum maximizes the three-phase boundary between the catalyst, reactants, and electrolyte, which is critical for efficient catalysis. The performance of platinum catalysts depends on the degree of dispersion, and the particle sizes. Cyclic voltammetry (CV), and the characterization of catalysts using rotating disc electrodes have identified two fundamental reactions that can occur at the positive electrode in the PEMFC. The first equation 2.14 is the more normal $O_2$ reduction via a 4-electron transfer process, while the second equation 2.15 reaction is via a 2-electron transfer intermediate reaction that forms peroxide.

$$O_2 + 4H^+ + 4e^- \rightarrow 2H_2O \tag{2.14}$$
$$O_2 + 2H^+ + 2e^- \rightarrow H_2O_2 \tag{2.15}$$

Peroxide formation may occur if $H_2$ can crossover through the membrane, and then become oxidized directly on the cathode. Peroxide reacts with the electrolyte, and can accelerate electrode degradation. It is important, therefore, to minimize crossover in the PEMFC, and maintain electrode potentials within safe limits. Overall, the design, and optimization of CLs in PEMFCs play a significant role in enhancing their efficiency, and durability.

### 2.2.3 Gas diffusion layer

GDLs are thin layers of material coated with a catalyst as mentioned in above section 2.2.2 that facilitate the distribution of reactant gases to the CL. GDLs are situated on both sides of the membrane in a PEMFC, and their primary purpose is to ensure the uniform dispersion of reactant gases across the CL. However, to achieve optimal performance, GDLs must meet specific requirements [20]:

- Effective transport properties for delivery of the reactants to the active area, and removal of water.
- Mechanical integrity to provide structural support to the membrane, and CL.
- High electrical conductivity, and low interfacial contact resistance.
- High thermal conductivity, and corrosion resistance for PEMFC environment.

Carbon-based GDLs are commonly used due to their high electrical, and thermal conductivities, porosity, chemical stability, and commercial availability. Carbon paper, and carbon cloth are the two most used forms of GDLs, and the respective scanning electron microscopy (SEM) is presented in figure 2.6. These GDLs are produced using mature technology, and are suitable for commercialization. Additionally, a variety of carbon-based GDLs with different properties, and treatments are commercially available from various suppliers [21].

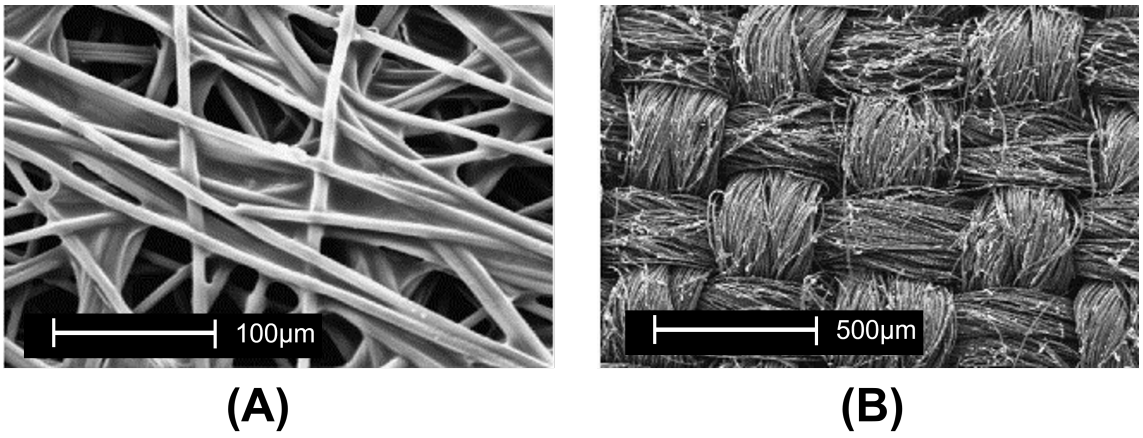


**Figure 2.6:** SEM images of: (A) carbon paper; (B) carbon cloth [22]
(Permission to use image granted by Elsevier)

GDL properties can be characterized into structural, and transport properties. The structural properties include porosity, thickness, and pore size distribution. Porosity plays a crucial role in PEMFC performance by affecting all transport properties, and hence, optimal porosity is required to maintain the balance between mass transport resistance. Thickness affects mass transport within the cell as well as the electrical, and thermal conductivity of the GDL. The pore size distribution can vary between different products, affecting their mechanical properties, and permeability. The transport properties include diffusivity, permeability, thermal, and electrical conductivities, and compressibility. Diffusivity plays a significant role in mass transport through the porous media of PEMFCs, driven by pressure differences, and temperature. The selection of GDL thickness, and porosity depends on the operating conditions, and flow field design. An optimal GDL thickness, and porosity are required to achieve a balance in water management, and effective reactants delivery.

### 2.2.4 Bi-polar plates

BPPs supply reactant gases, provide electronic connectivity between cells, offer structural support for MEAs, facilitate water, and heat management. However, these functions have conflicting requirements on BPP design. Therefore, the optimal design of BPPs is essential to achieve good stack performance, and lifetime. BPPs design should possess certain physicochemical characteristics, such uniform distribution of reactant gases over the active electrode surface to reduce concentration overpotential, high electronic conductivity for efficient current collection, strong mechanical properties to maintain stack integrity, impermeability to reactant gases for safe operation, corrosion resistance to withstand harsh cell environments for a long lifespan, and affordability through the use of low-cost materials, and automated fabrication methods [23]. Different geometrical configurations of gas flow fields are known, with conventional designs typically including pin, straight, or serpentine channels, which are illustrated in figure 2.7.

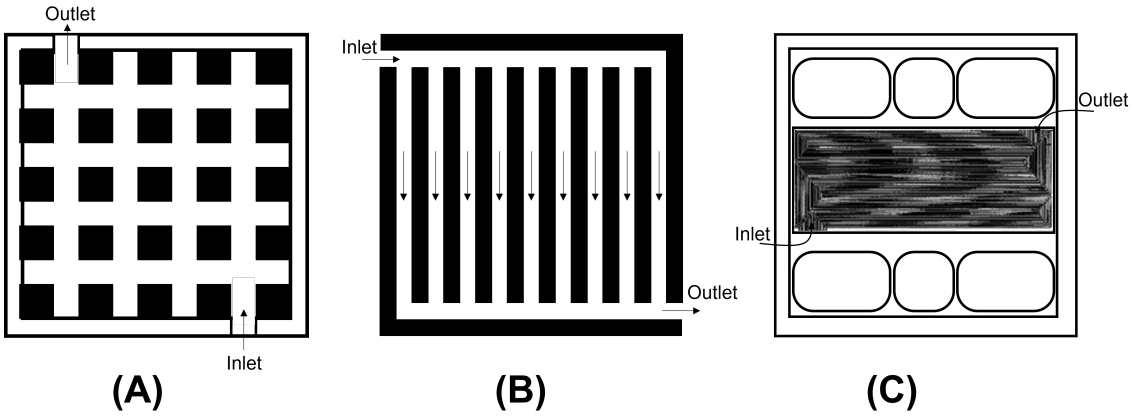


**Figure 2.7:** Different BPP design (A) pin design [24]; (B) straight, and parallel design [25]; (C) serpentine [26]

Pin-type flow fields, which consist of many pins arranged in a regular pattern, are commonly used in practice. Cubical or circular pins are typically used on both

cathode, and anode flow-field plates, allowing reactant gases to flow through intervening grooves. While pin-design flow fields result in low reactant pressure drop, they may lead to channeling, and stagnant areas, resulting in uneven reactant distribution, inadequate product water removal, and poor FC performance. Additionally, recirculation zones may arise behind each pin, leading to reactant concentration depletion, and decreased cell, and stack performance, especially with certain geometric shapes of flow fields.
The gas flow-field plate in this design includes multiple parallel flow channels that are connected to both the gas inlet, and exhaust headers. These channels run parallel to the edges of the plate. The purpose of this design is to distribute the reactant gas flow uniformly across the FC. However, this design often suffers from inadequate water drainage, and poor gas flow distribution on the cathode side. When air is used as the oxidant, water droplets tend to accumulate in the flow channels adjacent to the cathode, causing the channels to become wet, and the water to cling to the bottom, and sides of the channels. This results in stagnant areas throughout the plate, causing low, and unstable cell voltages to occur after extended periods of operation. Additionally, the straight, and parallel channels in the BPPs tend to be relatively short, and have no directional changes, leading to a small pressure drop along these channels. As a result, the pressure drops in the stack distribution manifold, and piping system, which is normal to the BPPs, tends to be large in comparison. This leads to non-uniform flow distribution of reactant gases among various active cells in the stack, causing poor cell performance.
To address water flooding resulting from inadequate water removal, Watkins et al.[26]. proposed using a single continuous fluid-flow channel that follows a serpentine path. This design eliminates stagnant flow areas but results in a long reactant flow path, substantial pressure drop, and significant concentration gradients from the inlet to the outlet. The use of a single channel to collect all the liquid water produced from the electrode reaction may also promote flooding, especially at high current densities. For higher current density operation, he also suggested using several continuous separate flow channels to limit the pressure drop, and minimize parasitic power required to pressurize the air. This design ensures adequate water removal, and no stagnant area formation at the cathode surface due to water accumulation. However, there has been extensive research on many different designs of flow fields patterns trying to reduce the pressure loss, and allow sufficient flow of the reactant. But within the scope of our current thesis, we will use 5-channel serpentine counter flow design, as they have significant performance increase when comparing to pin or single/parallel design.

## 2.3 Balance of plant

The BoP in a FC system comprises all the necessary components, and systems that support the proper functioning of the FC stack. It comprises the components that deliver fuel, and oxidant to the stack, manage waste products, and provide control, and monitoring functions. The BoP can vary depending on the FC type, and the application. For instance, the schematic of the FC-BoP is shown in figure 2.8, and the same is described below:

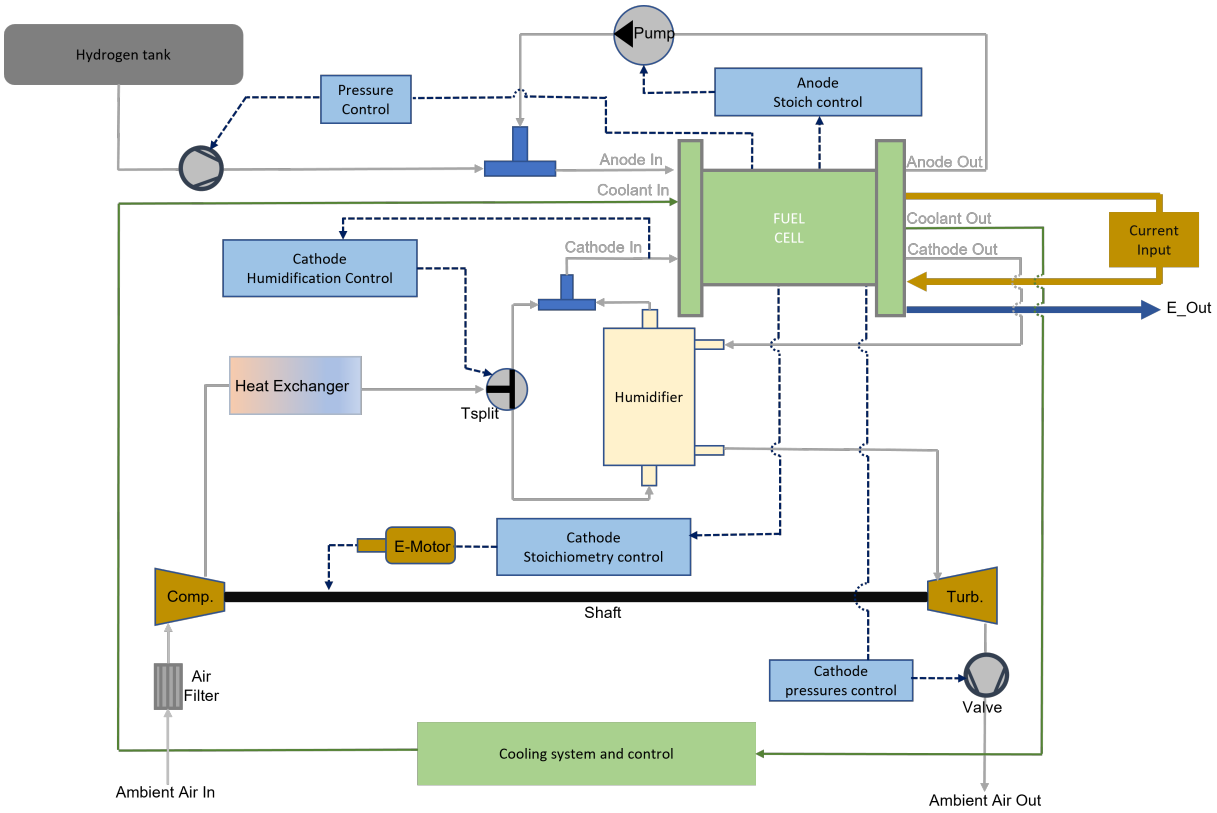


**Figure 2.8:** Schematic of complete FC-BoP

### 2.3.1 Air supply system

The air supply system comprises an air compressor, heat exchanger, humidification system, and expander. These components work together to ensure a continuous flow of air with the necessary humidity for proper cathode reaction in the FC stack. The power output of the FC system is directly influenced by the mass flow of air, which depends on pressure and volume flow. It is crucial to maintain the pressure, and humidity at the required levels as they significantly impact the performance of the FC system.

#### 2.3.1.1 Compressor

A compressor is a device that is used to increase the pressure of a gas or vapor by reducing its volume. Compressors majorly take in low-pressure gas or vapor, and then reducing its volume, which in turn increases the pressure. This is typically accomplished by using a piston, diaphragm, or rotating impeller to compress the gas or vapor. The compressed gas or vapor is then released at a higher pressure requested by the system [28]. Compressors are available in many different types, and sizes, and are often designed specifically for the application they will be used in. Dong et al.[29] provided a comprehensive analysis of four major types of compressors that can be used in FC vehicles, which includes roots, scroll, screw, and turbo compressors.
This study showed that the turbo compressor demonstrated the highest isentropic efficiency of 79.5% among the compressors evaluated. The scroll compressor showed

the lowest isentropic efficiency of 68.3%. The power consumption of the compressors ranged from 2.88 kW for the screw compressor to 5.05 kW for the root's compressor. The turbo compressor showed the lowest power consumption of 3.33 kW. The overall system efficiency was also evaluated for each compressor. The study found that the turbo compressor had the highest overall system efficiency of 43.3% among the compressors evaluated. The turbo compressor demonstrated the highest isentropic efficiency, lowest power consumption, and highest overall system efficiency among the compressors evaluated in the study.

#### 2.3.1.2 Air-filter

Air filters ensure the delivery of clean, and uncontaminated air to the FC stack. Specifically designed to protect the FC's sensitive components, such as CLs, and PEMs, these filters serve to prevent harmful particles from degrading performance or causing irreparable damage. Without effective filtration, these impurities can accumulate on catalyst surfaces, obstruct gas diffusion pathways, and hinder the electrochemical reactions occurring within the FC. To achieve efficient air filtration, FC air filters incorporate advanced filtration media characterized by high efficiency, and low-pressure drop. Depending on the specific requirements of the FC system, these filtration media may include materials like porous ceramics, fibrous materials, or metal meshes. The filters are meticulously designed to possess a high dust-holding capacity while maintaining adequate airflow rates to cater to the FC's demands. Figure 2.9 shows the example of air filters used in FCs for varied power, and system requirements.


**Figure 2.9:** Air filter for FCs for varied power requirement [31] (Permission to use image granted by Hengst filtration)

#### 2.3.1.3 Heat exchanger

The air discharged from the compressor is at elevated temperature than the surrounding ambient air, necessitating additional cooling to ensure optimal functionality of the FC. It is important for the heat exchangers to provide minimal pressure drop to ensure that the air can flow smoothly through the system without signifi-

cant resistance. This is particularly important as the airflow is directed towards the cathode, where it participates in the $O_2$ reduction reaction. Heat exchangers serve as the key devices employed to extract, and regulate the heat from the incoming air, achieving the desired temperature conditions for the FC operation.

### 2.3.2 Hydrogen flow system

Just as the cathode end requires a supply of air, the anode side of the FC demands a supply of $H_2$. The proper functioning of the FC relies on the availability of $H_2$ at the anode, delivered at the specific temperature, and humidity levels. To meet these requirements, the $H_2$ supply system comprises essential components, including a $H_2$ tank, control valve or pressure regulator, and a recirculation pump. Together, these system work to ensure the precise delivery of $H_2$ to the anode, facilitating optimal performance of the FC.

#### 2.3.2.1 Hydrogen tank

$H_2$ tanks are specifically designed to store $H_2$ gas in a compact, and lightweight manner, maximizing space utilization within the vehicle while adhering to safety standards. One widely used technique for $H_2$ storage is compressed gas, where $H_2$ is stored in high-pressure tanks with maximum operating pressures typically ranging from 20 to 70 MPa [32]. Among these pressures, 70 MPa is often considered the most economically viable for onboard storage, considering factors such as driving range, and space limitations within the vehicle [33].

**Table 2.2:** Different types of compressed $H_2$ tank

| Cylinder types | **Material** | **Feature** | **Application** | **Pressure, and weight percentage** |
|---|---|---|---|---|
| Type I | All metal | Corrosion, and heavy | Industrial | 17.5 – 20 MPa, 1 wt% |
| Type II | Metal liner with hoop wrapping | Corrosion, heavy, and short life | Industrial | 26.3 – 30 MPa |
| Type III | Metal liner with composite wrapping | Lightness, high burst pres., no permeation, lower corrosion | Vehicle (25 – 75% wt gain) | 35 MPa: 4 wt% 70 MPa: 5 wt% |
| Type IV | Plastic liner | Light, and lower burst pressure | Longer life, and vehicle | 70 MPa: $>$ 5 wt% |

Compressed $H_2$ storage is highly efficient, as the energy density increases with the pressure of the gas. However, alternative approaches such as cryo-compressed ($CcH_2$), which combines compressed gas, and liquid $H_2$, offer even higher density but come with challenges related to refrigeration, and insulation [34]. Other techniques for $H_2$ storage, such as metal-organic frameworks (MOFs), carbon nanostructures,

and metal hydrides, have their own advantages, and limitations. MOFs show promise at low temperatures, but face issues related to scalability, and thermal management [35]. Carbon nanostructures have limited storage capacities, and practicality for practical applications [32]. Metal hydrides, such as magnesium hydride, offer decent energy densities but suffer from slow kinetics, and safety concerns.
Despite these alternative methods, compressed $H_2$ cylinders remain the industry standard for automotive applications due to their comparable energy densities to fossil fuels. Table 2.2 shows different types of cylinder, which can store $H_2$ gas at various pressure levels, with Type I metallic pressure vessels commonly used for industrial applications operating at pressures of 20 – 30 MPa [43]. However, Type I vessels have limitations in storage efficiency, typically storing only about 1 wt% of $H_2$. Type II vessels feature a cylindrical part wrapped with fiber resin composite, while Type III, and Type IV vessels are fully composed of composite materials, often designed as composite overwrapped pressure vessels (COPVs). In the scope to estimate the flow, and losses compressed $H_2$ tank is simulated in this study, below figure 2.10 shows the schematic view of a type 4 pressurized $H_2$ reservoir.

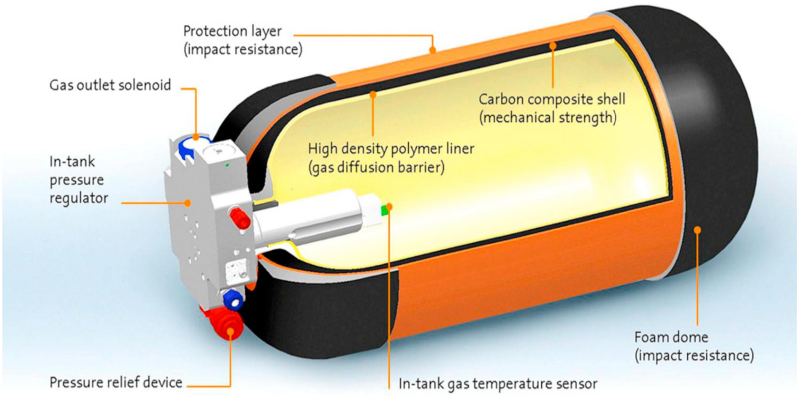


**Figure 2.10:** Type-IV composite overwrapped $H_2$ pressure vessel [36]
(Permission to use image granted by Elsevier)

#### 2.3.2.2 Hydrogen valve

A $H_2$ valve is a device used to control the flow of $H_2$ gas. It regulates the passage of $H_2$ through a pipeline or system, allowing for safe, and efficient distribution or utilization of the gas. The valve can be opened or closed manually or automatically, depending on the application. It allows to maintain the desired pressure, preventing leaks, and ensuring the safe operation of $H_2$ based systems, and equipment.

#### 2.3.2.3 Recirculation pump

To maintain proper $H_2$ humidification, and continuous flow, a re-circulation pump is used in the anode feedback loop. These re-circulation pumps are designed to provide a consistent, and controlled flow of $H_2$, considering factors such as pressure, flow rate, and back pressure, promoting humidified $H_2$, and preventing localized fuel starvation.

### 2.3.3 Humidification

Ensuring proper hydration of the proton-conducting membrane is crucial for efficient proton conduction in FC systems. Inadequate humidification or operating without humidification can result in accelerated membrane degradation due to radical formation, and dehydration [37]. Conversely, excessive water content can lead to water flooding, where the porous electrode structures become overwhelmed with water, impeding reactant transport. Therefore, optimizing the quantity, and distribution of water within the FC structure is essential for achieving high conductivity, and durability of the proton-conducting membrane while facilitating reactant transport. Extensive research has been conducted over the past few decades to investigate water management, and transportation in FC systems, leading to the development of successful methods. These methods encompass various techniques, such as incorporating microporous layers, optimizing the pore structure in the GDL, and designing innovative internal flow field structures. Externally, systems such as gas-bubbling humidifiers, direct water injection [38], enthalpy wheel humidifiers, and membrane humidifiers are employed. Gas bubbling humidifiers, and direct water injection methods offer high humidification performance but are primarily suitable for stationary applications due to their larger relative volume, and weight. The enthalpy wheel humidifier method helps improve overall efficiency, although gas leakage and parasitic losses pose challenges. Among these systems, the membrane humidifier is particularly attractive due to its simple structure, lightweight design, and good performance, making it well-suited for automotive applications.

#### 2.3.3.1 Humidifier

The process of humidification in the membrane humidifier involves the utilization of wet gas or liquid water to introduce moisture into the dry gas. The wet gas or liquid water is directed through one side of the membrane, while the dry gas flows through the other side. A membrane, typically nafion, is employed to separate the wet side from the dry side within the humidifier. In our specific system application, we will utilize a gas-to-gas membrane humidifier. This involves using the wet exhaust gas from the FC outlet to humidify the dry gas coming from the compressor side. The concept behind this approach is to recirculate the humidified gases, and utilize the water generated at the cathode end to humidify the incoming dry gases. By implementing this system, parasitic losses can be reduced, leading to improved overall efficiency. Figure 2.11 presents the schematic of gas-to-gas humidifier.

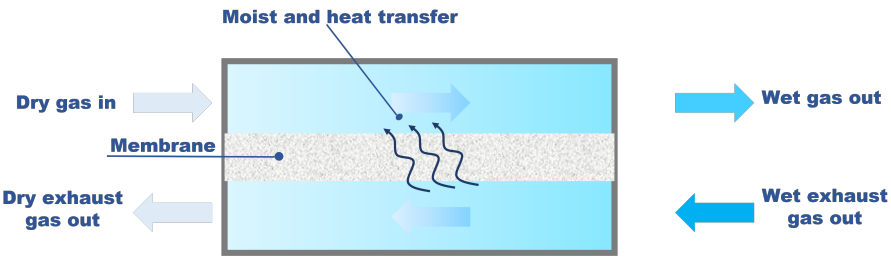


**Figure 2.11:** Schematic of gas-to-gas membrane humidifier

### 2.3.4 Cooling system

A cooling system is essential for achieving high energy conversion efficiency in PEMFC. These FCs produce waste heat at a similar rate to their electrical power output. For instance, in a 100 kW FCEV, a 60% energy efficiency would correspond to a heat generation rate of 40 kW by the FC stack. Thus, it is vital to develop effective heat dissipation techniques to maintain the optimal operating temperature of PEMFCs, typically in the range of 60 – 80 ℃. It is important to note that dissipating heat within this temperature range is more challenging compared to internal combustion engines (ICEs) due to differences in the surrounding temperature gradient. The selection of the optimal operating temperature is primarily driven by the need to mitigate electrode flooding, maintain proper PEM hydration, and prevent material degradation. In FCEVs, which typically operate within power ranges of 10 – 200 kW, liquid cooling systems are commonly employed to manage heat within the FC stacks, as indicated in the table 2.3:

**Table 2.3:** Different types of FCEV, and cooling method

| **FCEV** | **Stack Power [kW]** | **Cooling Method** |
|---|---|---|
| Hyundai Nexo | 95 | Water Cooling [39] |
| Honda FCX Clarity-2017 | 103 | Perpendicular coolant channel [40] |
| Tyota Mirai | 114 | Water cooling |
| Hyundai Tucson-2016 | 100 | Water cooling [39] |
| Saic MAXUS FCV80 | 115 | Water cooling [40] |

#### 2.3.4.1 Radiator

Radiators are integral heat exchangers employed for the purpose of efficiently transferring thermal energy between different mediums, facilitating cooling, and heating processes. In FC systems, the radiator serves the purpose to extract heat from the coolant, primarily utilizing conduction to the tubes, and fins, and convection to the surrounding air. In the FC, the coolant is circulated through the BPP, where it absorbs heat generated by the FC stack. The heated coolant is then passes through a thermostat or a thermal-controlled bypass mechanism, regulating the flow to the radiators. As the coolant traverses the radiator tubes, it efficiently transfers a significant portion of its heat to the tubes themselves, which subsequently transmit the heat to the fins interposed between each row of tubes. These fins design are critical in maximizing the contact surface area between the tubes, and the ambient air, thus enhancing the efficiency of heat exchange. Consequently, the fins release the accumulated heat to the surrounding air, promoting cooling. This cyclic process of heat extraction, and dissipation continues as the cooled liquid is directed back to the FC system for reutilization. It is common for the coolant to consist of a water-based solution, typically augmented with glycols to prevent freezing, and other additives to mitigate issues such as corrosion, erosion, and cavitation.

#### 2.3.4.2 Coolant pump

These pumps are designed to circulate coolant or fluid through the cooling system to maintain optimal operating temperatures, and ensure efficient heat dissipation. The primary function of these pumps is to manage the thermal balance of the system by removing excess heat generated by various components by efficiently regulating coolant flow, the pump prevents overheating, and helps maintain the desired temperature range for optimal system performance, and longevity. This allows the pump to adjust coolant flow rate based on the system's cooling demands, ensuring that the components are adequately cooled under different operating conditions. Additionally, the pumps can be integrated with the overall system, enabling efficient thermal management, and optimizing energy consumption.

#### 2.3.4.3 Fan

The radiator fans is responsible for circulating air through the vehicle's radiator. When the vehicle is not in motion or is moving at low speeds, it helps to regulate air through the radiator when there is not enough airflow through the grille. The type, and size of the fan have an impact on the temperature regulation of the vehicle's cooling system. The air acts as a medium to extract heat from the coolant, which passes through the radiator to dissipate the heat. The control of these fans is determined either by a thermostatic switch or the specific temperature requirements of the cooling system.

# 3

# Methodology

The focus of this thesis is to perform a simulation study of PEMFC operating at extended temperatures of 80, 100, and 120 ℃, and analyse its effect on the overall performance of the system, and the vehicle. Substantial part of the work is carried out on GT-Suite [48], which is a modeling, and simulation software developed by Gamma Technologies. It offers a convenient environment for analysing, and optimizing different automotive systems. A pre-configured FC model provided in the software is used as the basis model, and is worked upon to study the performance of FC at intermediate temperatures. This chapter covers the flow of the executed work.

## 3.1 Modeling

### 3.1.1 Cell modeling

A pre-loaded template 3.1 of a single FC is first studied in order to have a deeper understanding of the input, and output flows, and also the equations, and parameters that define the cell.

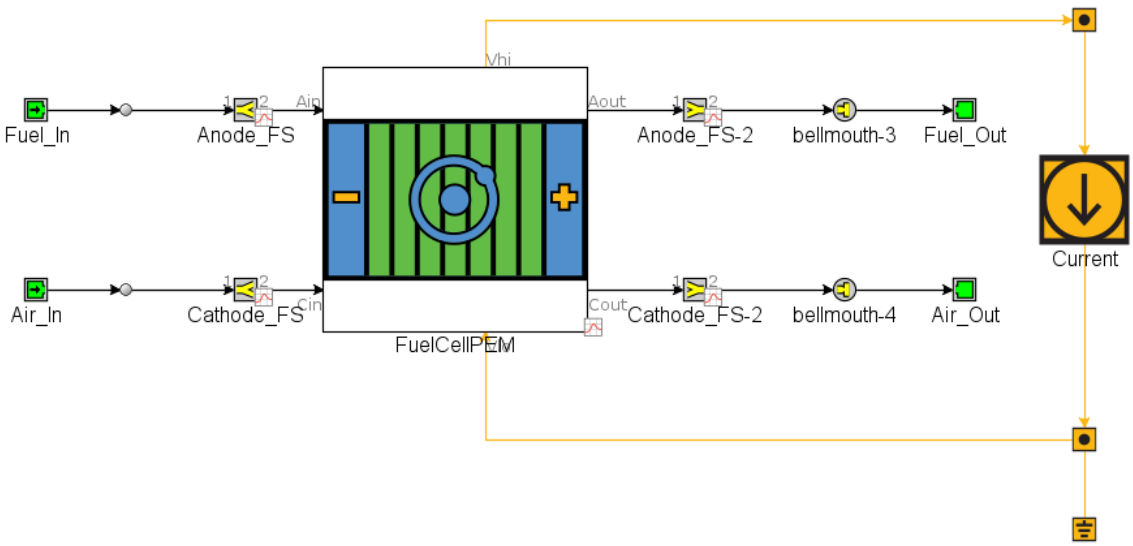


**Figure 3.1:** Single cell model

#### 3.1.1.1 Cell details

An electrochemical model characterizes the FC by incorporating calculations for the OCV, and overpotential. It is represented in the form of a polarization curve in figure 2.2. OCV is the maximum theoretical voltage provided by the FC without any external connected load. Overpotential is the additional potential required for the cell to reach equilibrium potential.

- **Fuel cell operating voltage**

$$V_{cell} = E^o - V_{act} - V_{ohm} - V_{conc} - V_{delOC} \tag{3.1}$$

where:
$E^o$ is reversible cell potential,
$V_{act}$ is activation overpotential,
$V_{ohm}$ is ohmic overpotential,
$V_{conc}$ is concentration overpotential,
$V_{delOC}$ is internal voltage loss.

- **Reversible potential**
The reversible potential is the theoretical voltage calculated using equation 3.2 that converts the reaction enthalpy to electricity.

$$E^o = \frac{-\Delta G}{2F} = 1.23V \tag{3.2}$$

$$\Delta G = \Delta H - T\Delta S \tag{3.3}$$

where:
$\Delta G$ is Gibbs free energy,
$\Delta H$ is difference between heat of formation of products, and reactants,
$\Delta S$ is difference between entropy of products, and reactants.

$$\Delta H = (h_f)_{H_2O} - (h_f)_{H_2} - \frac{1}{2}(h_f)_{O_2} \tag{3.4}$$

$$\Delta S = (s_f)_{H_2O} - (s_f)_{H_2} - \frac{1}{2}(s_f)_{O_2} \tag{3.5}$$

- **Activation polarization**
At low current densities, a small overpotential is necessary to overcome the activation energy of the sluggish electrochemical reactions taking place on the electrodes. This is called activation polarization, and is given by,

$$V_{act} = \begin{cases} \frac{R \cdot T}{2 \cdot \alpha_c \cdot F} \cdot ln\left(\frac{i}{i_{o,c}}\right) & i \leq i_{o,c}/(1-\alpha) \\ \frac{R \cdot T}{2 \cdot \alpha_a \cdot F} \cdot ln\left(\frac{i}{i_{o,a}}\right) & i > i_{o,a}/(1-\alpha) \end{cases} \tag{3.6}$$

where:
$\alpha_i$ is charge transfer coefficient,
$i_{o,c}$ is cathode exchange current density,
$i_{o,a}$ is anode exchange current density.

these define the readiness of electrode to undergo electrochemcial reaction.

$$i_{o,c} = {i_o}^{ref} a_c L_c \left(\frac{P_{O_2}}{P_{ref}}\right)^{\gamma} exp\left[\frac{E}{R}\left(\frac{1}{T_{ref,cat}} - \frac{1}{T_{cell}}\right)\right] \tag{3.7}$$

$$i_{o,a} = {i_o}^{ref} a_c L_c \left(\frac{P_{H_2}}{P_{ref}}\right)^{\gamma} exp\left[\frac{E}{R}\left(\frac{1}{T_{ref,an}} - \frac{1}{T_{cell}}\right)\right] \tag{3.8}$$

where:
$P_{ref}$ is 1 atm,
$T_{ref,cat}$ is 298.15 K,
$T_{ref,an}$ is 353 K.

${i_o}^{ref}$, $a_c$, $L_c$, and $E$ are user inputs, and $i_{o,i}$ is evaluated at each timestep based on the instantaneous values of $P_{O_2}$, $P_{H_2}$, and $T_{cell}$.

- **Ohmic polarization**
Figure 2.2 shows a linear decrease in cell potential in the region of ohmic resistance. This is observed due to internal resistance in electrolyte that resist flow of ions, and also due to internal resistance in other cell components that resist flow of electrons. The linear relation is defined by Ohm's law as:

$$V_{ohm} = R_{ohm} \cdot i \tag{3.9}$$

$$R_{ohm} = \frac{t_m}{\sigma_m} \tag{3.10}$$

where:
$t_m$ is membrane thickness,
$T_{ref,cat}$ is membrane conductivity.

$\sigma_m$ can further be equated as an exponential function with respect to temperature, and coefficients $b_{11}$, $b_{12}$, and $b_2$.

$$\sigma_m = (b_{11}\lambda_m - b_{12}) exp\left(b_2\left(\frac{1}{303} - \frac{1}{T_{cell}}\right)\right) \tag{3.11}$$

where:
$\lambda_m$ is water content in the membrane,
$a$ is water vapour activity.

$$\lambda_m = 0.043 + 17.81a - 39.85a^2 + 36.0a^3 \quad \text{for } 0<a<1 \tag{3.12}$$

$R_{ohm}$ in equation 3.10 is evaluated at each time step based on the instantaneous values of $\lambda_m$, which is dependant, and $T_{cell}$.

- **Concentration polarization**
  At higher current densities, the reaction kinetics increase rapidly to meet the load requirement. As a result, the reactants get consumed quickly. If the rate of consumption exceeds the diffusion rate on the catalyst surface, the FC becomes incapable of delivering a current beyond that particular point. This current is called limiting current. The relation is described as:

$$V_{conc} = \frac{RT}{2F} ln\left(\frac{i_L}{i_L - 1}\right) \tag{3.13}$$

### 3.1.2 BoP system design, and modeling

To simulate the steady state behavior of the FC system, the BoP is modeled using GT-Suite software. First, the calibrated single cell model is scaled up from 1 $cm^2$ to a larger size of 240 $cm^2$. The selection of the 240 $cm^2$ cell area is based on reference FC [47], which serves as a benchmark for scalability. Furthermore, to meet the specified power requirement of 150 kW, the number of cells needed in the system is calculated based on equation 3.14. These number of cells ensures that the scaled-up FC system will deliver the desired power output.

$$P_{nom} = nV_{cell} \times i \times A_{cell} \tag{3.14}$$

$$n = \frac{P_{nom}}{V_{cell} \times i \times A_{cell}} \tag{3.15}$$

where :

| | |
|---|---|
| $n$ | is number of cells, |
| $i_d$ | is nominal current density = 1 $A/cm^2$, |
| $A_{cell}$ | is single cell area = 240 $cm^2$, |
| $V_{cell}$ | is nominal volt = 0.5 V, |
| $P_{nom}$ | is nominal power = 150 kW. |

substituting the above values in equation 3.15 gives the total number of cells, $n$ is equal to 1250. The cell to system scaling is performed using predictive modeling technique, that uses the physical characteristics of the FC's MEA to predict the performance. For efficient design, and modeling of the FC, the system is explored separately in three different subsystems as airflow system, $H_2$ system, and cooling system.

#### 3.1.2.1 Air flow system

In the aforementioned section, it is clarified that air is provided by an air compressor, specifically a centrifugal compressor. This compressor is driven by an electric motor, regulated by a proportional integral (PI) controller to maintain the desired stoichiometry. The schematic of the air-flow system is shown in figure 3.2, where centrifugal compressors exhibit notable pressure-flow rate characteristics, as they are not operated in the low-flow region situated to the left of the surge line.
In this particular design, it becomes imperative to regulate both the flow, and pressure in order to keep the operating point to the right of the compressor surge line.

This feature allows for enhanced compressor efficiency by manipulating both flow rate, and pressure, enabling high efficiencies across a wide range of flow rates. Similar to the $H_2$ supply, the air supply necessitates humidification to meet performance requirements. In this arrangement, a gas-to-gas humidifier is employed, capitalizing on the presence of liquid water in the air to humidify the incoming dry gases from the heat exchanger. The liquid water can be easily separated from the exhaust air using a simple method.

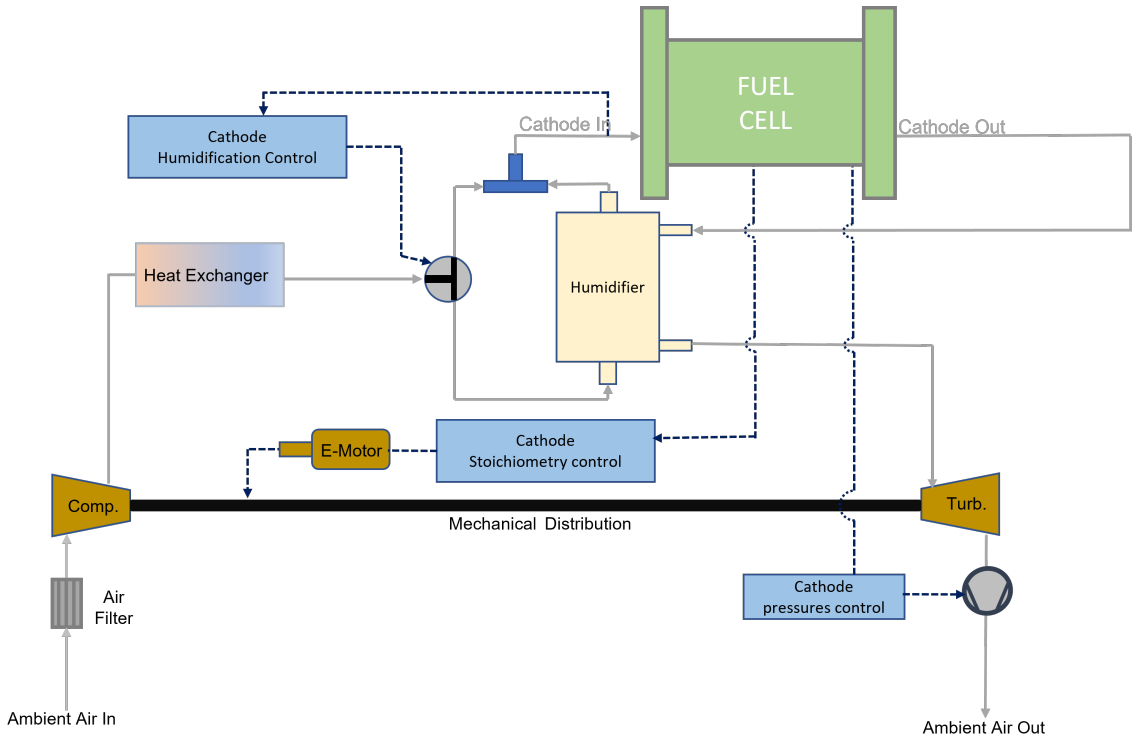


**Figure 3.2:** Schematic of airflow system

Considering the system operates under high pressure, the air at the exhaust remains warm, and retains some level of pressure, albeit lower than the inlet pressure. This surplus energy is harnessed by a turbine to generate work, potentially offsetting a portion of the work required for compressing the air. Both the compressor, and the turbine are mounted on the same shaft, creating a turbo. It's important to note that due to the inefficiencies inherent in both the compression, and expansion processes, as well as the pressure drop throughout the stack, a turbine may only recover a fraction of the compression work.

- **Air Filter**
  In the model, the pressure drop is defined by effective orifice diameter under the assumption of incompressible flow. This is calculated by considering the pressure, flow rate, and reference density. Since the simulation focuses on static conditions, this model provides a good approximation for the pressure drop.
- **Compressor**
  The modeled compressor in this study is a radial type, and its performance

characteristics are represented by a map. The map is created through simulation or experimental data, and is used to predict parameters such as mass flow rate, outlet temperature, and power consumption. The lookup map is obtained from a compressor designed for a 150 kW system [47]. To maintain the humidity, and proper operation of the FC the map is extrapolated to allow the compressor to operate within the compressor map. The pressure map is extrapolated based on equation 3.16.

$$PR_{scaled} = min(1, P_{Data,min}) + PR_{multiplier}(PR_{orig.} - min(1, P_{Data,min})) \quad (3.16)$$

where:

| | |
|---|---|
| $PR_{scaled}$ | is scaled pressure, |
| $P_{Data,min}$ | is inital minimum pressure, |
| $P_{Data,max}$ | is inital maximum pressure, |
| $PR_{orig.}$ | is original pressure, |
| $PR_{multiplier}$ | is multiplier. |

Additionally, the speed, and mass flow rate of the compressor is corrected with respect to a reference condition, to estimate the corrected power, as defined by equations 3.17, and 3.18.

$$RPM_{comp-corc.} = RPM_{comp-act.} \times \sqrt{\frac{T_{ref}}{T_{inlet}} \frac{\gamma_{ref}}{\gamma_{actual}} \frac{R_{ref}}{R_{actual}}} \quad (3.17)$$

$$\dot{m}_{comp-corc.} = \dot{m}_{comp-act.} \times \frac{P_{ref}}{P_{inlet}} \times \sqrt{\frac{T_{ref}}{T_{inlet}} \frac{\gamma_{ref}}{\gamma_{actual}} \frac{R_{ref}}{R_{actual}}} \quad (3.18)$$

where:

| | |
|---|---|
| $RPM_{comp-corc.}$ | is compressor's corrected RPM, |
| $RPM_{comp-act.}$ | is compressor's acutal RPM, |
| $\dot{m}_{comp-corc.}$ | is corrected mass flow rate, |
| $\dot{m}_{comp-act.}$ | is compressor's actual mass flow rate. |

- **Turbine**
  Turbine is similarly modelled based on the characteristic map which is obtained from the e-turbo design of 150 kW FC [47]. Additionally, the speed, and mass flow rate is corrected with respect to a reference condition, for corrected power estimation as defined by equations 3.19, and 3.20.

$$RPM_{turb-corc.} = \frac{RPM_{turb-act.}}{\sqrt{T_{inlet}}} \times \sqrt{\frac{\gamma_{ref}}{\gamma_{actual}} \frac{R_{ref}}{R_{actual}}} \quad (3.19)$$

$$\dot{m}_{turb-corc.} = \frac{\dot{m}_{turb-act.}\sqrt{T_{inlet}}}{P_{inlet}} \times \sqrt{\frac{\gamma_{ref}}{\gamma_{actual}} \frac{R_{ref}}{R_{actual}}} \quad (3.20)$$

where:

| | |
|---|---|
| $RPM_{turb-corc.}$ | is turbine's corrected RPM, |
| $RPM_{turb-act.}$ | is turbine's acutal RPM, |
| $\dot{m}_{turb-corc.}$ | is turbine's corrected mass flow rate, |
| $\dot{m}_{turb-act.}$ | is turbine's actual mass flow rate. |

- **Motor**
  Motor with inverter model enables the transformation of energy from electrical to mechanical form, interacting with various components such as controllers, batteries, and more, to generate the necessary torque for the turbo shaft. Equation 3.21 represents the basic series circuit of motor.

$$L_{EQ}I_A = V_A - R_{EQ}I_A - K_B N_{SHAFT} \tag{3.21}$$

  where:
  $L_{EQ}$ is motor equivalent inductance,
  $R_{EQ}$ is motor equivalent resistance,
  $K_B$ is back voltage coefficient,
  $N_{SHAFT}$ is rotational velocity of motor shaft,
  $I_A$ is armature current.

  In order to regulate the torque exerted on the shaft, the applied voltage $V_A$ is controlled. The operational state of the motor is determined by the sign of the actual power request. A positive power request indicates motor operation, where power is drawn from the connected battery, while a negative power request indicates generator operation, resulting in the charging of the battery. The respective power requests are as follows:

$$P_{request} = V_A I_A + P_{controller} \tag{3.22}$$

  where:
  $P_{request}$ is requested power,
  $P_{controller}$ is controller power.

$$V_A = \begin{cases} V_B & Act - Pos = 0 \\ \frac{Act-Pos}{100} \times (V_{max} - V_B) + V_B & Act - Pos > 0 \\ \frac{Act-Pos}{100} \times (V_B - V_{max}) + V_B & Act - Pos < 0 \end{cases} \tag{3.23}$$

  $V_{max}$, and $V_{min}$ is the maximum, and minimum applied voltage, $Act - Pos$ is actuator position, and $V_B$ is back voltage which is the limit for the controller.

- **Stoichiometry control-PI**
  A PI controller is used to regulate, and maintain the desired stoichiometry. The control action produces an output, in this case $V_A$ that is proportional to the error between the desired stoichiometry ratio $\lambda_{cath-targ.}$, and the actual stoichiometry ratio $\lambda_{cath.}$ of the system being controlled. The integral control continuously sums up the error over time, and adjusts the control output accordingly. The PI controller allows to maintain the steady state, and reduces the disturbances, and control the flow within the desired map.

$$\frac{dx_\lambda}{dt} = e_\lambda \tag{3.24}$$

$$e_\lambda = \lambda_{cath-targ.} - \lambda_{cath.} \tag{3.25}$$

$$V_A = K_{P\lambda-C}(e_\lambda) + K_{I\lambda-C}(x_\lambda) \tag{3.26}$$

- **Cathode pressure control-PI**
  To maintain the desired pressure inside the FC, the exhaust valve's opening is controlled by PI controller. The controller regulates the valve opening $Pos_{valout}$ that is proportional to the error between the desired cathode pressure $P_{cath-targ.}$, and actual cathode pressure $P_{cath}$. The integral control continuously sums up the error over time, and adjusts the control output accordingly. The PI controller allows to maintain the steady state, and reduces the disturbances, and control the flow within the desired map.

$$\frac{dx_{Pc}}{dt} = e_{Pc} \tag{3.27}$$

$$e_{Pc} = P_{cath-targ.} - P_{cath} \tag{3.28}$$

$$Pos_{vout} = K_{Ppress.}(e_{Pc}) + K_{Ipress.}(x_{Pc}) \tag{3.29}$$

- **Humidification control**
  Humidification control strategy for 80 ℃:
  A gas-to-gas humidifier system comprises a shell, and tube configuration. The transfer of water molecules from the wet side to the dry side is facilitated by a membrane made of the same material as the FC (Nafion). Additionally, a simple heat transfer correlation is established between the wet, and dry gases. To ensure proper humidity levels, a PI controller is utilized in conjunction with a bypass valve. This controller regulates the opening of the valve, denoted as $Pos_{bRHv}$. The proportional control component adjusts the opening of the bypass valve based on the difference between the cathode's relative humidity $RH_{C-targ.}$, and the incoming air's relative humidity at the cathode end $RH_{Cin}$. This difference is compared to the desired inlet air relative humidity required for the air supplied to the FC. Simultaneously, the integral control continuously accumulates the error over time, and modifies the control output accordingly. This combined action of proportional, and integral control ensures precise, and stable control of the humidity level within the system. The control of the humidifier valve, and the bypass valve is detailed below:

$$\frac{dx_{posbp}}{dt} = e_{posbp} \tag{3.30}$$

$$e_{posbp} = RH_{C-targ.} - RH_{Cin} \tag{3.31}$$

$$Pos_{bRHv} = K_{PPRH}(e_{posbp}) + K_{IPRH}(x_{posbp}) \tag{3.32}$$

$$Pos_{bRHv2} = 50 - Pos_{bRHv} \tag{3.33}$$

  where:
  $Pos_{bRHv}$ is position of $1^{st}$ valve,
  $Pos_{bRHv2}$ is position of bypass valve.

  Humidification control strategy for 100, and 120 ℃:
  Schematic representation of the control used for secondary heat exchanger is shown in figure 3.3. During the operation of the FC at IT, the exhaust air does not possess an adequate amount of water molecules to transport to

the incoming dry air in the humidifier. To address this issue, a secondary heat exchanger with a bypass control system is devised. This setup effectively lowers the temperature of the exhaust gas, resulting in the condensation of water vapor. Consequently, this process humidifies the incoming air, ensuring a sufficient level of moisture is attained. Control of secondary heatexchanger is described below:

$$\frac{dx_{pos2bp}}{dt} = e_{pos2bp} \tag{3.34}$$

$$e_{pos2bp} = RH_{C-targ.} - RH_{Cin} \tag{3.35}$$

$$Pos_{b2RHv} = K_{P2RH}(e_{pos2bp}) + K_{I2RH}x_{pos2bp} \tag{3.36}$$

$$Pos_{b2RHv2} = 50 - Pos_{b2RHv} \tag{3.37}$$

where:

$Pos_{b2RHv2}$ is position of secondary heater inlet valve,

$Pos_{b2RHv}$ is position of secondary bypass valve.

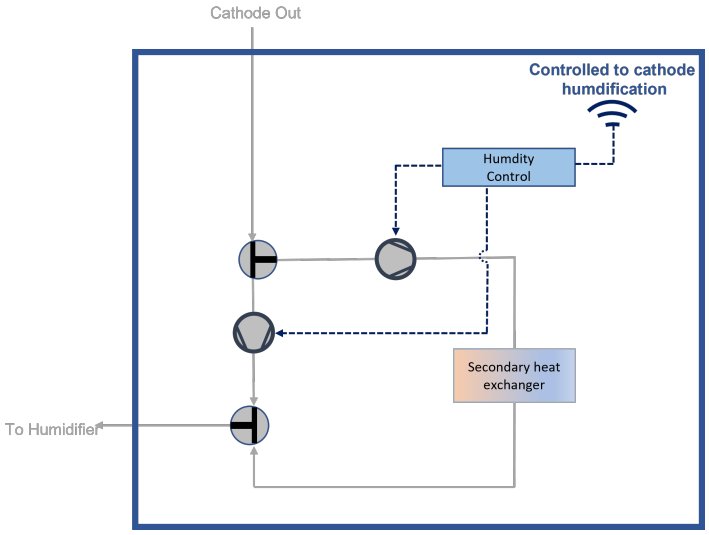


**Figure 3.3:** Schematic of humidification control for intermediate temperature

### 3.1.2.2 Hydrogen flow system

In FC systems, $H_2$ is generated elsewhere, and then stored within the system. As explained in section 2.3.2.1, the prevailing method of $H_2$ storage for automotive applications involves high-pressure cylinders. The schematic of $H_2$ flow system is presented in figure 3.4. Two pressure standards have been established: 350, and 700 bar. For the present simulation study, the 350 bar standard is employed. Upon being released from the storage tank, $H_2$ undergoes pressure reduction through a regulated system. In the following design, temperature control is integrated into the regulator, with the boundary condition set to the respective temperature. To prevent the accumulation of impurities, and foreign substances, $H_2$ is directed through the stack (S > 1), while unused $H_2$ is returned using an active recirculation pump. This technique is safer, and more efficient in the long run compared to $H_2$ purging. Before

entering the FC stack, $H_2$ typically needs to be humidified up to 100% RH. This is necessary to avoid membrane drying caused by electroosmotic drag. The level of humidity is regulated through the recirculation flow, ensuring optimal conditions within the system.

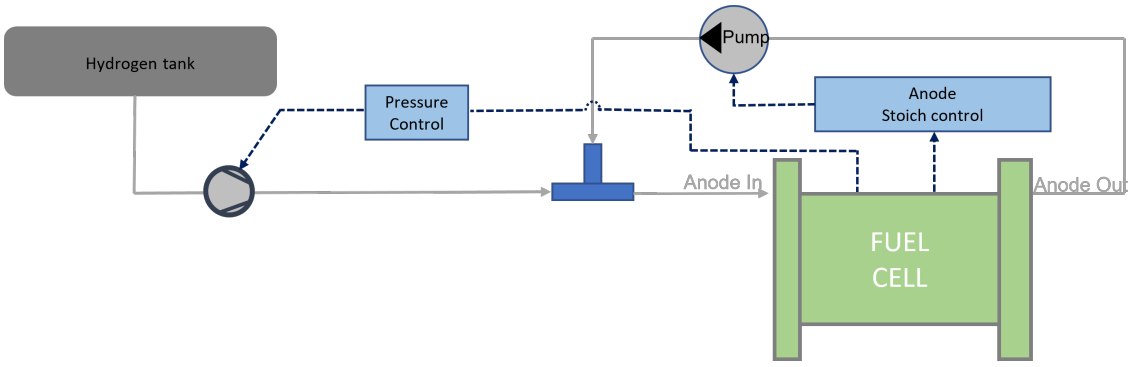


**Figure 3.4:** Schematic for $H_2$ flow

- **Hydrogen pressure control**
  To maintain the desired $H_2$ pressure at the FC, the $H_2$ valve $Pos_{Pval}$ is regulated by PI controller.

$$\frac{dx_{AP}}{dt} = e_{AP} \tag{3.38}$$

$$e_{AP} = P_{AP-targ.} - P_{AP} \tag{3.39}$$

$$Pos_{Pval} = K_{P-HP}(e_{AP}) + K_{I-HP}(x_{AP}) \tag{3.40}$$

- **Recirculation pump, and stoichiometry control**
  The recirculation pump is modelled with a specific volumetric flow rate applied at a particular location within the feedback loop. The determination of these flow rates is based on the desired stoichiometry at the anode side, which is regulated by the PI controller. Power consumed by the pump is described in the below equation.

$$P_{H_2,out} = \dot{m}(h_{H_2,out} - h_{H_2,in}) \tag{3.41}$$

$$h_{H_2,out} = h_{H_2,in} + \Delta h_{H_2,s}\frac{1}{\eta_s} \tag{3.42}$$

$$\Delta h_{H_2,s} = c_p T_{total,in}\left[\left(\frac{p_{H_2,out}}{p_{H_2,in}}\right)^{\left(\frac{k-1}{k}\right)} - 1\right] \tag{3.43}$$

where:

| | |
|---|---|
| $P_{H_2,out}$ | is the required power, |
| $h_{H_2,out}$ | is $H_2$'s outlet enthalpy, |
| $h_{H_2,in}$ | is $H_2$'s inlet enthalpy, |
| $\Delta h_{H_2,s}$ | is isentropic enthalpy change, |
| $k$ | is ratio of specific heats, |
| $\eta_s$ | is isentropic efficiency. |

Volumetric flow rate, $V_{flow}$ input is determined from the active PI control output.

$$\frac{dx_{\lambda-A}}{dt} = e_{\lambda-A} \tag{3.44}$$

$$e_{\lambda-A} = \lambda_{A-targ.} - \lambda_A \tag{3.45}$$

$$V_{flow} = K_{Pvflow}(e_{\lambda-A}) + K_{Ivflow}(x_{\lambda-A}) \tag{3.46}$$

#### 3.1.2.3 Coolant system

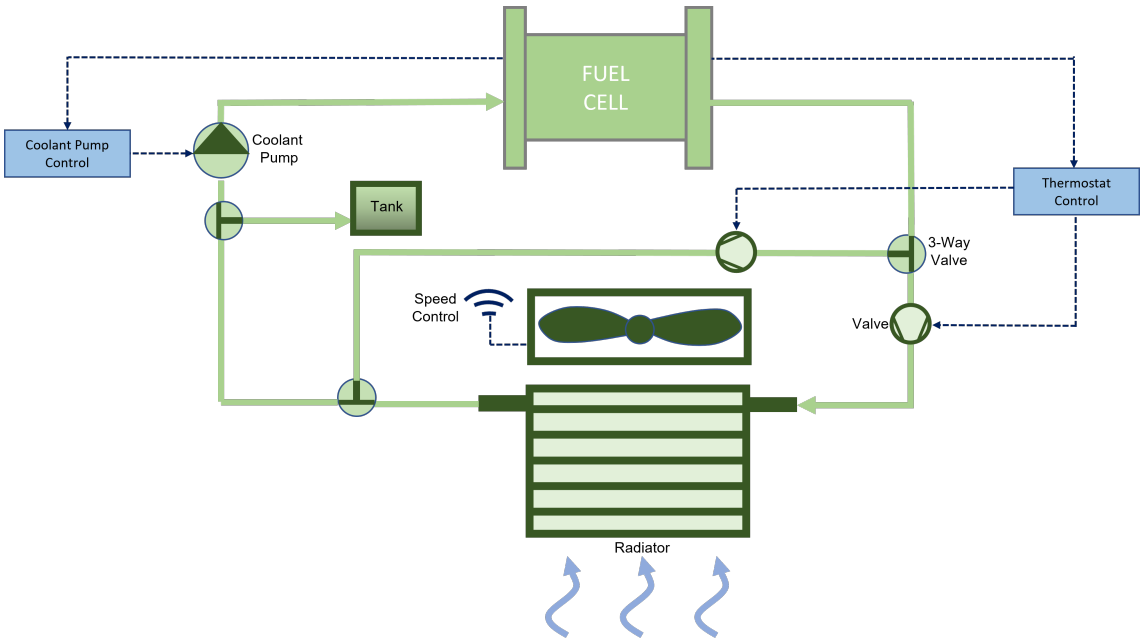


**Figure 3.5:** Schematic of cooling system

- **Radiator**
  A comprehensive model of the radiator is developed in GT-Suite. The model takes into account the thermal capacitance of the radiator walls, and the conductivity properties of the selected material. The temperature of the structure within the heat exchanger is determined by considering the heat transfer balance between the structure, and the two fluids involved. This balance is calculated using a set of equations 3.47 that govern the heat transfer process.

$$\frac{dT_{wall}}{dt} = \frac{Q_m + Q_s}{\rho V C_p} \tag{3.47}$$

$$\frac{dT_{wall}}{dt} = \frac{\left[\left(\frac{hA_{base}+\eta_{fin}hA_{fin}}{1+hR_f}\right)\Delta T - \frac{2kA_c\Delta T_w}{t}\right]_m + \left[\left(\frac{hA_{base}+\eta_{fin}hA_{fin}}{1+hR_f}\right)\Delta T - \frac{2kA_c\Delta T_w}{t}\right]_s}{\rho V C_p} \tag{3.48}$$

where:

| | |
|---|---|
| $A_{base}$ | is base heat transfer area (not including fins), |
| $A_c$ | is thermal cross-sectional conduction area, |
| $A_{fin}$ | is fin heat transfer area, |
| $h$ | is fluid heat transfer coefficient, |
| $C_p$ | is heat capacity of the wall material, |
| $k$ | is thermal conductivity of the wall material, |
| $\eta_{fin}$ | is fin efficiency, |
| $\rho$ | is density of the wall material, |
| $R_f$ | is fouling resistance, |
| $t$ | is tube thickness, |
| $T_w$ | is temp. diff. between the surface, and wall, |
| $\eta_s$ | is isentropic efficiency, |
| $V$ | is volume of the wall material. |

The modeling of pressure loss encompasses two main components: friction loss, and expansion/contraction effects. Friction loss is accounted for using an empirical friction model selected for the specific application, along with a calibrated friction multiplier. The expansion, and contraction terms are automatically calculated based on the provided geometry setup but are also fine-tuned through the use of a discharge coefficient. The placement of the discharge coefficient is crucial, and depends on the specific geometry configuration in order to accurately capture the pressure loss phenomenon.
Pressure drop equation for internal flow:

$$\begin{aligned}\Delta P = &\left(\frac{\rho_{in}}{2}\left(\frac{\dot{m}_{in}}{\rho_{in}A_{core}}\right)^2\right) + \left(\sum\left(\frac{C_f}{2}f_m\rho_{core}\mu_{core}^2\frac{A_{surface}}{A_{core}}\right)\right) \\ &+ \left(\frac{\rho_{out}}{2}\left(\frac{\dot{m}_{out}}{C_{D,c}\rho_{out}A_{ref}}\right)^2\right) + (\rho_{out}\mu_{out}^2 - \rho_{in}\mu_{in}^2)\end{aligned} \tag{3.49}$$

Pressure drop equation for external flow:

$$\begin{aligned}\Delta P = &\left(\frac{\rho_{up}}{2}\left(\frac{\dot{m}_{up}}{C_{D,c}\rho_{up}A_{core}}\right)^2 - \frac{\rho_{up}{\mu_{up}}^2}{2}\right) + \left(\frac{\sum\left(\frac{C_f}{2}f_m\rho_{core}\mu_{core}^2\frac{A_{surface}}{A_{core}}\right)}{n}\right) \\ &- \left(\frac{\sum\left(2\frac{A_{core}}{A_{ref}}\left(1-\frac{A_{core}}{A_{ref}}\right)\frac{\rho_{out}{\mu_{out}}^2}{2}\right)}{n}\right) + (\rho_{out}\mu_{out}^2 - \rho_{in}\mu_{in}^2)\end{aligned} \tag{3.50}$$

where:

| | |
|---|---|
| $A_{core}$ | is core subvolume flow area, |
| $A_{ref}$ | is outlet reference pipe area, |
| $A_{surface}$ | is core subvolume surface area, |
| $C_f$ | is fanning friction factor, |
| $C_{D,c}$ | is calibrated discharge coefficient, |
| $f_m$ | is friction multiplier, |
| $\dot{m}_{in}$ | is inlet mass flow rate, |
| $\dot{m}_{out}$ | is outlet mass flow rate, |
| $\dot{m}_{up}$ | is inlet (upstream) mass flow rate, |
| $\Delta P$ | is pressure drop, |
| $\rho_{core}$ | is core subvolume density, |
| $\rho_{in}$ | is inlet core density, |
| $\rho_{out}$ | is outlet core density, |
| $\mu_{core}$ | is core subvolume velocity, |
| $\mu_{in}$ | is inlet subvolume velocity, |
| $\mu_{out}$ | is outlet subvolume velocity. |

- **Coolant pump**
  Coolant pump is modelled based on measured performance data that correlates pump speed, flow rate, pressure rise, and efficiency. It is modelled as a mechanical pump with imposed speed signals. Different power terms calculated from the pump template. Average theoretical power, $P_{cool,th}$, is the minimum power necessary to pump the fluid from inlet to outlet assuming a perfect process.

$$P_{cool,th} = \dot{m}_{cool} \Delta h_{cool,s} \tag{3.51}$$

$$\Delta h_{cool,s} = \frac{p_{cool,out} - p_{cool,in}}{\rho_{cool,in}} \tag{3.52}$$

  where:

| | |
|---|---|
| $\dot{m}_{cool}$ | is mass flow rate of coolant, |
| $\Delta h_{cool,s}$ | is isentropic enthalpy change, |
| $p_{cool,out}$ | is outlet static pressure, |
| $p_{cool,in}$ | is inlet static pressure, |
| $\rho_{cool,in}$ | is inlet static density. |

- **Radiator fan**
  Similar to the pump model, fan is designed with the performance data that consists of flow rate, fan speed, pressure rise, and efficiency. In this study, a mechanical fan is modelled with imposed speeds, set by optimizing the cooling system. Average theoretical power (air), $P_{air,th}$, is the power necessary to move air from inlet to outlet assuming a perfect process.

$$P_{air,th} = \dot{m}_{air} \Delta h_{air,s} \tag{3.53}$$

$$\Delta h_{air,s} = c_p T_{total,in} \left[ \left( \frac{p_{air,out}}{p_{air,in}} \right)^{\left(\frac{k-1}{k}\right)} - 1 \right] \tag{3.54}$$

where:

| | |
|---|---|
| $\dot{m}_{air}$ | is mass flow rate of air, |
| $p_{air,out}$ | is air's outlet static pressure, |
| $p_{air,in}$ | is air's inlet static pressure, |
| $\Delta h_{air,s}$ | is enthalpy change. |

- **Thermal control (coolant flow, and thermostat)**
  As mentioned in section 3.1.2.3, the coolant pump is subjected to a specified flow rate. This flow rate $RPM_{pump}$ is regulated using a PI controller, wherein the desired temperature for the FC, $T_{FCtarget}$, serves as the target, and feedback input, $T_{FCactual}$, and the controller output corresponds to the pump speed. By employing this control mechanism, the coolant pump adjusts its speed to maintain the required temperature for the FC, ensuring optimal operating conditions.

$$\frac{dx_{TFC}}{dt} = e_{TFC} \tag{3.55}$$

$$e_{TFC} = T_{FCtarget} - T_{FCactual} \tag{3.56}$$

$$RPM_{pump} = K_{PTFC}(e_{TFC}) + K_{ITFC}(x_{TFC}) \tag{3.57}$$

  In order to regulate the temperature difference $\Delta$T between the coolant temperature at the inlet $T_{radin}$, and outlet $T_{radout}$ of the radiator, a bypass system incorporating a PI controller is employed. The output of the controller determines the opening of the bypass valve $Pos_{bTv}$, which governs the flow of coolant through the radiator to maintain the desired temperature. This control mechanism ensures effective temperature management within the cooling system.

$$\frac{dx_{Trad}}{dt} = e_{Trad} \tag{3.58}$$

$$e_{Trad} = T_{radout} - T_{radin} \tag{3.59}$$

$$Pos_{bTv} = K_{Ppbv}(e_{Trad}) + K_{Ipbv}(x_{Trad}) \tag{3.60}$$

#### 3.1.2.4 Optimization

- **Optimisation of the e-turbo:**
  Once the compressor map, turbine map, and the base design profile is implemented in the GT-Suite, initial boundary conditions for pressure, and mass flow rates $O_2$ stoichiometry are set, allowing to perform the simulation of the FC system. Reference mass flow, and efficiency maps are shown in figure 3.6, 3.7, 3.8, and 3.9. During this simulation, various aspects such as air flow, compressor surge area, and efficiency, turbine operating point, and FC performance are evaluated to identify potential areas for improvement.

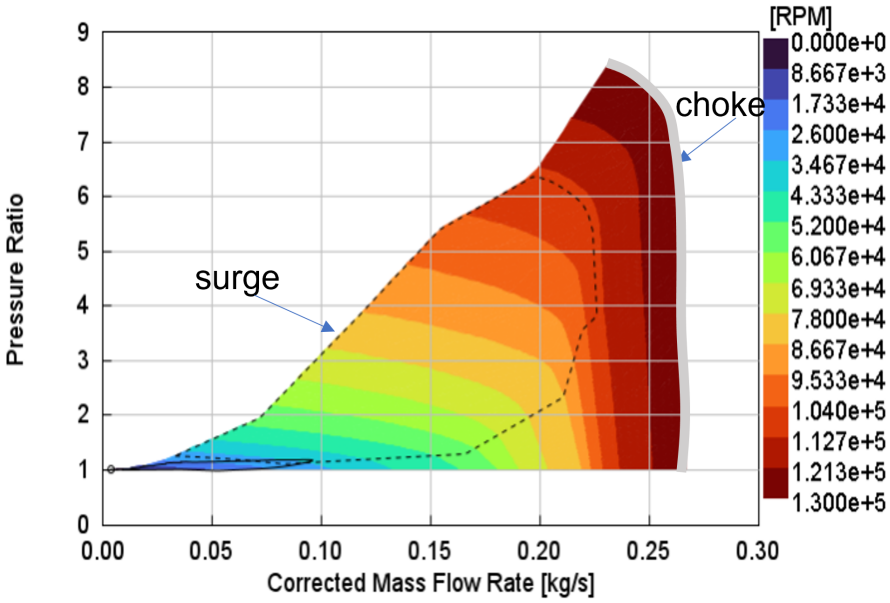


**Figure 3.6:** Corrected speed map of compressor

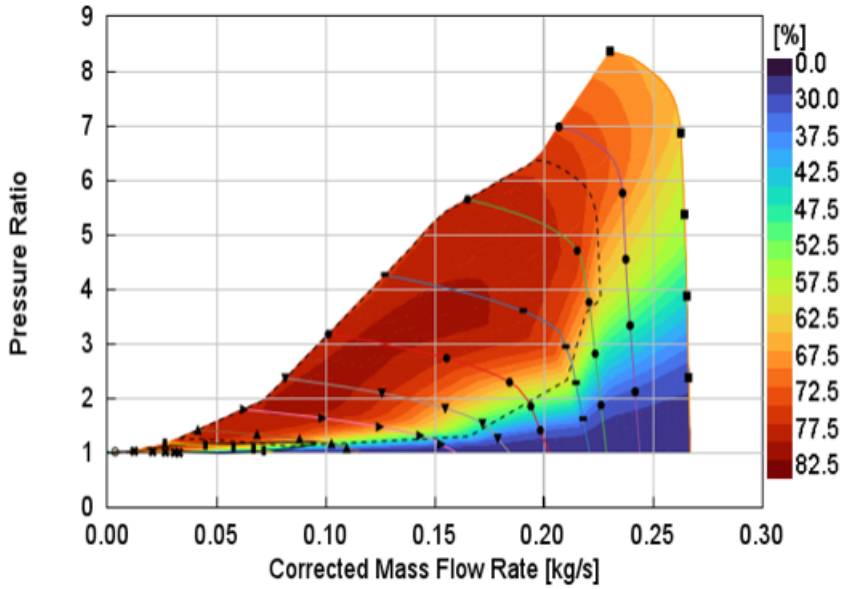


**Figure 3.7:** Corrected efficiency map of compressor

If it is determined that FC performance can be enhanced, optimization is carried out for pressure, and $O_2$ stoichiometry while keeping the compressor power consumption the least. However, if the compressor operating point lies outside the surge operating zone in figure 3.6, initial optimization is performed for pressure, and stoichiometry. If no improvement is observed, further optimization is conducted by adjusting the size of the compressor. At the same time, a good efficiency point is validated which fits within the surge region.

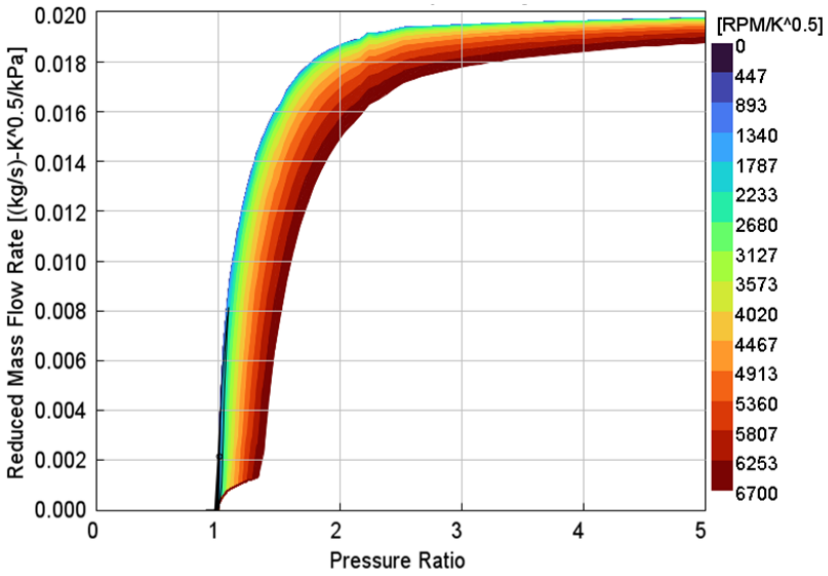


**Figure 3.8:** Corrected speed map of turbine

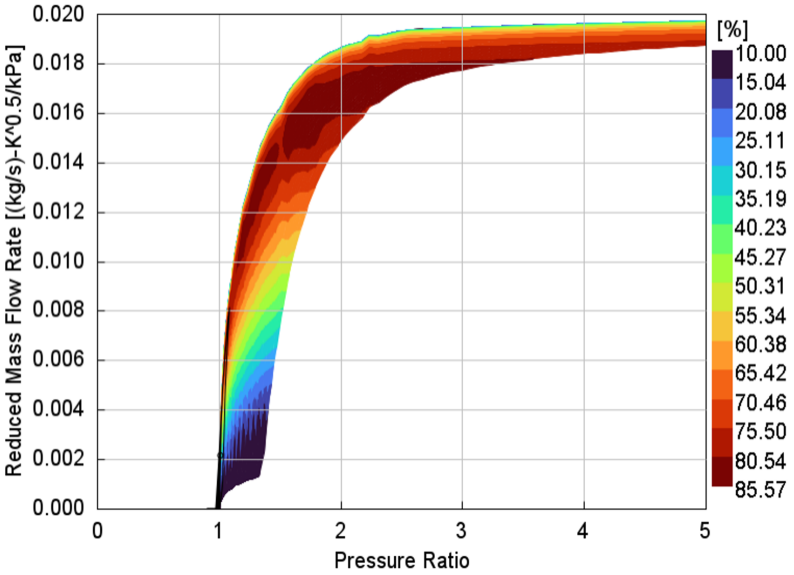


**Figure 3.9:** Corrected efficiency map of turbine

Turbine operating point is not restricted from the surge zone, however, its important to hold the flow, and speed in the defined map. Turbine, operation is interlinked with the compressor boundary condition. To ensure that these changes do not significantly impact the overall performance of the FC system or other operating conditions, simulations are repeated for the respective points with the adjustments implemented. This iterative process allows for the assessment, and refinement of the FC system to achieve optimal performance. Iterative process followed for the optimization of the e-turbo is presented in the below figure 3.10.

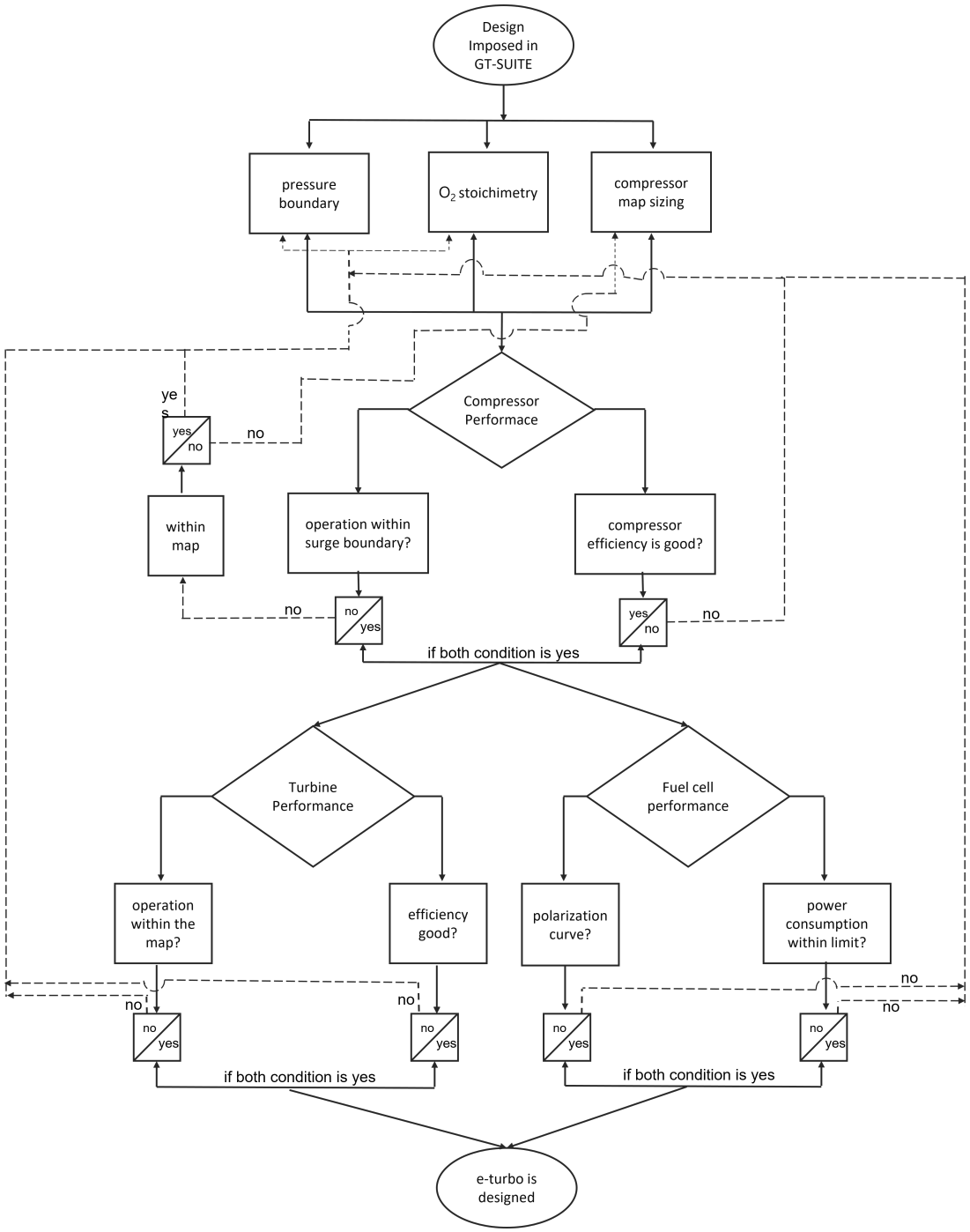


**Figure 3.10:** e-turbo optimization process

- **Optimisation of the coolant pump, and radiator fan:**
  Upon successfully incorporating the coolant, and radiator fan design, and mapping into the GT-Suite software, an initial boundary condition is set for the radiator fan speed. Respective maps are shown in figure 3.11, 3.12, 3.13, and 3.14.

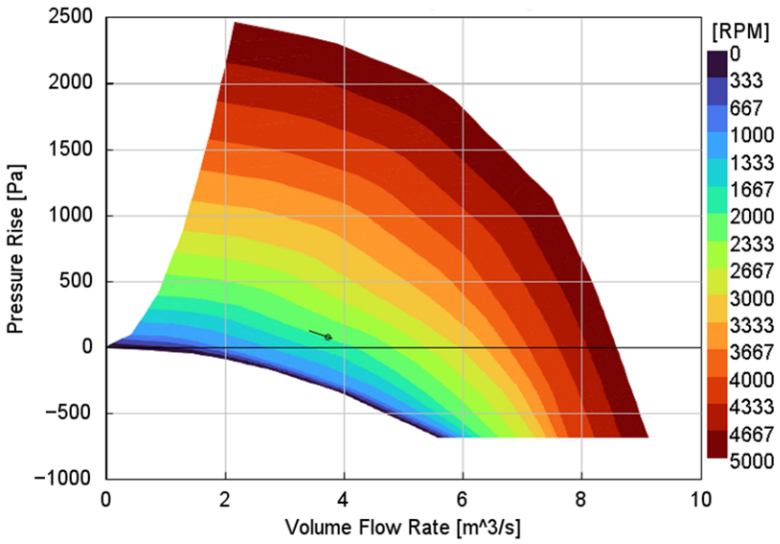


**Figure 3.11:** Corrected speed map of radiator fan

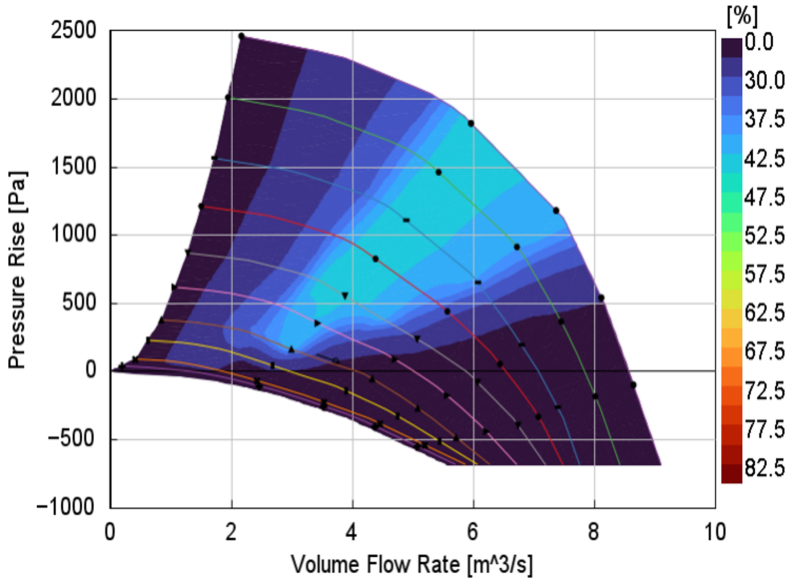


**Figure 3.12:** Corrected efficiency map of radiator fan

This enables the integration of the complete cooling system simulation with the FC system. During this simulation, various aspects such as coolant flow, air flow, operating points on the corresponding maps, and the cooling effectiveness at the radiator is assessed to identify potential areas for enhancement.

If it is determined that the fan's power consumption can be improved, optimization is conducted by adjusting the imposed speed while maintaining a constant temperature difference $\Delta T$ around the radiator. If the maximum power of the radiator fan or the coolant pump is reached without achieving the desired cooling system effectiveness, further optimization is pursued by considering adjustments to the size of the components. To ensure that these modifications do not significantly impact the overall performance of the FC system or other operating conditions, simulations are repeated for the relevant points with the implemented changes.

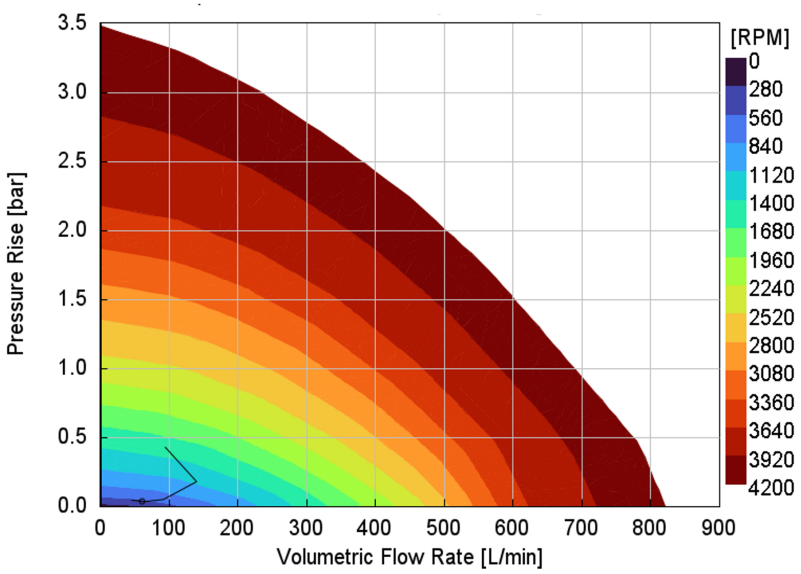


**Figure 3.13:** Corrected speed map of coolant pump

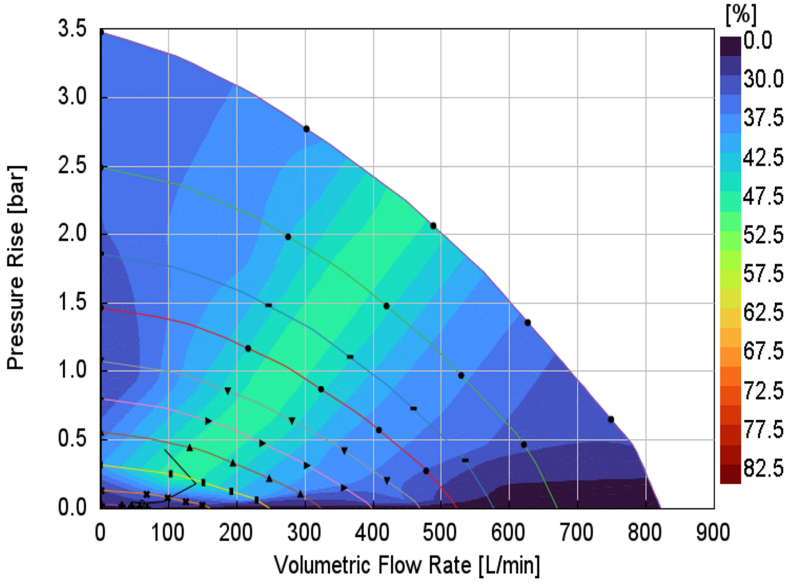


**Figure 3.14:** Corrected efficiency map of coolant pump

This iterative process facilitates the evaluation, and refinement of the FC system, aiming to achieve optimal cooling system performance as presented in figure 3.15.

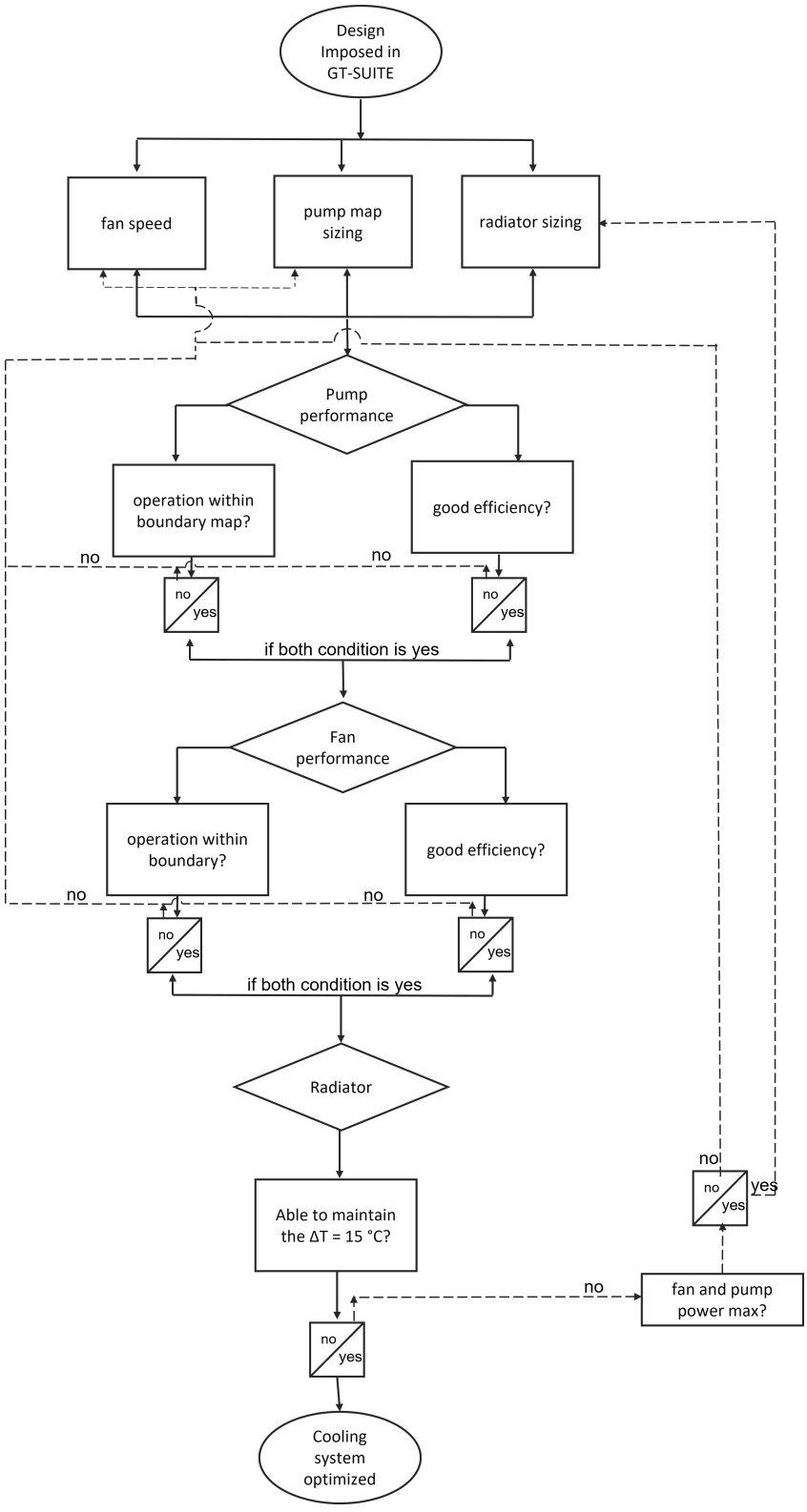


**Figure 3.15:** Cooling system optimization

## 3.2 Calibration

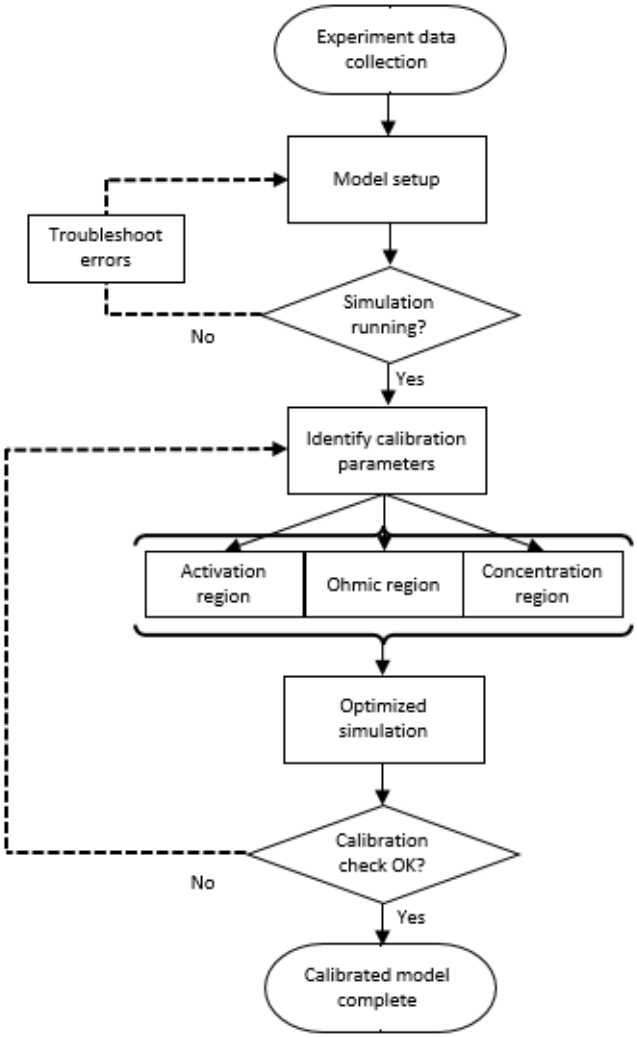


**Figure 3.16:** Calibration flowchart

### 3.2.1 Data collection

Prior to the commencement of the thesis, experiment on IT-PEMFC was being conducted at KTH Royal Institute of Technology. To begin with, data necessary for single cell calibration is acquired from the researchers. The data consists of polarization curves for 80, 100, and 120 ℃ as well as flow parameters, and cell component specifications that are inputs in the model 3.1. Other parameters that are required to build the model is mentioned in table 3.2.

**Table 3.1:** Experiment inputs in the model [45]

| Input | Details | Unit | Remarks |
|---|---|---|---|
| Flow parameters | Pressure | bar | Cathode (air)=2<br>Anode ($H_2$)= 2 |
| | Mass flow rate | ml/min | Cathode (air)= 200<br>Anode ($H_2$)= 80 |
| | Temperature | ℃ | 80/100/120 |
| | RH | % | 70 |
| Membrane | Material | | Commercially available Nafion |
| | Dry density | g/m$^3$ | 1700000 |
| | Thickness | micron | 10 |
| | Length of the manifold | mm | 100 |
| | Material used | | Graphite |
| Catalyst | Loading | mg/cm$^2$ | Cathode= 0.25; Anode= 0.15 |
| | Specific surface area | cm$^2$/mg | Cathode= 528; Anode= 500 |
| Thermal | Bipolar material/cathode GDL/anode GDL plate | | Graphite |
| GDL | Thickness | micron | 150 |

**Table 3.2:** Other model input parameters

| Input | Details | Unit | Remarks |
|---|---|---|---|
| Flow parameters | Configuration | | Counter flow |
| | Number of segments | | 3 |
| | Length/diameter of header | mm | 4/100 |
| | Channel shape | | Circular |
| | Channel length/dia | mm | 30/4 |
| | Number of channels | | 5 |
| Thermal | Model | | Isothermal |
| | Cell mass | kg | 5 |
| | Bipolar plate mass fraction (mf) | | 0.9 |
| | Anode/cathode GDL mf | | 0.05 |
| GDL | Porosity | | 0.75 |
| | Tortuosity | | 1.6 |
| OCV loss | | V | 0.18 |

### 3.2.2 Calibration parameters

The final calibrated system must have one set of defining parameters that best fits the experiment polarization curve for all three operating temperatures. So it is important to first, identify the model parameters that influence each region of loss by running simulation trials. Subsequently, these parameters can be optimized to get the most accurate fit. The observed parameters are catalyst loading, $L_c$, and charge transfer coefficient, $\alpha$ for activation losses, springer coefficient, $b_{11}$ for ohmic losses, and membrane thickness $t_m$ for transport losses. There are also other model inputs that influence the losses practically but cannot be defined through equations.

These are listed in table 3.2. Reasonable values are considered for these parameters pertaining to the experiment, and model setup.

### 3.2.3 Optimization, and curve fit

As indicated in table 3.1, catalyst loading, and membrane thickness are defined attributes in the experiment, and cannot be used in model optimization. This leaves $\alpha$, and $b_{11}$ which can be used for calibration. For the curves to start from the nearest OCV to that of experiment, $\alpha$ is chosen to be 0.5. GT-Suite optimizer is used to obtain a $b_{11}$ value of 0.001175 .

## 3.3 Degradation modeling

A predictive empirical model is developed to estimate the durability of an IT PEMFC, taking inspiration from the model developed by Kim et al.[46] for HT PEMFC. To establish the degradation characteristics, experimental data obtained from KTH University is utilized. The university conducted long-term durability tests at different load conditions (5%, 42%, and 100%), and temperatures (80, and 100 ℃). The voltage drop over time for cells operated at 80, and 100 ℃ is analyzed to construct a proposed durability model. This model is formulated based on a set of three-dimensional polynomial equations specific to each operating temperature. Equation 3.61 is the first step which relates test operational time, t with voltage drop. It consists of four coefficients: third order, second order, first order, and a constant term. These time coefficients, $x_i$ have an exponential relation with cell operating temperature, $T_i$ which is calculated in the second step using equations 3.62 to 3.65.

$$VD(t,T) = x_1 t^3 - x_2 t^2 + x_3 t + x_4 \tag{3.61}$$

To enhance the accuracy of the predictions, load conditions are also considered in the equations. The constants $a_i$, $b_i$, $c_i$, and $d_i$ are manually set to calibrate with the experiment load conditions. The values of these constants are defined in table 3.3 for different operating temperature scenarios.This step aids in refining the model's performance, and ensuring more precise estimates of the voltage drop in the IT PEMFC system.

$$x_1 = \exp\left[(3.565 \times 10^{-3} \times T_i^2) - (0.9947 \times T_i) + a_i\right] \tag{3.62}$$

$$x_2 = -\exp\left[(4.199 \times 10^{-3} \times T_i^2) - (1.2792 \times T_i) + b_i\right] \tag{3.63}$$

$$x_3 = \exp\left[(3.272 \times 10^{-3} \times T_i^2) - (1.0404 \times T_i) + c_i\right] \tag{3.64}$$

$$x_4 = \exp\left[(-1.113 \times 10^{-3} \times T_i^2) - (0.3907 \times T_i) + d_i\right] \tag{3.65}$$

By considering both the operating time, and temperature, the final model predicts the voltage drop for different load conditions.

**Table 3.3:** Degradation equation load constants

| Coefficient | Load (%) | 80 °C | 100 °C | 120 °C |
|---|---|---|---|---|
| $a_i$ | 5 | 23.2 | 34 | 44.8 |
| | 42 | 25 | 35 | 45 |
| | 100 | 25 | 35 | 46 |
| $b_i$ | 5 | 51 | 65 | 77 |
| | 42 | 53 | 65 | 77 |
| | 100 | 53 | 65 | 77 |
| $c_i$ | 5 | 49.4 | 59 | 67.6 |
| | 42 | 48.2 | 59.5 | 69.5 |
| | 100 | 50.5 | 60 | 70 |
| $d_i$ | 5 | 34.5 | 10 | -14.5 |
| | 42 | 30 | 10 | -10 |
| | 100 | 30 | 10 | -10 |

## 3.4 Vehicle integration

Finally the FC system is integrated together with the powertrain, and vehicle model. The representative powertrain model contains two FC stacks, and their BoP components, a battery, a traction motor, and a control system which decides on the power split of the total power request between the FC, and battery. A schematic arrangement of the FCEV can be seen in figure 3.17.

**Table 3.4:** Simulation detail for the vehicle, and battery

| Vehicle/powertrain component | Detail | Unit |
|---|---|---|
| Vehicel load | 44 | ton |
| FC | 300 | kW |
| Battery | 28 | kWh |

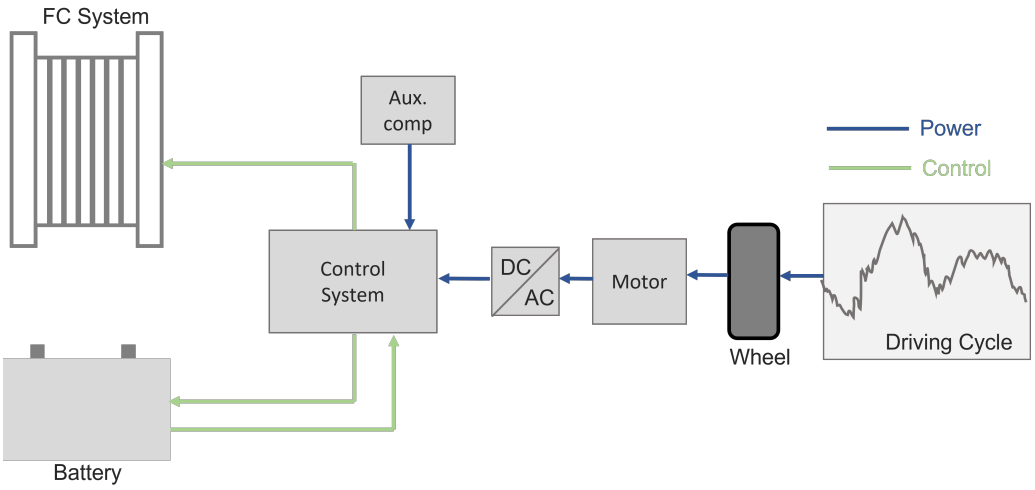


**Figure 3.17:** Schematic of vehicle FC integration to powertrain

# 4

# Results, and discussion

## 4.1 Cell calibration

With the single cell model run on values obtained in section 3.2, the following results from figure 4.1 to figure 4.3 are obtained. On comparing the three plots, it is observed that the model is a good fit for the experiment conducted at 100, and 120 ℃ operating temperature. On the other hand the model at 80 ℃ operation is a good fit at the initial current densities, and deviates away at higher current densities. One explanation is that the GT-Suite calibration model is modeled for 60 to 80 ℃ operating temperature. So the behaviour of 80 ℃ resembles 60 ℃ more than 100, and 120 ℃. Also ohmic, and transport region for 80 ℃ looks too efficient when compared with experimental curve. The transport losses for 120 ℃ also shows the same trend. This is because membrane thickness is predefined in the experiment, and cannot be optimized. A thicker membrane would generally give higher transport losses.

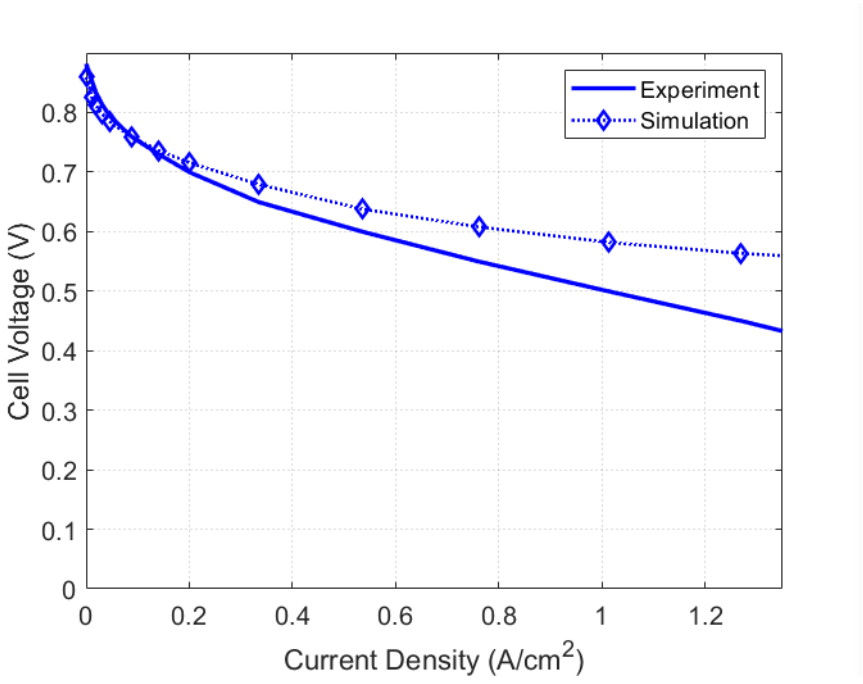


**Figure 4.1:** Cell calibration for 80 ℃ operating temperature

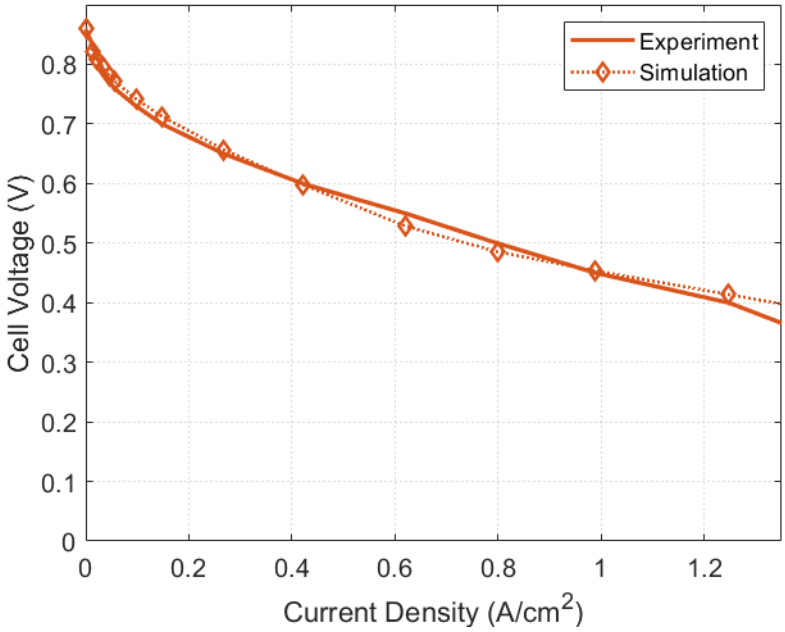


**Figure 4.2:** Cell calibration for 100 ℃ operating temperature

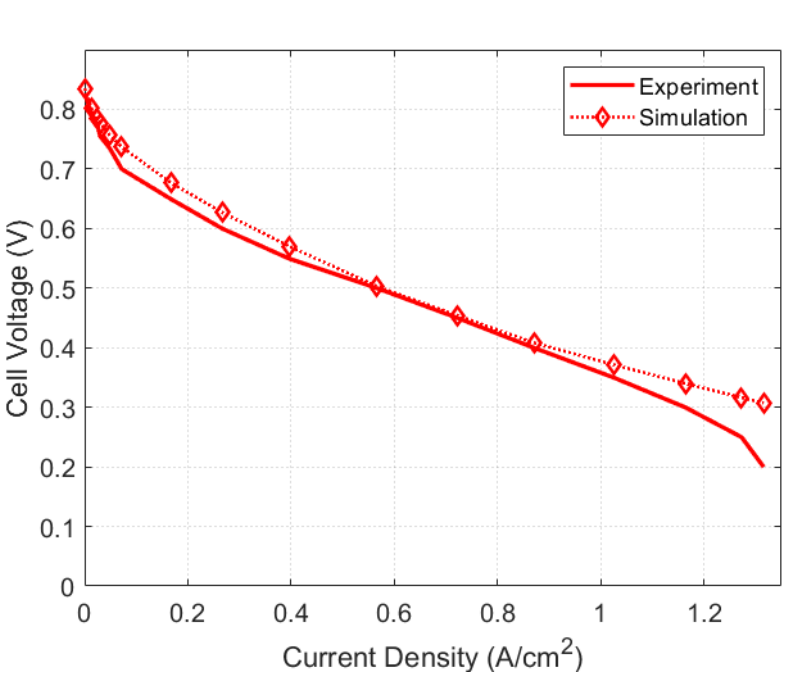


**Figure 4.3:** Cell calibration for 120 ℃ operating temperature

For further analysis, individual losses for each operating temperature are plotted. In general, activation loss is higher for lower operating temperature due to the slow reaction kinetics at the electrochemical interfaces. With increase in temperature, the reactants have higher energy, and move quickly, facilitating reaction kinetics, and thus the reactions. As indicated in figure 4.4, 80 ℃ has higher activation loss

compared to 100, and 120 ℃ operation. But there is no major difference between 100, and 120 ℃. It is because, to maintain the relative humidity of 70%, and pressure of 2 bars at 120 ℃, the partial pressure of oxygen is lower than that of what is required at 100 ℃. This causes some higher losses at 120 ℃ than what is usually expected. The voltage drop is nonlinear due to the exponential relation between exchange current density, and voltage as shown in section 3.1.1.1.

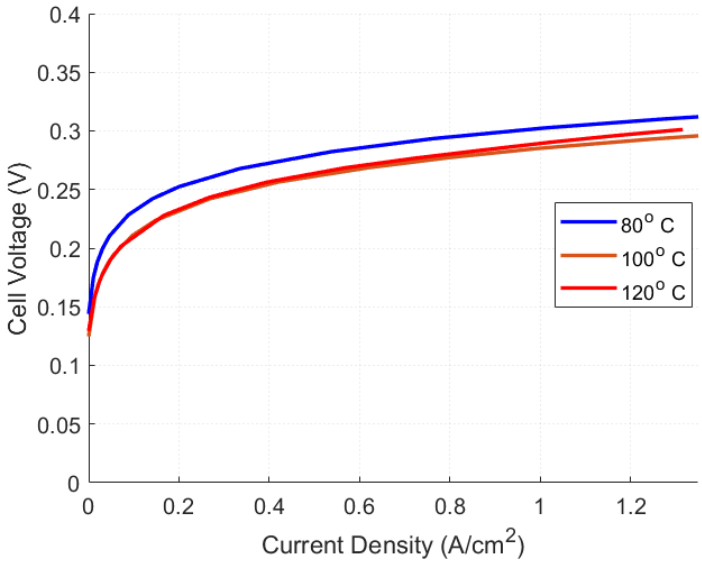


**Figure 4.4:** Activation losses

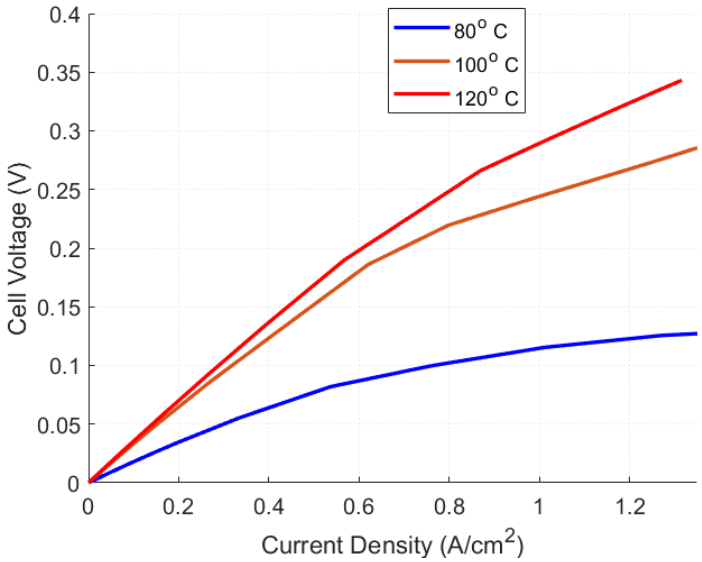


**Figure 4.5:** Ohmic losses

The ohmic polarization in figure 4.5 is opposite to the known trend. With increase in temperature, the losses are increasing. One reason is that, in the model, membrane

conductivity, and water content are considered. At 100, and 120 ℃, the membrane might be dehydrated to maintain good ionic conductivity. Concentration loss is negligible when compared to activation, and ohmic losses mainly due to the fact that the curve is not calibrated for higer current densities. The application region is till a current density of 1 A/cm$^2$.

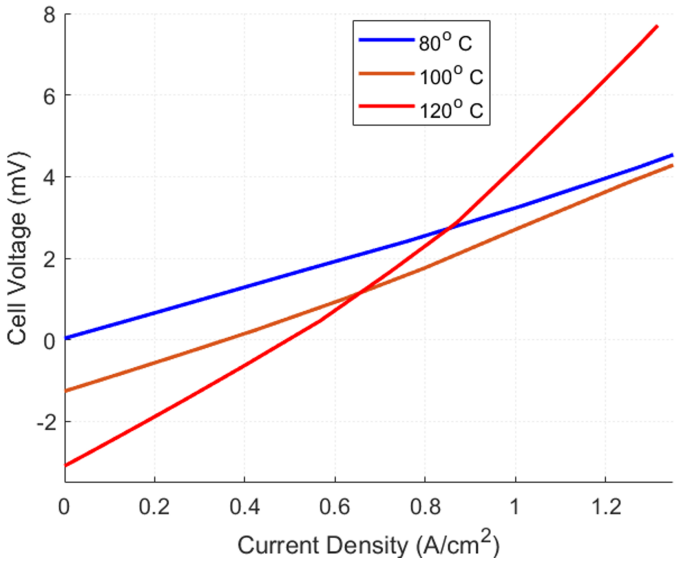


**Figure 4.6:** Transport losses

## 4.2 Cell degradation

The degradation model at 5%, 42%, and 100% loads perfectly reflect the experiment results for 80, and 100 ℃ operating temperature.

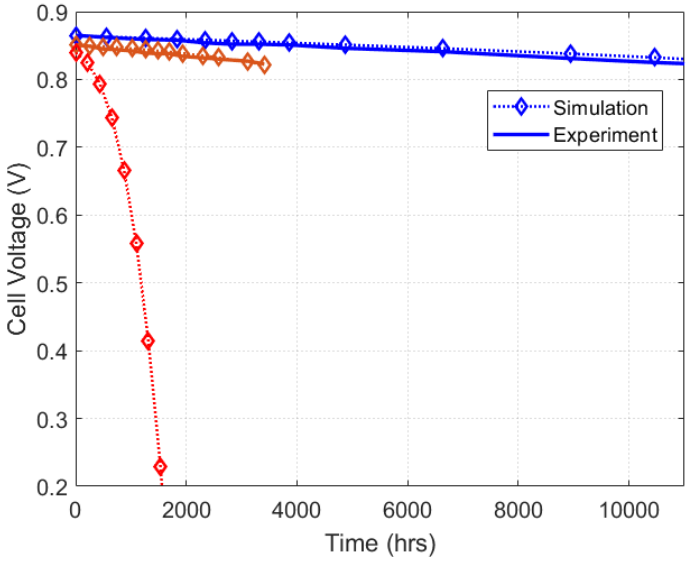


**Figure 4.7:** Cell degradation for 5% load

At these temperatures, the starting voltage drops by 15%, and 30% for 42%, and 100% loads respectively. The explanation is that, at higher loads, the FC has to supply a larger current leading to increase in activation losses. These respective loads are based on operating the FC in the NEDC (Normal European Driving Cycle) cycle. As seen in figure 4.7, the operating voltage drops by 1%, and 3% for 80, and 100 ℃ respectively while operating at FC on 5% load after 3500 hrs.

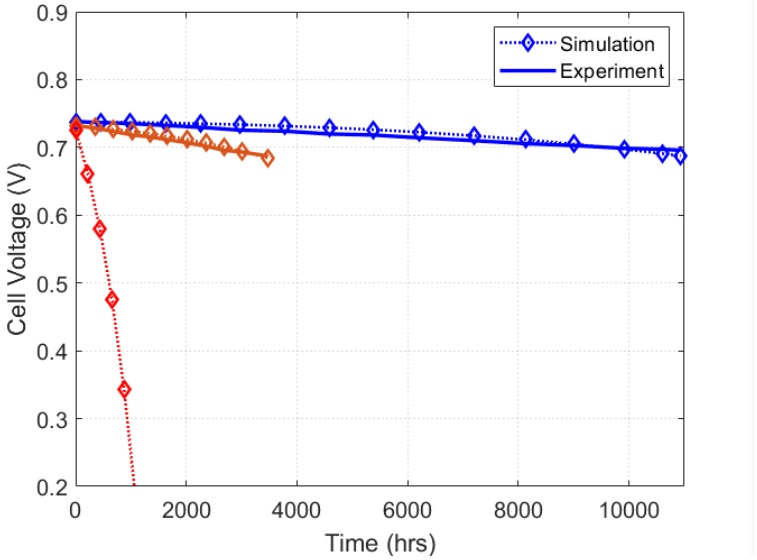


**Figure 4.8:** Cell degradation for 42% load

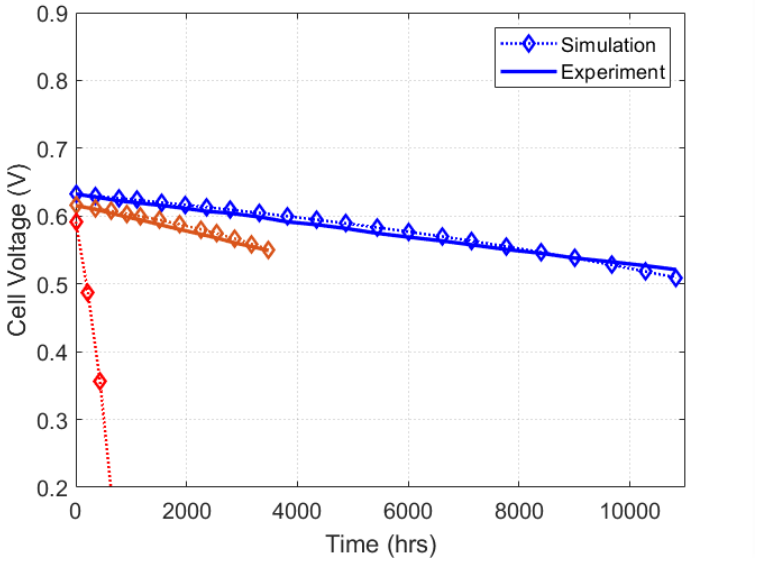


**Figure 4.9:** Cell degradation for 100% load

Secondly, it can be observed in figure 4.8 that the operating voltage decreases by 2%, and 6% for 80, and 100 ℃, respectively after 3500 hours. Furthermore, in figure 4.9, it can be seen that the operating voltage drops by 5%, and 11% for 80, and 100 ℃,

respectively after 3500 hours. Finally, when running the predictive model with an operating temperature of 120 ℃, we observe an exponential decline in the operating voltage, which reflects exponential degradation as observed at all loads. This can be seen in figure 4.7 to 4.9. One important observation from the predictive model is that the degradation is simultaneously influenced by both operating temperature, and load. Operating the FC at 120 ℃ has a severe impact on the FC's lifespan.

## 4.3 System design, and optimization

### 4.3.1 e-turbo design optimization

The design optimization for the e-turbo follows the process outlined in section 3.1.2.4. The optimization begins with a maximum pressure ratio of 4.5 bar. Initially, the focus of the optimization is on the e-turbo while the FC operates at 80 ℃. The results, depicted in figure 4.10, clearly illustrate that all the operating points are effectively within the compressor and turbine map.

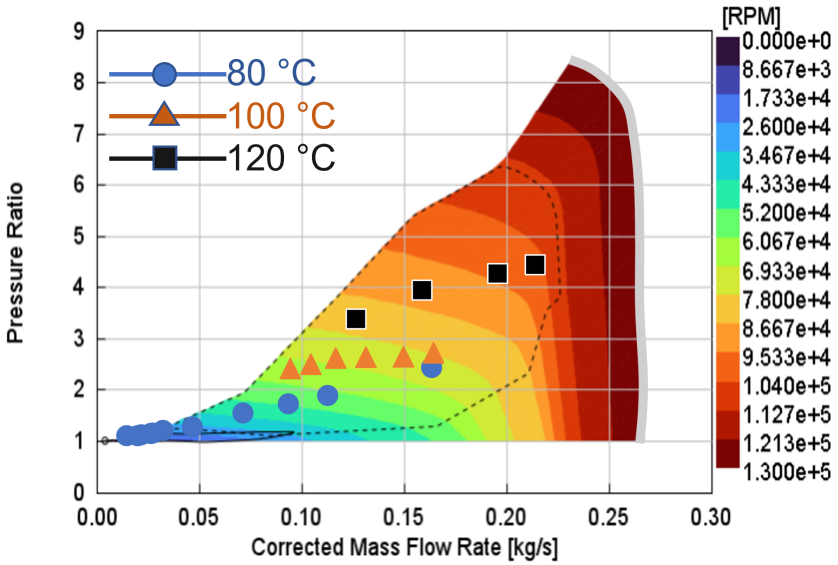


**Figure 4.10:** Operating points on the optimized compressor speed map

However, when the FC is operated at a higher temperature of 100 ℃, a proportional increase in the pressure ratio of 2 bar or more is required to maintain the proper RH for optimal operation. This operational requirement poses difficulties in running the FC at lower current densities, making it impossible to operate at those specific points. Furthermore, operating the FC at 120 ℃ demands an even higher pressure ratio, which exceeds the capacity of the original compressor design. To overcome this challenge, the compressor map was scaled to allow for FC operation at higher temperatures. However, despite scaling the compressor's maximum pressure ratio up to 8 bar, it did not facilitate operation at lower current densities.
After benchmarking the compressor's map, the optimization process was iterated

for all operating temperatures, resulting in the final fit observed in the figures below 4.11 to 4.13.

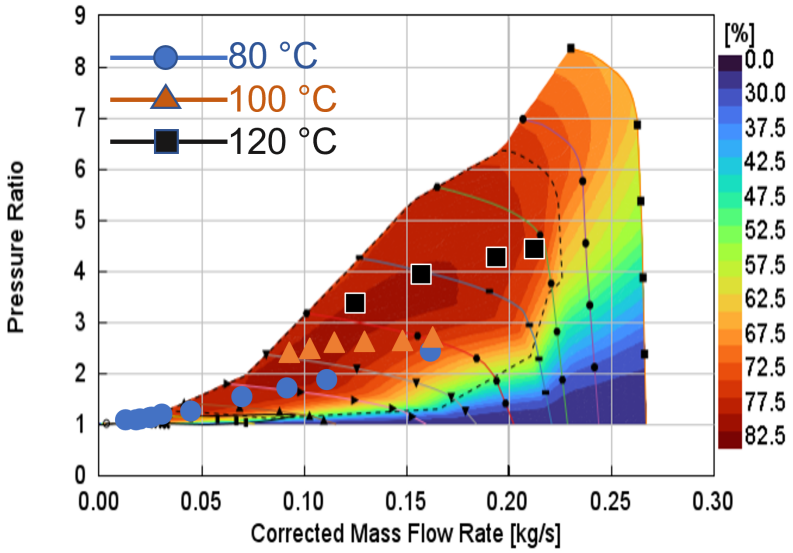


**Figure 4.11:** Operating points on the optimized compressor efficiency map

Interestingly, the initial turbine design is found to be adequate for accommodating all the operating points. However, these points do not correspond directly to the temperature. One possible explanation is that exhaust air temperature decreases after coming out of the secondary heat exchanger. Secondly, the mass flow rate is restricted due to the added inclusion.

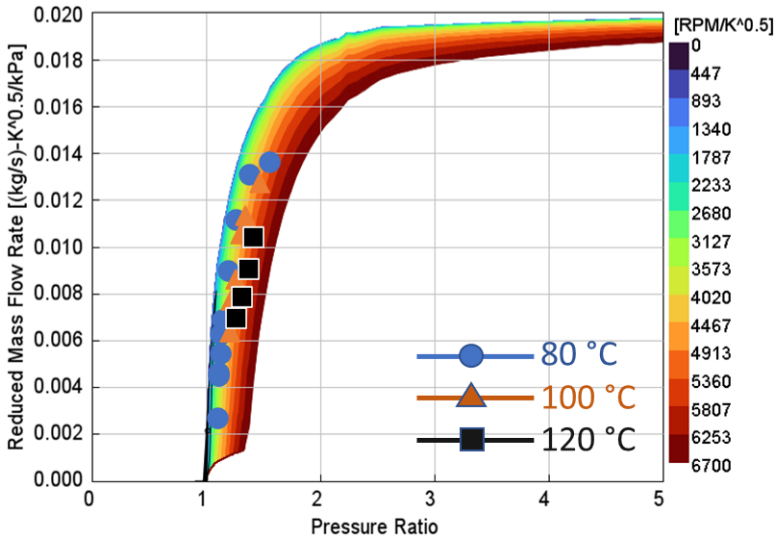


**Figure 4.12:** Operating points on the optimized turbine speed map

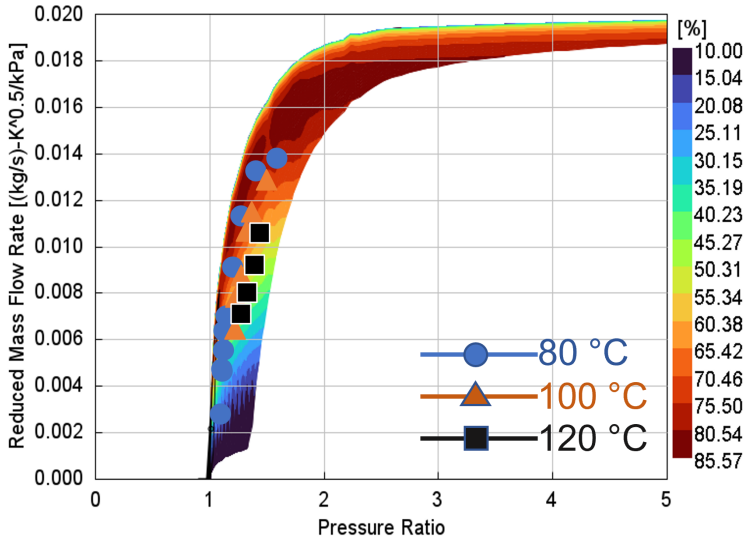


**Figure 4.13:** Operating points on the optimized turbine efficiency map

### 4.3.2 Cooling system design, and optimization

The cooling system is optimized similarly to the e-turbo, following the process described in section 3.1.2.4. A pre-defined industrial coolant pump, and radiator design exist in GT-Suite for a 60 kW operating FC. However, to achieve efficient operation, the coolant pump, and radiator fan design is optimized.

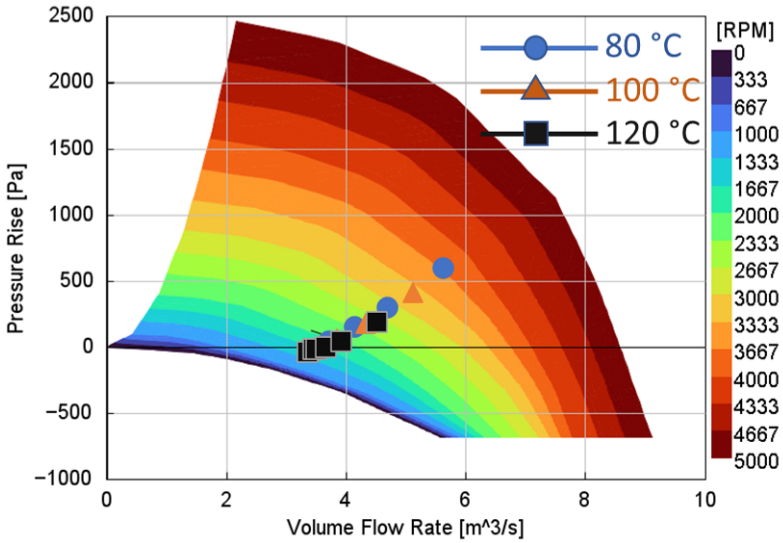


**Figure 4.14:** Operating points on the optimized radiator fan speed map

The initial design of the cooling system proved ineffective in maintaining the required temperatures of the FC at higher current densities. Consequently, the sizing of the pump, fan, and radiator is optimized to address this issue. Figures 4.14, and 4.15 demonstrate the operating point on the radiator fan, indicating that it operates at its highest power at an operating temperature of 80 °C followed by 100, and

120 ℃ respectively. This can be attributed due to the higher temperature gradient between the FC, and its surrounding environment for 80 ℃, followed by 100, and 120 ℃ respectively. By optimizing the size, and speed of the fan at each current density for all operating temperatures, it is possible to ensure efficient temperature management.

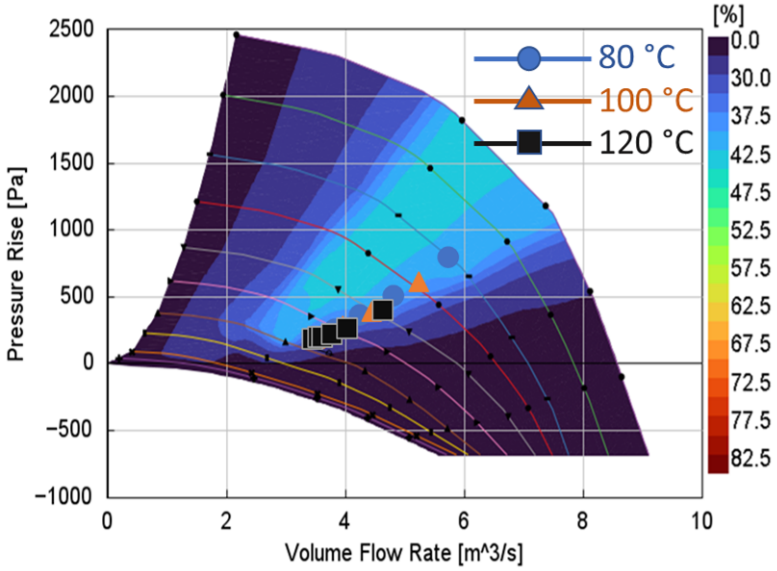


**Figure 4.15:** Operating points on the optimized radiator fan efficiency map

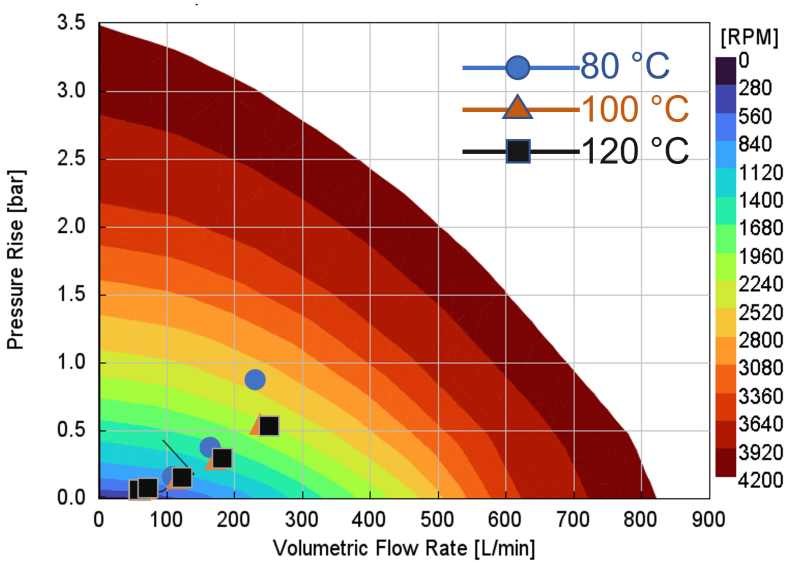


**Figure 4.16:** Operating points on the optimized coolant pump speed map

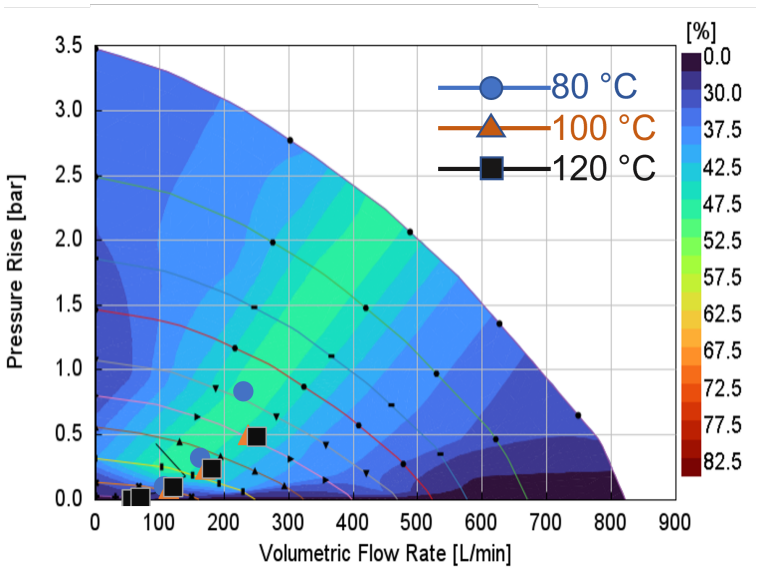


**Figure 4.17:** Operating points on the optimized coolant pump efficiency map

## 4.4 FC system performance

### 4.4.1 System performance at 80, 100, and 120 °C

Stack power, system power, power consumed by the parasitic components, and system efficiency are analysed, and explained below:

- **Polarization curve:**
  The complete system simulation is conducted after the successful design, and optimization of each component in the BoP.

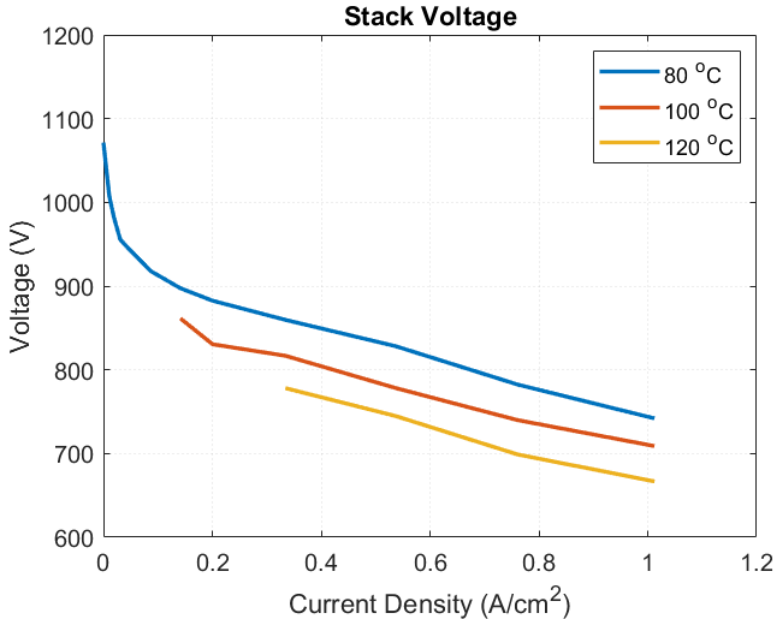


**Figure 4.18:** Polarization curve for FC system operating at 80, 100, and 120 °C

The simulation is conducted with constant FC system components at three different operating temperatures: 80, 100, and 120 ℃. Figure 4.18 illustrates that as the FC operating temperature increases, the polarization curve decreases. This decrease in performance at higher temperatures follows a similar trend as observed in the single-cell. However, it should be noted that the reduction in polarization cannot be solely attributed to the similarity of the trends. The inlet conditions at the system level differ across the three operating temperatures due to varying pressure requirements. As mentioned earlier, the inlet pressure is proportionately higher at higher temperatures, which would intuitively lead to better performance. Surprisingly, the performance actually decreases. One potential explanation for this lower performance at higher temperatures could be the lower RH of the membrane, and the higher ohmic losses associated with elevated temperatures. Furthermore, it is important to highlight that the FC does not operate effectively at lower current densities, specifically in the range of 0 to 0.2 A/cm$^2$ at 100 ℃, and 0 to 0.3 A/cm$^2$ at 120 ℃. This limitation arises from the inability of the compressor to sufficiently increase the pressure at lower mass flow rates, thereby hindering the FC's effective operation at those points.

- **Stack Power:**
  The stack power is determined by multiplying the current by the stack voltage. In this study, it is observed from figure 4.19 that the stack power is higher when the FC is operated at 80 ℃ across the entire range of current densities. However, the stack power decreases when the FC is operated at 100 ℃, and further decreases at 120 ℃. This decrease in stack power is proportional to the stack voltage.

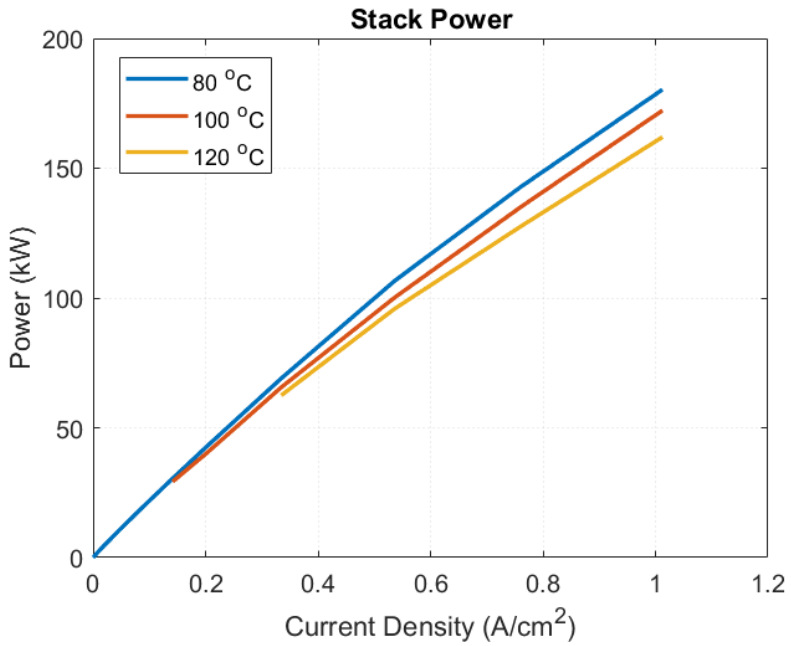


**Figure 4.19:** Electric power output for FC operating at 80, 100, and 120 ℃

Specifically, when comparing the stack power at 1 A/cm$^2$, it is found to be 181 kW when operating the FC at 80 ℃, 171 kW at 100 ℃, and 160 kW at 120 ℃, respectively. This indicates that the maximum power produced by the stack is 6% lower when operating the FC at 100 ℃, and 11% lower when operating at 120 ℃, compared to the 80 ℃ operating temperature.

- **System power, and losses:**
  The result of system power aligns with the earlier findings, as the stack power decreases with increasing temperature. System power accounts for all parasitic losses from the compressor, pump, fan, and DC/DC elements. Although the DC/DC system is not modeled in this thesis, its efficiency is assumed to be 98%. Figure 4.20 illustrates the system power for the three operating temperatures, while figure 4.21 shows the power consumption of the moving components. Upon analyzing the power consumption plots, it is evident that the compressor is the primary consumer of power in all cases. However, the consumption by the compressor is significantly higher at 100, and 120 ℃, indicating a proportionate power loss at the system level. Additionally, the turbine reflects some power back, but it is insufficient to compensate for the power consumed by the compressor. The fan also consumes a considerable amount of power, particularly at higher current densities. Interestingly, the power consumption of the fan, and pump is higher at 80 ℃ compared to 100, and 120 ℃. This is due to the cooling system requiring more energy to cool down higher temperature gradients.

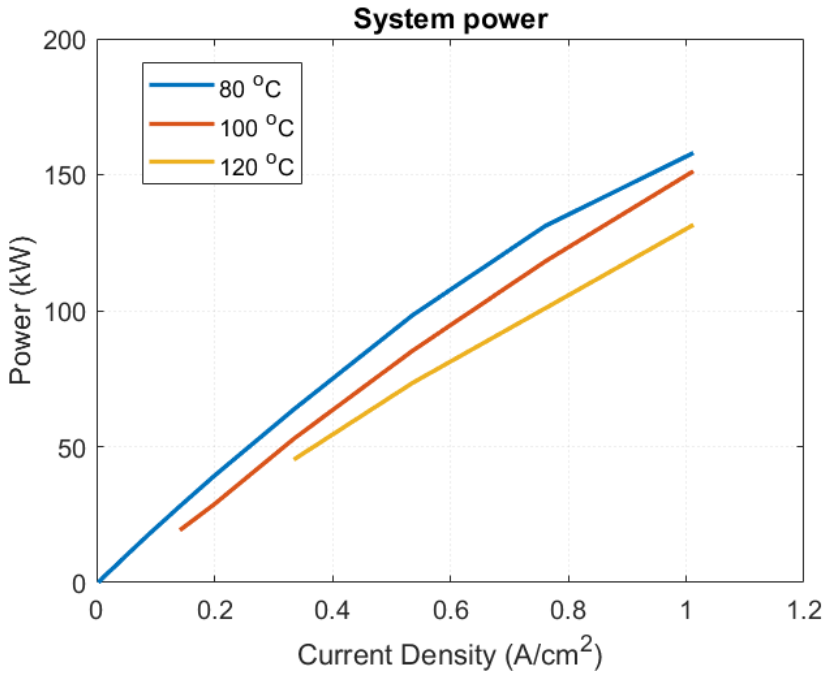


**Figure 4.20:** FC system power for the operation at 80, 100, and 120 ℃

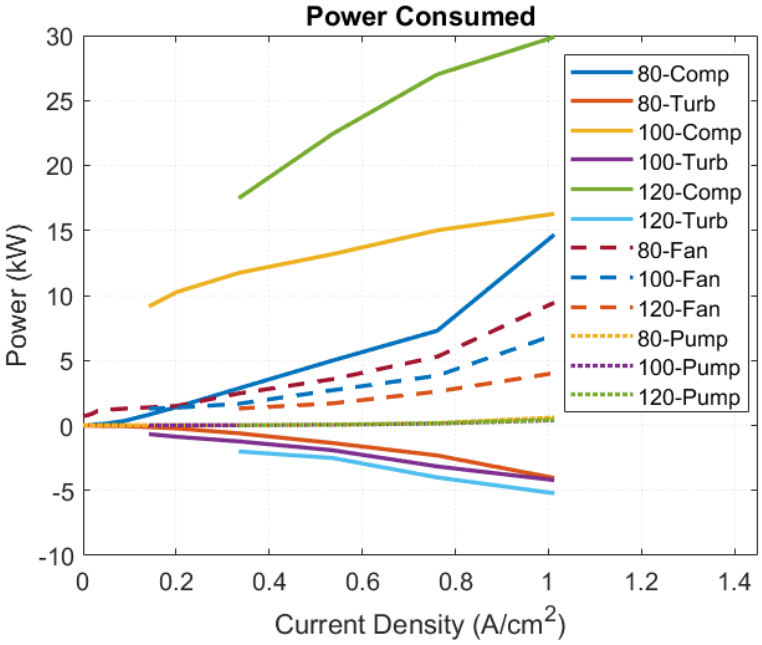


**Figure 4.21:** Power consumption by BoP at 80, 100, and 120 ℃

Figure 4.22 provides a breakdown of power losses at 1 A/cm$^2$. The compressor stands out as the highest power-consuming component, accounting for 48%, 58%, and 81% of power consumption at 80, 100, and 120 ℃, respectively.

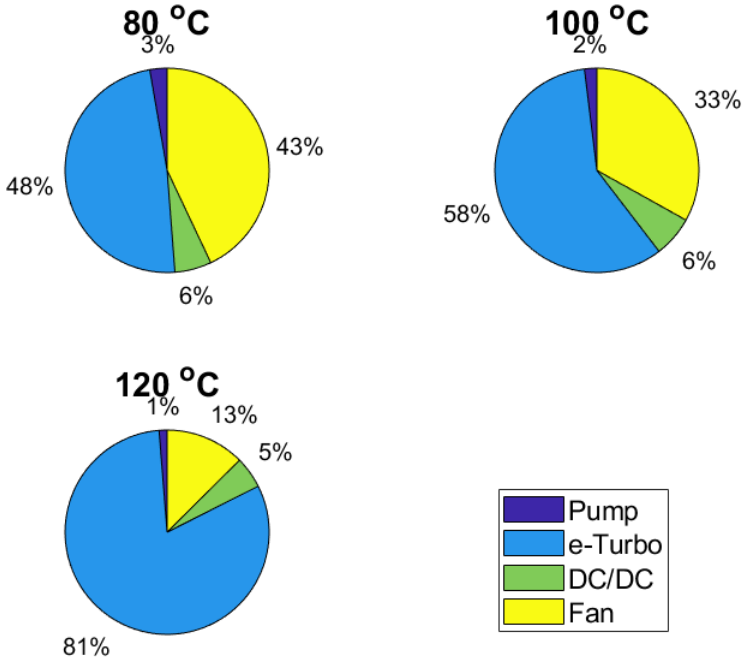


**Figure 4.22:** Losses distribution at 100% load at 80, 100, and 120 ℃

The fan, on the other hand, consumes 43%, 33%, and 13% of power at 80, 100,

and 120 ℃, respectively. Coolant pump, and DC/DC conversion on average consume 3%, and 6% respectively at all operating condition. Considering all losses, and parasitic components, reveals the system operating at 80 ℃, is capable of generating a maximum power output of 158 kW. This represents the highest power output among the three temperatures studied. For the FC system operating at 100 ℃, the maximum power output decreases to 151 kW. Furthermore, at the highest operating temperature of 120 ℃, the FC system's maximum power output is significantly reduced to 128 kW.

- **System Efficiency:**
  The efficiency of the FC system, taking into account all power consumed within the system, is shown in figure 4.23, and is analyzed at three operating temperatures. At an operating temperature of 80 ℃, the FC system exhibits an efficiency range of 51% – 41%. When the FC system operates at 100 ℃, the efficiency range is slightly lower, ranging from 41% – 39%. Finally, when the FC system is operated at 120 ℃, the efficiency range decreases, ranging from 34% – 33%.

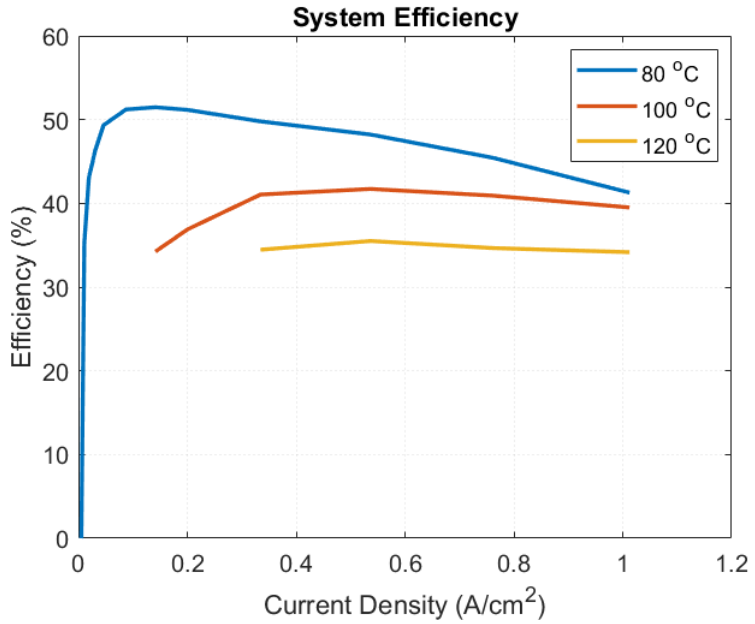


**Figure 4.23:** System efficiency for operation at 80, 100, and 120 ℃

- **Remarks:**
  The findings presented above underscore the significance of temperature control in optimizing the performance, and efficiency of FC systems. It is evident that operating the FC at lower temperatures results in higher power output, and improved efficiency, while operating at 120 ℃ demonstrates lower power output, and efficiency. However, it is important to note that maintaining a temperature of 80 ℃ necessitates a larger cooling system. Based on the analysis conducted, a careful consideration is recommended for integrating a mix state system that operates the FC at 80 ℃ up to a current density of 0.8 A/cm$^2$, and at 100 ℃ for higher current densities. This approach allows for leveraging the performance benefits of operating at 80 ℃ while optimizing the

cooling system.
By adopting this approach, the system can benefit from the higher power output, and efficiency achieved at 80 ℃, while still accommodating higher current densities by transitioning to 100 ℃. This strategy allows for a balance between performance, and cooling system optimization, A similar system was designed, and the results are presented in the below section.

### 4.4.2 System performance at 80 ℃, 100 ℃, and mix state

In order to enhance the overall system design, additional optimization was performed for the mixed system. This optimization effort led to a reduction in the compressor map by 30%, resulting in a decrease in the maximum pressure ratio from 8.5 bar to 6 bar. Moreover, a notable achievement was the reduction in the radiator heat transfer area by 55%. To assess the performance of the optimized system, a performance comparison was conducted. The results of this comparison are presented below:

- **Polarization Curve:**
  Upon downsizing the compressor map in the mixed system, it was observed that the original operation at 80 ℃ was no longer feasible, particularly at current densities below 0.4 A/cm$^2$. As a result, the operating points for the mixed system were optimized to ensure operation within the surge zone of the compressor, preventing any detrimental effects on system performance. The polarization curve below illustrates the comparison between the potential output of the mixed system, and the actual operation at 80 ℃:

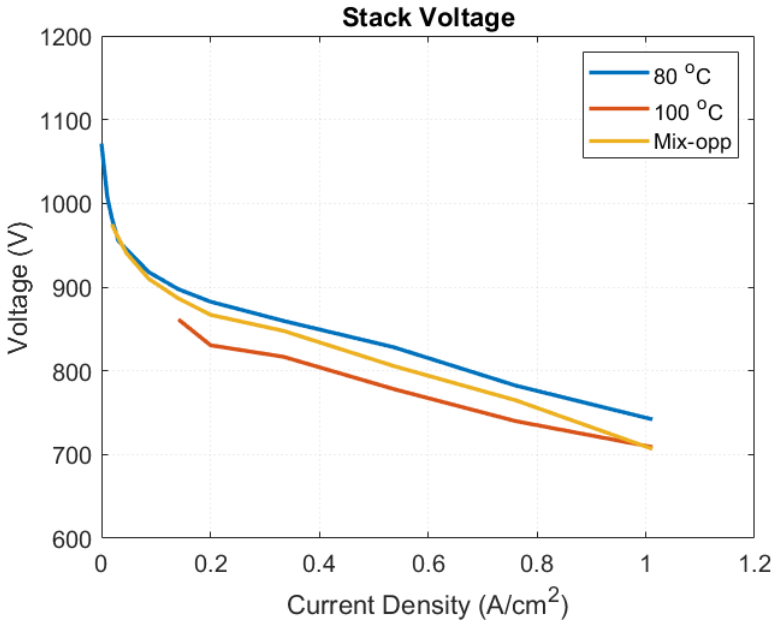


**Figure 4.24:** Polarization curve for FC operating at 80 ℃, 100 ℃, and mix state

From the polarization curve in figure 4.24, it is evident that the potential output of the mix system is lower than the actual operation at 80 ℃. This disparity in performance can be attributed to the further optimization of the

system for a smaller compressor, resulting in lower pressure, and reduced overall performance.

- **Stack Power:**
  As seen in figure 4.25 that the stack power is proportion to the potential output, the FC stack power experiences a reduction when operating the FC at 80 ℃, specifically below a current density of 0.8 A/cm$^2$. However, it is noteworthy that the stack power remains comparable at the maximum current density when operating at 100 ℃. This reduction in stack power at lower current density, operating at 80 ℃ is in proportion to the potential output, and can be attributed to the specific operating conditions, and system optimization.

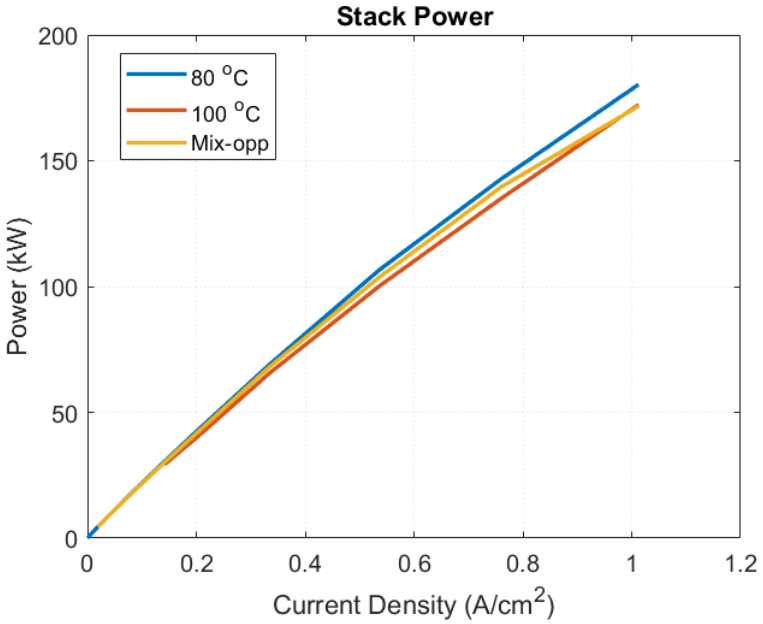


**Figure 4.25:** Electrical power for FC operating at 80 ℃, 100 ℃ mix state

- **System power, and loses:**
  When comparing from stack to system, the maximum useful power is reduced by 13%, 12%, and 12% for system operating at 80 ℃, 100 ℃, and mixed operating temperatures, respectively. From figure 4.26, it is observed that the system power remains the same up to 0.5 A/cm$^2$. However, it diverges for higher loads when operating at 80 ℃, and mixed operating conditions.At lower loads up to 0.2 A/cm$^2$, the fan power consumption is the highest. For the mixed system, the fan consumption is lower by almost 2 kW up to 0.8 A/cm$^2$. Once the shift activates to ramp up the temperature to 100 ℃ at higher loads, the fan consumption increases. At higher loads above 0.2 A/cm$^2$, as seen in figure 4.27 the compressor consumption increases. The power consumed by the compressor is lower when operating the mixed system at 80 ℃ compared to the original system running. However, the compressor consumption is higher at the highest load. One of the reason is that the mixed system utilizes a smaller compressor with lower operating points in the mixed system operating at 80 ℃.

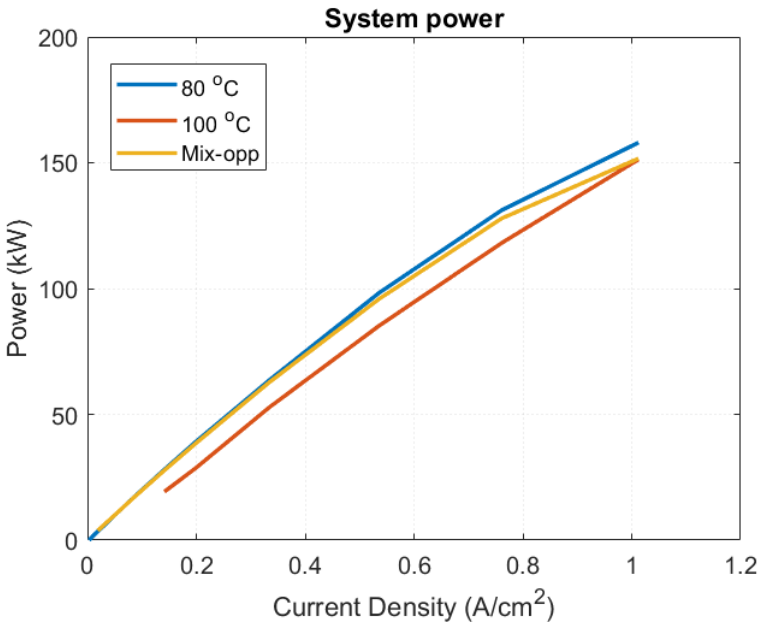


**Figure 4.26:** FC system power operating at 80 ℃, 100 ℃, and mix-state

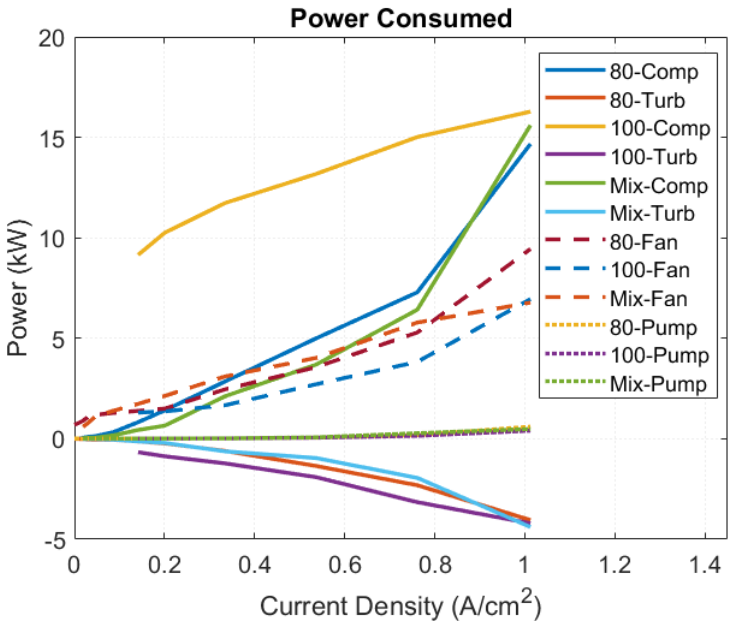


**Figure 4.27:** Power consumption by BoP while operating at 80 ℃, 100 ℃, and mix state

It can be seen in figure 4.28 at peak load, the mixed system consumes 7% higher power on the compressor. On the other hand, the power consumption is reduced by 9% for the fan. Due to the utilization of a smaller-sized compressor, and radiator in the mixed system.

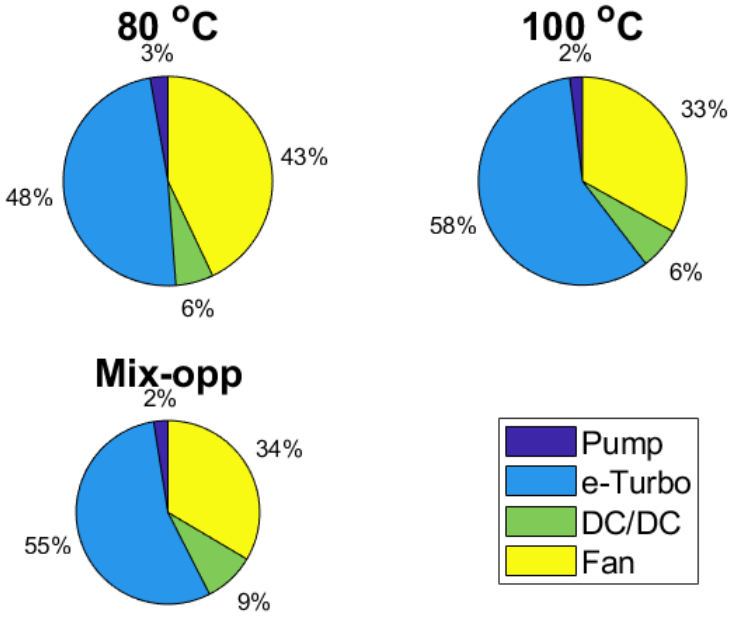


**Figure 4.28:** Losses accumulation at 100% load for 80 ℃, 100 ℃, and mix state

- **System Efficiency:**
  FC efficiency with mixed system is shown in figure 4.29. As anticipated, the system level efficiency for the FC operating at 80 ℃ is the highest.

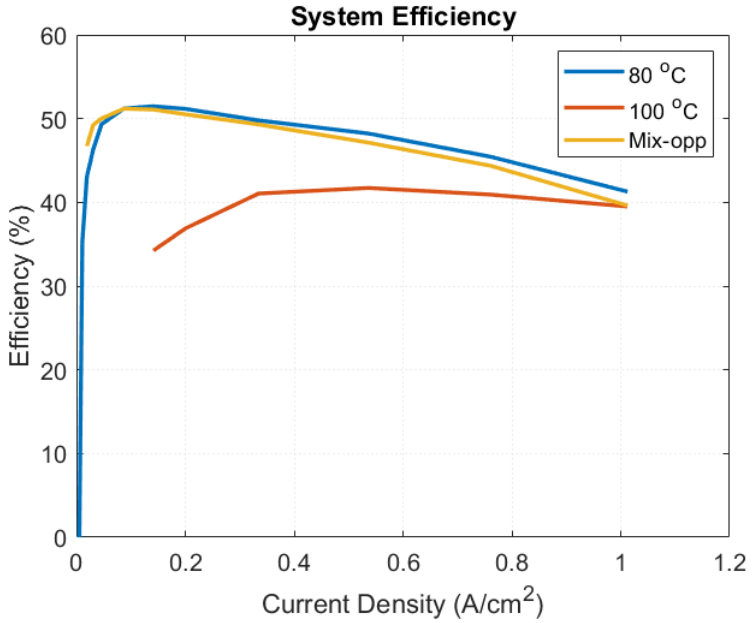


**Figure 4.29:** System efficency for 80 ℃, 100 ℃, and mix state

The efficiency range for the 80 ℃ operating temperature is observed to be from 51% – 41%. For the mixed system, the efficiency slightly decreases at higher

loads. The efficiency range for the mixed system is found to be from 51% – 40%. While the downsized compressor enables improved system optimization, it also introduces limitations in terms of power output. Overall, the mixed system exhibits a bit lower efficiency profile compared to the original 80 ℃ operation due to the system's further optimization for a smaller compressor, and radiator leading to reduced pressure, and increased fan load.

## 4.5 Vehicle level performance

After integrating the FC system with the representative vehicle powertrain, a longer constant-speed driving cycle with lower stops was implemented. This driving cycle was chosen to align with the focus of the thesis, which is the development of FC systems for heavy-duty mobility, as these transportation vehicles typically follow such patterns. Figure 4.30, and 4.31 shows the FC, and battery performance at vehicle level. The FC operating at 80 ℃ can ramp up to a maximum power of 300 kW, whereas the FC operating at 100 ℃, and mixed operation can maximum power provided 260 kW.

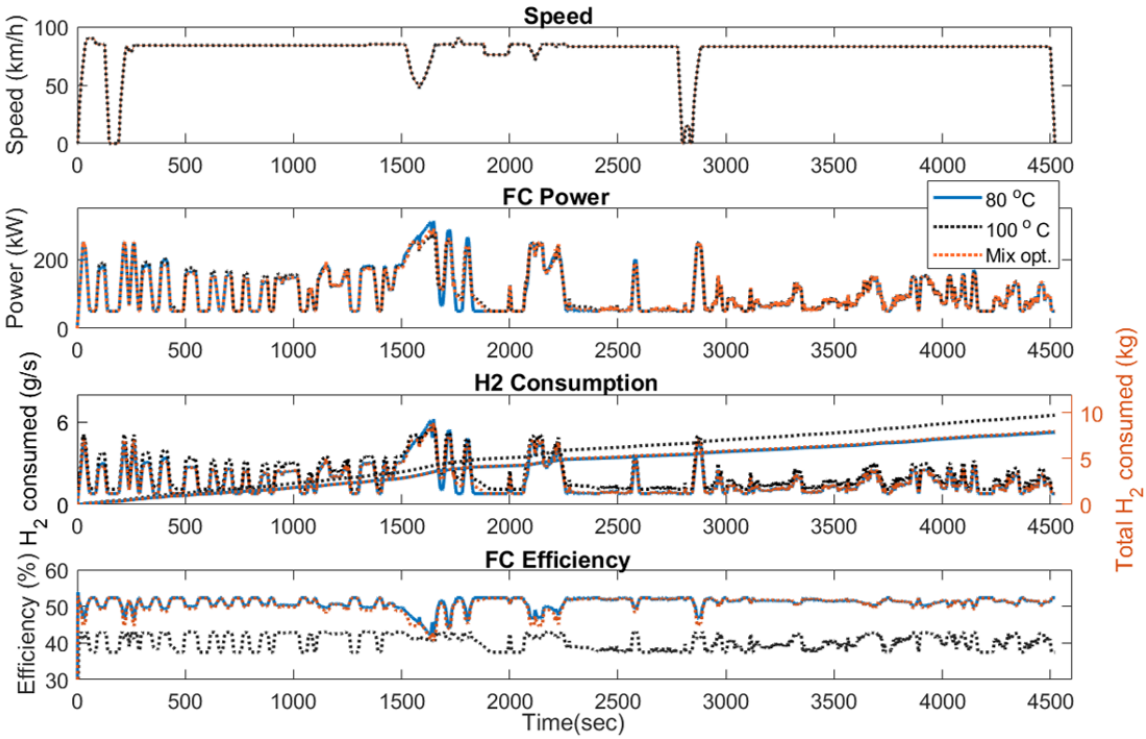


**Figure 4.30:** FC performance at vehicle level

Hydrogen consumption of 7.5 kg/100km, 7.7 kg/100km, and 9.4 kg/100km is observed while operating the FC at 80 ℃, mixed, and 100 ℃ respectively. This shows that the hydrogen consumption is 23% higher when operating at 100 ℃, and 2.6% higher with mixed operation compared to operating at 80 ℃. Operating the FC continuously at 100 ℃ will result in a loss of overall energy estimation. This indicates

a decrease in efficiency compared to operating at 80 ℃. The mixed state operation of the FC system presents an intriguing finding. A significant higher consumption of 2.6% is primarily observed during higher load conditions. This demonstrates that the mixed state operation offers potential for improved efficiency compared to operating solely at 100 ℃.

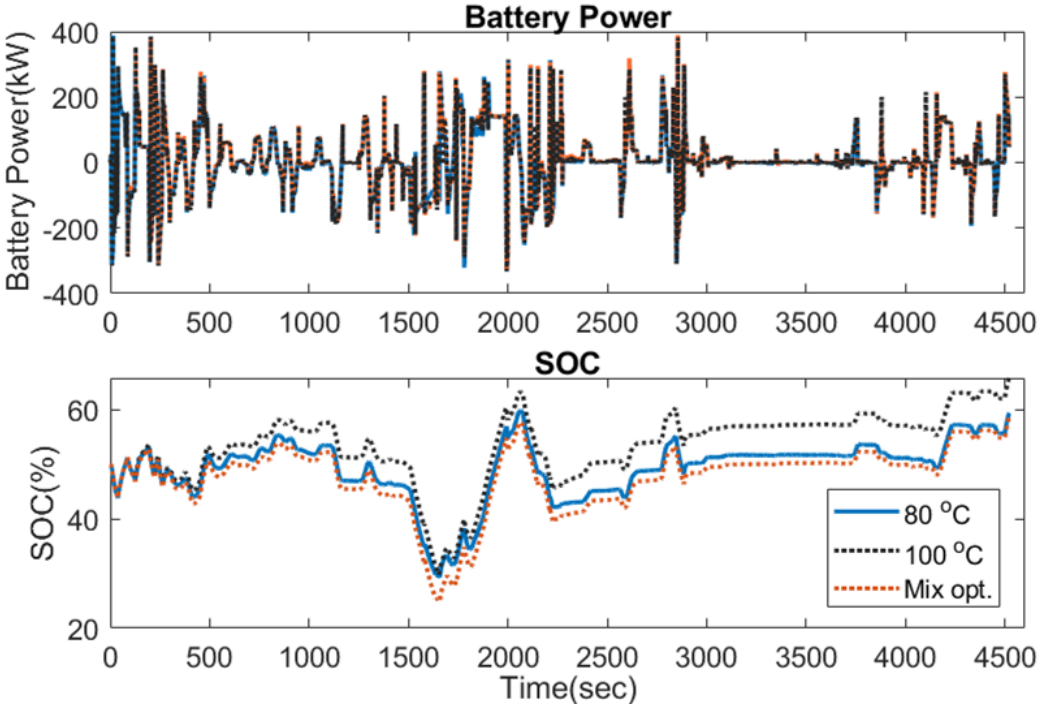


**Figure 4.31:** Buffer battery power consumption

# 5
# Conclusion

In conclusion, the results of this thesis highlight the importance of temperature control, and system optimization in FC systems. Operating the FC at lower temperatures, such as 80 ℃, provides higher power output, and improved efficiency. On the other hand, operating at higher temperatures, particularly 120 ℃, leads to decreased performance, and efficiency. This is due to accelerated degradation, and the requirement of the larger compressor which consumes 19% of the stack power.
The degradation models used in the study accurately reflected the experimental results, demonstrating voltage drops of 6% after 15,000 hrs while operating at 80 ℃, and approximately 4,930 hrs while operating at 100 ℃. The accelerated degradation at 120 ℃ resulted in a significant voltage drop in a much shorter operation time. The polarization curve analysis showed a decrease in performance as the FC operated at higher temperatures, indicating the impact of lower RH, and increased ohmic losses. Surprisingly, the higher inlet pressure at higher temperatures did not compensate for the performance decline.
The power consumption analysis revealed that the compressor was the major consumer of power in the system, followed by the fan. The power consumption of these components increased at higher temperatures, leading to proportionate power losses at the system level. The coolant pump, and DC/DC conversion also contributed to power consumption, but to a lesser extent. The efficiency analysis demonstrated that operating the FC at 80 ℃ yielded the highest efficiency, ranging from 51% – 41%. However, the efficiency slightly decreased at higher loads for the mixed system ranging from 51% – 40%. These findings emphasize that a mixed operation has a respective importance on system optimization, and FC efficiency. Further, the integration of the FC system with a representative vehicle powertrain highlighted the power capabilities at different temperatures. The FC operating at 80 ℃ had a maximum power output of 300 kW, while at 100 ℃, and in mixed operation, the maximum power output was limited to 260 kW.
Hydrogen consumption, after integrating the FC with the vehicle model shows that higher temperatures result in higher consumption. Operating at 100 ℃ leads to a 25% higher hydrogen consumption when compared with 80 ℃ operation, while mixed condition showed a 2.6% increase respectively. These findings highlight the significance of temperature control, system optimization, and meticulous selection of operating conditions to maximize the performance, and efficiency of FC systems in heavy-duty mobility applications.

# 6
# Future work

This thesis work sheds light on the feasibility of operating PEM FCEVs at extended intermediate temperatures, specifically up to 120 ℃. However, the challenges associated with operating the system at higher temperatures are evident, encompassing issues such as cell degradation, effective water management under elevated temperatures, and the need for component designs capable of meeting high-pressure requirements.
This presents some avenues for future work that can be explored on the findings of this study:

- **Nafion material**
  While PFSA Nafion is commonly used in industrial applications, its conductivity decreases at elevated temperatures. Therefore, future research should focus on developing, and evaluating new materials that exhibit higher conductivity at intermediate temperatures.
- **System design**
  One area of future focus should be the development of a compressor design that facilitates operation at lower mass flow rates, enabling efficient performance at various operating conditions. Additionally, exploring alternative materials for gas-to-gas humidifiers, which are currently based on Nafion membranes for water transportation, could enhance the performance, and reliability of the humidification process.
- **Dynamic modeling**
  The current simulation approach used in this study is limited to static modeling, which provides valuable insights into the system's performance, and degradation. However, investigating the dynamic behavior of the system, considering the effects of degradation over time, would provide a more comprehensive understanding of the system's response under varying operating conditions.
- **Effect of degradation on vehicle level**
  To fully assess the practical implications of FC degradation, it would be valuable to investigate the impact of degradation on the performance of the FC system at the vehicle level. Evaluating the degraded state performance of the FC system in a realistic vehicle environment would provide insights into the system's long-term reliability, durability, and overall efficiency.

# Bibliography


[1] Song. (2005). High-performance PEMFCs at elevated temperatures using Nafion 112 membranes. Journal of the Electrochemical Society., 152(3). https://doi.org/10.1149/1.1855871.

[2] Jianlu Zhang, Yanghua Tang, Chaojie Song, Zetao Xia, Hui Li, HaijiangWang, Jiujun Zhang. "PEM fuel cell relative humidity (RH) and its effect on performance at high temperatures". Electrochimica Acta 53 (2008) 5315–5321 https://doi.org/10.1016/j.electacta.2008.02.074.

[3] Hui Xu, Ying Song, H. Russell Kunz, and James M. Fenton. "Effect of Elevated Temperature and Reduced Relative Humidity on ORR Kinetics for PEM Fuel Cells". Journal of The Electrochemical Society, Volume 152, Number 9 https://iopscience.iop.org/article/10.1149/1.1984351.

[4] Barbir, F. (2013). *PEM Fuel Cells: Theory and Practice (2nd ed.)*. Elsevier. http://dx.doi.org/10.1016/B978-0-12-387710-9.00001-1.

[5] Larminie, J., & Dicks, A. (2003). *Fuel Cell Systems Explained (2nd ed.)*. John Wiley & Sons, Ltd. ISBN: 0-470-84857-X.

[6] Dario R. Dekel, Review of cell performance in anion exchange membrane fuel cells, Journal of Power Sources, Volume 375, 2018, Pages 158-169, ISSN 0378-7753, https://doi.org/10.1016/j.jpowsour.2017.07.117.

[7] O'Hayre, R., Cha, S.W., Colella, W.G., Prinz, F.B. (2016). *Fuel Cell Fundamentals (3rd ed.)*. John Wiley & Sons, Ltd. ISBN: 9781119114208.

[8] Chen E. Thermodynamics and Electrochemical Kinetics. In: Hoogers G, editor. Fuel Cell Technology Handbook. Boca Raton, FL: CRC Press; 2003.

[9] Mahmoud M. Saleh, Takeoshi Okajima, Masahiko Hayase, Fusao Kitamura, Takeo Ohsaka, Exploring the effects of symmetrical and asymmetrical relative humidity on the performance of H2/air PEM fuel cell at different temperatures, Journal of Power Sources, Volume 164, Issue 2, 2007, Pages 503-509, ISSN 0378-7753,https://doi.org/10.1016/j.jpowsour.2006.11.065.

[10] Zhang, R. Lin, L. Técher, X. Cui Experimental study of variable operating parameters effects on overall pemfc performance and spatial performance distribution Energy, 115 (2016), pp. 550-560 https://10.1016/j.energy.2016.08.086.

[11] Alfieri, V., Binetti, G., Ruotolo, R., and Gandino, E., "Optimal Control of a Fuel Cell Electric Vehicle (FCEV) Powertrain," SAE Technical Paper 2022-01-1131, 2022, https://doi.org/10.4271/2022-01-1131.

[12] Denver F. Cheddie, Norman D.H. Munroe., "Analytical correlations for intermediate temperature PEM fuel cells", Journal of Power Sources 160 (2006) 299 304 https://doi.org/10.1016/j.jpowsour.2006.01.046.

[13] Mohammad Bagher Karimi, Fereidoon Mohammadi, Khadijeh Hooshyari, Recent approaches to improve Nafion performance for fuel cell applications: A review, International Journal of Hydrogen Energy, Volume 44, Issue 54, 2019,Pages 28919-28938, https://doi.org/10.1016/j.ijhydene.2019.09.096..

[14] Morihiro Saito, Naoko Arimura, Kikuko Hayamizu, and Tatsuhiro Okada, Mechanisms of Ion and Water Transport in Perfluorosulfonated Ionomer Membranes for Fuel Cells, The Journal of Physical Chemistry B 2004 108 (41), 16064-16070, DOI: 10.1021/jp0482565.

[15] Liu W, Peng Z, Kim B, Gao B, Pei Y. "Development of a PEMFC dynamic model and the application to the analysis of fuel cell vehicle performance". 4th International Conference on Energy Materials and Applications; 2019. https://doi.org/10.1088/1757-899X/628/1/012006.

[16] S.F. Bordín, H. Andrada, A. Carreras, G. Castellano, R. Oliveira, V.G. Jos Nafion membrane channel structure studied by small-angle X-ray scattering and Monte Carlo simulations Polymer, 155 (2018), pp. 58-63.

[17] Seung-Eun Nam, Sang-Ock Kim, Yongku Kang, Jae Wook Lee, Kew-Ho Lee, Preparation of Nafion/sulfonated poly(phenylsilsesquioxane) nanocomposite as high temperature proton exchange membranes, Journal of Membrane Science, Volume 322, Issue 2, 2008, Pages 466-474, ISSN 0376-7388, https://doi.org/10.1016/j.memsci.2008.05.075.

[18] Xu, Guoxiao and Dong, Xinwei and Xue, Bin and Huang, Jianyou and Wu, Junli and Cai, Weiwei, Recent Approaches to Achieve High Temperature Operation of Nafion Membranes, https://www.mdpi.com/1996-1073/16/4/1565.

[19] Dicks, Andrew L. Rand, David A. J.. (2018). Fuel Cell Systems Explained (3rd Edition). John Wiley Sons. https://app.knovel.com/hotlink/toc/id:kpFCSEE01P/fuel-cell-systems-explained/

fuel-cell-systems-explained.

[20] Jayakumar, A., Sethu, S.P., Ramos, M. et al. A technical review on gas diffusion, mechanism and medium of PEM fuel cell. Ionics 21, 1–18 (2015). https://doi.org/10.1007/s11581-014-1322-x.

[21] Reza Omrani, Chapter 5 - Gas diffusion layer for proton exchange membrane fuel cells, Editor(s): Gurbinder Kaur, PEM Fuel Cells, Elsevier, 2022, Pages 91-122, ISBN 9780128237083, https://doi.org/10.1016/B978-0-12-823708-3.00017-1.

[22] Y. Wang, C.-Y. Wang, K.S. Chen Elucidating differences between carbon paper and carbon cloth in polymer electrolyte fuel cells Electrochim. Acta, 52 (12) (2007), pp. 3965-3975, https://doi.org/10.1016/j.electacta.2006.11.012.

[23] Xianguo Li, Imran Sabir, Review of bipolar plates in PEM fuel cells: Flow-field designs, International Journal of Hydrogen Energy, Volume 30, Issue 4, 2005, Pages 359-371, ISSN 0360-3199, https://doi.org/10.1016/j.ijhydene.2004.09.019.

[24] Reiser CA, Sawyer RD. Solid polymer electrolyte fuel cell stack water management system. US Patent No. 4,769,297, 1988.

[25] Pollegri A, Spaziante PM. US Patent No. 4,197,178, 1980.

[26] Watkins DS, Dircks KW, Epp DG. US Patent No. 4,988,583, 1991.

[27] Marvin Russel H, Carlstrom CM. US Patent No. 6,500,580, 2002.

[28] Compressor definition from wikipedia https://en.wikipedia.org/wiki/Compressor.

[29] Yu, W., Sichuan, X., and Ni, H., "Air Compressors for Fuel Cell Vehicles: An Systematic Review," SAE Int. J. Alt. Power. 4(1):115-122, 2015, https://doi.org/10.4271/2015-01-1172.

[30] Zhang, Y.; Wang, J.; Yao, Z. Recent Development of Fuel Cell Core Components and Key Materials: A Review. Energies 2023, 16, 2099, https://doi.org/10.3390/en16052099.

[31] Air filters for Fuel cell https://www.hengst.com/en/products/fuel-cell/cathode-air-filter/.

[32] Rivard E, Trudeau M, Zaghib K. Hydrogen Storage for Mobility: A Review. Materials (Basel). 2019 Jun 19;12(12):1973. doi: 10.3390/ma12121973. PMID:

31248099; PMCID: PMC6630991.

[33] Sung Chan Kim, Seung Hoon Lee, Kee Bong Yoon, Thermal characteristics during hydrogen fueling process of type IV cylinder, International Journal of Hydrogen Energy, Volume 35, Issue 13, 2010, Pages 6830-6835, ISSN 0360-3199, https://doi.org/10.1016/j.ijhydene.2010.03.130.

[34] Abdalla M. Abdalla, Shahzad Hossain, Ozzan B. Nisfindy, Atia T. Azad, Mohamed Dawood, Abul K. Azad, Hydrogen production, storage, transportation and key challenges with applications: A review, Energy Conversion and Management, Volume 165, 2018, Pages 602-627, ISSN 0196-8904,https://doi.org/10.1016/j.enconman.2018.03.088.

[35] Petitpas, G., Simon, A.J., Moreno-Blanco, J. and Aceves, S.M., 2017. Liquid hydrogen infrastructure analysis. Lawrence Livermore National Laboratory: Livermore, CA, USA.

[36] Abdalla M. Abdalla, Shahzad Hossain, Ozzan B. Nisfindy, Atia T. Azad, Mohamed Dawood, Abul K. Azad, Hydrogen production, storage, transportation and key challenges with applications: A review, Energy Conversion and Management, Volume 165, 2018, Pages 602-627, ISSN 0196-8904, https://doi.org/10.1016/j.enconman.2018.03.088.

[37] SAE International SAE J2600 Compressed Hydrogen Surface Vehicle Fueling Connection Devices ;2015 https://www.sae.org/standards/content/j2600_201211.

[38] Trung V. Nguyen and Ralph E. White 1993 J. Electrochem. Soc. 140 2178DOI 10.1149/1.2220792.

[39] B.K. Hong, S.H. Kim Recent advances in fuel cell electric vehicle technologies of hyundai ECS Trans, 86 (2018), pp. 3-11.

[40] Fuel cell electric vehicles in China https://fuelcellsworks.com/news/china-saic-motors-achieves-milestones-with-it-fuel-cell-vehicles/.

[41] Radiator schematic diagram https://michaelandcompany.com/radiator-and-engine-cooling-system-service/.

[42] T. E. Springer, T. A. Zawodzinski, and S. Gottesfeld, Polymer Electrolyte Fuel Cell Model, Los Alamos National Laboratory, Los Alamos, New Mexico 87545.

[43] Daniel G. Sanchez, Tiziana Ruiu, Indro Biswas, Mathias Schulze, Stefan Helmly, K. Andreas Friedrich, Local impact of humidification on degradation in polymer electrolyte fuel cells, Journal of Power Sources, Volume 352, 2017, Pages 42-55, ISSN 0378-7753,

https://doi.org/10.1016/j.jpowsour.2017.03.057.

[44] Deuk Ju Kim, Min Jae Jo, Sang Yong Nam, A review of polymer–nanocomposite electrolyte membranes for fuel cell application, Journal of Industrial and Engineering Chemistry, Volume 21,2015, Pages 36-52, ISSN 1226-086X, https://doi.org/10.1016/j.jiec.2014.04.030.

[45] Martina B, Björn E, Nikola N, Carina L, Göran L, Rakel W.L, "The effect of oxygen partial pressure and humidification in proton exchange membrane fuel cells at intermediate temperature (80–120$^o$ C)", Journal of Power Sources, Volume 563, 2023.https://doi.org/10.1016/j.jpowsour.2023.232803.

[46] Jintae K, Minjin K, Taegon K, Young-Jun S, Taewon S, Kyoung H.C, "Degradation modeling and operational optimization for improving the lifetime of high-temperature PEM (proton exchange membrane) fuel cells", Energy, Volume 66, 2014 https://doi.org/10.1016/j.energy.2013.08.053.

[47] Master Thesis : Turbo for Fuel Cell Electric Vehicle https://lup.lub.lu.se/luur/download?func=downloadFile&recordOId=9084918&fileOId=9084927.

[48] GT-Suite software https://www.gtisoft.com/gt-suite/.

[49] Gustaver, M. (2020) A Chalmers University of Technology Master's thesis template for LaTeX. Unpublished.

# A

# Appendix 1

## A.1 GT Suite

All the information is taken form the Gamma technologies own website [48]
GT-Suite is a versatile simulation tool that caters to a wide range of applications and industries. This software provides comprehensive capabilities for designing various aspects, ranging from initial conceptual designs to intricate subsystem and component analyses. At the core of the program lies its multi-physics platform, which encompasses specialized libraries such as the flow library, thermal library, and electrochemical library. By leveraging this multi-physics platform, users can effortlessly configure their desired simulation scenarios within a unified modeling environment. According to the official Gamma Technologies website, GT-Suite offers numerous possibilities. For instance, it enables users to employ a lumped battery model for analyzing drive cycles or utilize a cell-level model with 3D finite element thermal discretization to pinpoint local hotspots during acceleration events. This showcases the software's flexibility and adaptability to accommodate diverse simulation needs and deliver precise insights for various scenarios.

## Final Model in GT-SUITE

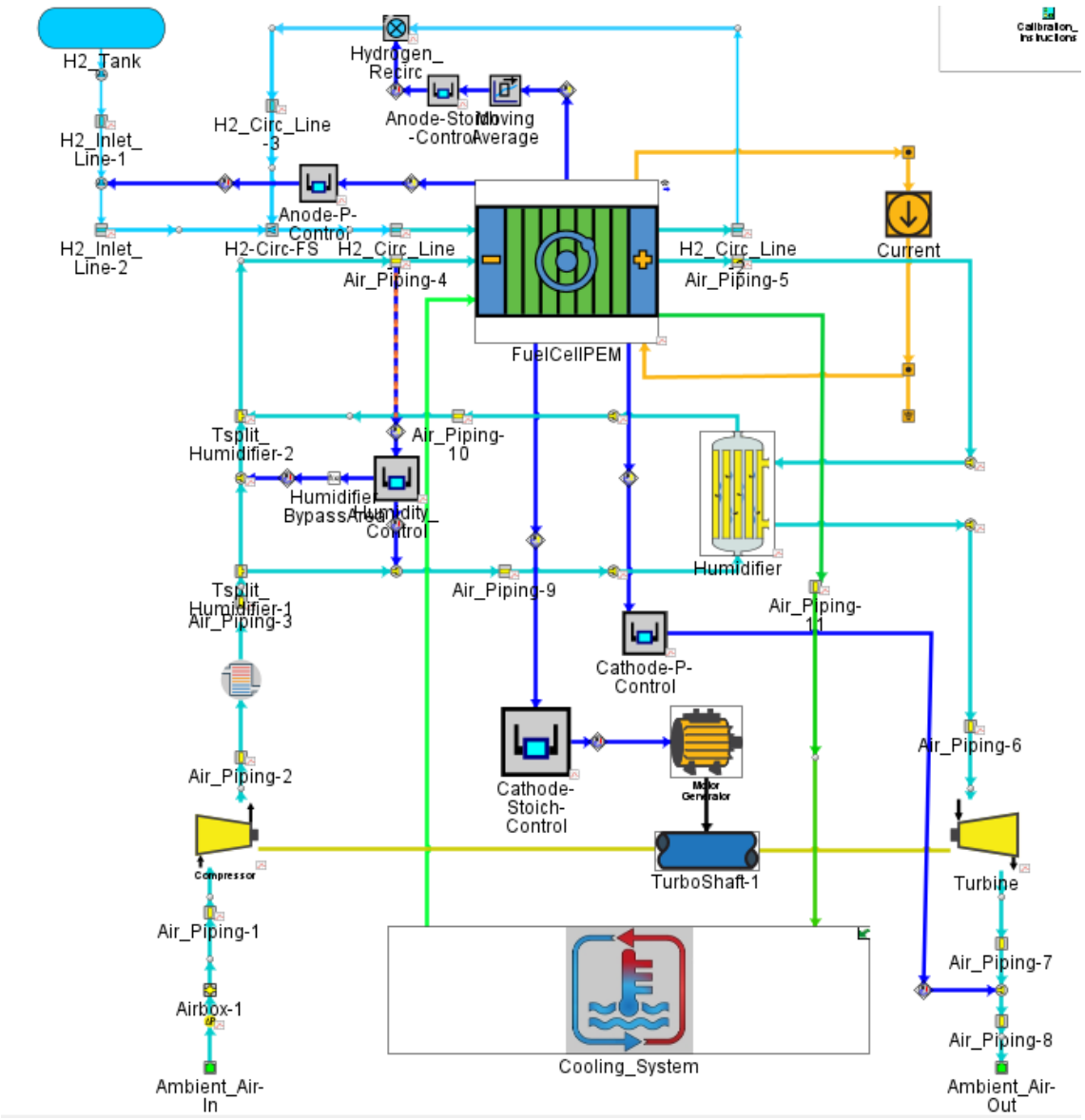


**Figure A.1:** Schematic of airflow

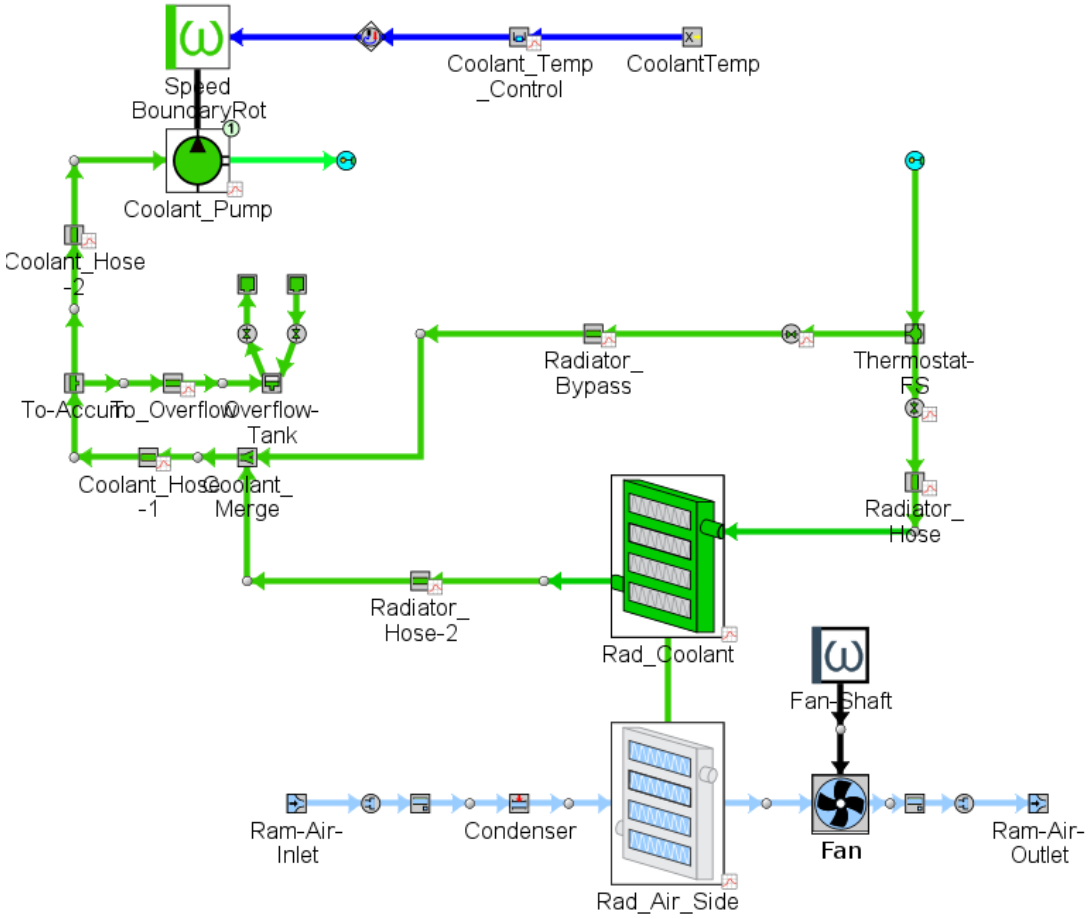


**Figure A.2:** Schematic of airflow

**DEPARTMENT OF SOME SUBJECT OR TECHNOLOGY**
**CHALMERS UNIVERSITY OF TECHNOLOGY**
Gothenburg, Sweden
www.chalmers.se


CHALMERS
UNIVERSITY OF TECHNOLOGY